

**MECHANICALLY CHARACTERIZING POLYMERIC MATERIALS
USING BUCKLING MECHANICS AND MECHANOPHORES**

by

Mitchell L. Rencheck

A Dissertation

Submitted to the Faculty of Purdue University

In Partial Fulfillment of the Requirements for the degree of

Doctor of Philosophy



School of Materials Engineering

West Lafayette, Indiana

December 2020

THE PURDUE UNIVERSITY GRADUATE SCHOOL
STATEMENT OF COMMITTEE APPROVAL

Dr. Chelsea S. Davis, Chair

School of Materials Engineering

Dr. Kendra A. Erk

School of Materials Engineering

Dr. Jeffery P. Youngblood

School of Materials Engineering

Dr. Jan Anders-Mansson

School of Materials Engineering

Approved by:

Dr. David F. Bahr

To Steffi, Mom, Dad, Michael, Walter, Dorothy, Richard, and Eleanor

ACKNOWLEDGMENTS

If I were to go back and tell a 16 year old version of myself that in 10 years I would write a dissertation and complete a Ph.D., I would have probably laughed myself right out of the room. The truth is that, while yes I did write a dissertation and complete a Ph.D., none of what I have accomplished over the past 4+ years would be possible without my family, friends, lab mates, sponsors, and advisors. With that being said, this collection of work has been fully made possible by you all, and for that, I cannot thank you enough.

I would like to start my parade of acknowledgments by honoring my sweet wife, Steffi. I could write pages and pages of thanks and gratitude to her, but I would also like to turn in this dissertation by the deadline. It is difficult to find enough words for expressing my love and appreciation for how she has dealt with me throughout my time in graduate school. While we have not been married the whole duration of my Ph.D., she has witnessed both the miseries and triumphs. She has picked me up and encouraged me through the low points and celebrated with me in the high points. The sacrifices she has made while pursuing my Ph.D. have been many, and I will never be able to do enough to express my gratitude to her. She has been a solid foundation for me throughout this journey, and for that, I cannot acknowledge and thank her enough. I love you Steffster!

I would have not arrived at the end of my Ph.D. journey without the support of my advisor, Prof. Chelsea Davis. As Prof. Davis's first graduate student to graduate with their Ph.D., the journey has consisted of setting up a laboratory, making up group activities, and getting the chance to name equipment, which actually never happened. From the beginning, I definitely felt that Prof. Davis cared about my development as a researcher, professional, and human being. A few golden nuggets I have taken away from the Davis Research Group (DRG) are the importance of understanding the underlying science behind a result, the significance of effectively communicating results to an audience, and how to explain fundamental science to others. Looking back to August of 2016 and seeing how much growth I have made is astonishing and I have Prof. Davis to greatly thank for that. Lastly, I want to acknowledge how grateful I am for the great work-life balance created in the DRG. Being seen as a person and not a "set of hands" in the lab has made my doctoral journey an overall positive experience. Additionally, I would like to acknowledge my graduate committee, Prof. Youngblood, Prof. Erk, and Prof.

Mansson. I appreciate the direction and support given by all of you over the past four years and for some the past eight years. I also want to thank my collaborators, Sami-El Awad Azrak, Endrina Forti, Dr. Md Nuruddin, Brandon Mackey, Prof. Michael Sangid, and Prof. Chia-Chih Chang, for assistance on research projects throughout my doctorate.

While on the topic of DRG, I would like to thank my fellow graduate student lab mates: Hyeyoung Son, Naomi Deneke, Jared Gohl, and Hyungyung Jo. Thank you for all of the help in the lab you have provided me over the years, but more importantly, thank you for the encouragement and feedback. The unsung heroes of many research groups are the undergraduate research assistants. Without them, finishing my Ph.D. may have taken twice as long. That being said, I would like to thank Ricardo Rodriguez, Juan-Carlos Cardenas, Andrew Weiss, and Hugh Grennan.

For financial support, I would like to thank Purdue University, the Purdue Research Foundation, the GAANN Fellowship, the College of Engineering Dean's Teaching Fellowship, and the Indiana Department of Transportation. Thank you for supporting me through my Ph.D.

Next, I would like to share my personal acknowledgments, starting with family. So much credit for having the ability to write a dissertation goes to my mom and dad. A few lessons that they instilled in me at an early age have carried with me throughout my lifetime. The biggest one comes from my mother. She taught me that when you do something, you do it with excellence. I remember back in middle school when paragraphs were defined by a number of sentences. My mom would always make me write the maximum number of sentences that made up a paragraph. As silly of a lesson as this may seem, over the years and through many other examples, it has taught me the importance of doing things with excellence. My dad has always pushed me to be the very best version of myself and give my best effort in all I do. Lessons like these are very hard to appreciate when you are younger, but as an adult, there is significant value in these lessons. I am thankful that you have taught me these lessons, not just with academics, but in all aspects of life. Honestly, without the two of you, I doubt I would have had the capacity and drive to finish a Ph.D. I love you both very much.

To my Big bro, I definitely would not have gotten here without him and in many ways, I owe the man I am today to him. He was the first person to share with me about who Jesus is, and how much He desires to be in a relationship with me. For that I am grateful. Over the years, he

has provided me with wisdom and a voice of reason when times are uncertain. I want to acknowledge Michael and let him know that his little bro loves him.

I want to acknowledge my grandparents who are unable to read this, for the sacrifices they have made. They have always valued education, and I hope that they can be proud of this dissertation. Also, I want to thank my uncles and aunts; Uncle Bob and Aunt Debbie, Uncle Rich and Aunt Paula, Uncle Jim and Aunt Kim, Uncle John and Jess, Uncle Choup and Aunt Debbie, and Uncle Jim and Aunt Mary Ann; my cousins Katie, Chris, Quinn, Lauren, Jessica, Rob, Zack, Talon, Jimmy, Joey, and Julia who have provided me with laughter and cheer throughout my life.

Now onto the “In-Law” side of the family. Mama Sheen and Steve have provided so much support to me during my time in graduate school. Whether that is cooking a meal during busy times or just being there to listen to successes, I am very grateful for them. I also want to acknowledge my brothers and sisters-in-law; Craig, Lindsay, Adam, and Stephanie for their support during graduate school as well as my nephews and nieces; Caleb, Lucas, Maddie, Anna, and Peyton for bringing more joy into my life.

I want to thank and acknowledge my friends who have been there for me every step of the way. I want to give a big shoutout to C. Watson, K. Benkoil, B. Johnson, A. Topinka, J. Chow, C. Bush, L. Schrumpf, M. Churik, The Gainors, The Goodmans, The Nowickis, The Freeborns, The Robertses, The Hoovers, The McMunns, The Morses, The Welchs, and The Abells.

The culmination of everyone’s influence has encouraged me one way or another throughout my Ph.D. Although, none of this praise is justified without giving thanks to God who has been the One I have leaned on and turned to continuously throughout graduate school. I am grateful for the peace and calmness given to me by Your grace. Thank you for Your unconditional love. Finishing my dissertation is not a solo effort even though my name is the only author. I could not have achieved this without everyone acknowledged here and many more.

TABLE OF CONTENTS

LIST OF TABLES	9
LIST OF FIGURES	10
ABSTRACT	14
1. INTRODUCTION	15
2. A BUCKLING MECHANICS APPROACH TO ELASTIC MODULUS DETERMINATION OF GLASSY POLYMER FILMS	20
2.1 Introduction	20
2.2 Materials and Methods	24
2.2.1 Materials Preparation	24
2.2.2 Tensile Testing	25
2.2.3 FSCB Modulus Measurement Methodology	25
2.3 Results and Discussion	25
2.4 Conclusions	32
3. NANOCELLULOSE FILM MODULUS DETERMINATION VIA BUCKLING MECHANICS APPROACHES	33
3.1 Introduction	33
3.2 Materials and Methods	35
3.2.1 CNF Film Preparation	35
3.2.2 TOCNF Film Preparation	36
3.2.3 CNC Film Preparation	36
3.2.4 Tensile Testing	36
3.2.5 FSCB Testing	37
3.3 Results and Discussion	38
3.3.1 Establishing Buckling and Failure Criteria for Nanocellulose Films	38
3.3.2 E Determination by FSCB	41
3.3.3 Comparing FSCB and Tensile Testing for E Determination	43
3.3.4 The Effect of Stiffness on Measurement Precision Through FSCB	45
3.4 Conclusion	49

4. THE TAPE DRAPE TEST – A PRACTICAL AND NONDESTRUCTIVE WAY TO ASSESS ELASTIC MODULI OF PAVEMENT MARKING TAPES IN THE FIELD	51
4.1 Introduction.....	51
4.2 Materials and Methods.....	55
4.2.1 Tensile Testing E Determination.....	55
4.2.2 Three-Point Bend E Determination	56
4.2.3 Tape Drape E Determination.....	57
4.3 Results and Discussion	60
4.3.1 E Determination Technique Comparison	60
4.3.2 Tape Geometry and Composition Effects on E Measurement Techniques.....	63
4.4 Conclusion and Implications.....	64
5. A METHODOLOGY FOR CALIBRATING MECHANOPHORE ACTIVATION INTENSITY TO APPLIED STRESS.....	67
5.1 Introduction.....	67
5.2 Materials and Methods.....	71
5.2.1 Materials Preparation.....	71
5.2.2 Methodologies	73
5.3 Results and Discussion	77
5.3.1 MP Activation Near a Glass Particle	77
5.3.2 FEA Simulations of a Rigid Inclusion Imbedded in a PDMS/SPN Matrix.....	81
5.3.3 Characterizing the I and σh Concentration Gradients	82
5.3.4 The Methodology for Calibrating I to σh	85
5.3.5 Calibrating I to σ with Different Stress States and MP Concentrations	88
5.4 Conclusion	92
CONCLUSIONS.....	94
REFERENCES	97

LIST OF TABLES

Table 3-3-1. Nanocellulose Film Thicknesses.....	38
Table 4-1. Comparison of E Determined by Various Test Methods	61

LIST OF FIGURES

Figure 1-1. Examples of either employing old ideas new to new problems, such as employing *a*) a non-destructive technique designed to test the “handle” of fabrics from 1930⁸ to *b*) determine the elastic modulus of aged paper in 2018 without damaging the samples for the preservation of antique documents and affidavits⁹, or employing new technologies to solve current problems by *c*) implementing MPs into a wind turbine blade materials system to predict premature or unforeseen failure¹². Reproduced (a) from ref. 7 with permission from Taylor & Francis Group, copyright 1930, (b) ref. 8 with permission from The American Society of Mechanical Engineers, copyright 2018, and (c) ref. 12 with permission from the Royal Society of Chemistry, copyright 2020..... 16

Figure 1-2. Images showing a color change with increasing force due MP activation in an elastomer (*left*), and schematics of MP activation at the molecular level as force increases (*right*).¹² Reproduced from ref. 12 with permission from the Royal Society of Chemistry, copyright 2020. 18

Figure 2-1. A schematic representation of *a*) an unbuckled and *b*) a buckled film with the key dimensions illustrated. *c*) Representative force, P , vs. change in displacement, Δx , experimental result for a typical buckling experiment. The red dashed lines show the tangent intersection approach used to determine the critical buckling load, P_{cr} . The black dashed line shows the displacement at which the film buckled, and the critical buckling load is labeled, P_{cr} 22

Figure 2-2. *a*) Experimental setup schematic. *b*) Top down image of experimental setup showing mechanical stage used for critical buckling measurements. Oblique and top down images of a film before (*c* and *e*) and after (*d* and *f*) it reaches P_{cr} 26

Figure 2-3. An Euler curve for the PET samples. The black points represent the experimental column. The grey points represent estimated points to show a complete curve, as these slenderness ratios were not experimentally tested. The black line displays the yield stress. 27

Figure 2-4. The effect of changing sample width and length on critical buckling load for PET. *a*) constant length of 28 mm while the film width was changed (black squares) and a constant width of 15 mm while the film length was changed (gold circles) are shown. *b*) The relationship of critical buckling load and b/a^2 . Open symbols indicate tentative results due to the sensitivity limits of the instrument. 29

Figure 2-5. *a*) The average elastic modulus of each individual film geometry for PET. The black line represents the buckling modulus average and the gray shaded region is one standard deviation from the buckling average. The red line represents the tensile modulus average and the red shaded region is one standard deviation from the tensile average. *b*) The $E_{FSCB}:E_{Tens}$ ratio of each film geometry for all materials. 30

Figure 2-6. The comparison between thin plate and column buckling mechanics approaches for calculation of elastic modulus of the system. The same material was used for all experiments with (theoretically) the same modulus. The apparent change in modulus with aspect ratio of the sample by the thin plate buckling analysis (blue data points) indicates that one or more assumptions associated with this approach are not appropriate here. 31

Figure 3-1. Images of rectangular laser cut <i>ai</i>) unpressed CNF, <i>aii</i>) pressed CNF, <i>aii</i>) TOCNF, and <i>aiv</i>) CNC films for buckling. <i>bi</i>) A top and <i>bii</i>) side view schematic and image of the experimental set-up for buckling.	37
Figure 3-2. An Euler curve for the nanocellulose films. The horizontal lines represent the yield stress or fracture stress depending on the film type (corresponding to the colors in the legend). The dotted line has a slope of -2 and is a guide to the eye.....	40
Figure 3-3. <i>a</i>) Representative force-displacement curves for P_{cr} determination using the LI methodology for all film types. Note the break in the y-axis. <i>b</i>) Representative $v(x)$ vs. $v(x)/P$ curves for P_{cr} determination using the Southwell methodology for all film types.	42
Figure 3-4. <i>a</i>) P_{cr} for the LI and Southwell methods at the largest thickness for each film type. Note the break and change in scale in the y-axis. <i>b</i>) E for the LI method, the Southwell method, and tensile testing approaches at the largest thickness for each film type. The filled rectangle with the dotted outline denotes the range of reported literature values of the CNC tensile modulus. ^{27,73} The error bars represent one standard deviation of the average in both plots.	44
Figure 3-5. <i>a</i>) The effect of thickness on P_{cr} for both the LI (filled) and Southwell (open) methods. <i>b</i>) A modified Euler curve. <i>c</i>) K dependence on sample geometry. <i>d</i>) The effect of thickness on E for both the LI (filled) and Southwell (open) methods. The dashed lines in <i>b</i>) and <i>c</i>) have a slope of one and are a guide to the eye. The error bars represent one standard deviation of the average.	47
Figure 4-1. Representative images of TPM tapes. A macroscopic image of the <i>ai</i>) back, <i>aii</i>) front, and <i>aiii</i>) cross-sectional image of Tape 1. A macroscopic image of the <i>bi</i>) back, <i>bii</i>) front, and <i>biii</i>) cross-sectional image of Tape 2 with labels of structural features. A macroscopic image of the <i>ci</i>) back, <i>cii</i>) front, and cross-sectional image <i>ciii</i>) through a raised ridge and <i>civ</i>) away from a ridge.	52
Figure 4-2. Experimental set-ups of <i>a</i>) tensile testing, <i>b</i>) three-point bend testing, and <i>c</i>) Tape Drape Testing.....	56
Figure 4-3. An example of the ImageJ analysis used to determine θ for the Tape Drape Test. <i>a</i>) The angle tool was selected from the toolbar at which point <i>b</i>) a line was drawn from the edge of the table (point S) to the specifying the endpoint of the tape to the horizontal (point O). <i>c</i>) A second horizontal line was drawing starting from the edge of the table (point S) which established the horizontal to calculate θ which equaled 27.9° in this example.	58
Figure 4-4. <i>a</i>) Tape Drape Testing plot of c with respect to θ . <i>b</i>) The scaling relationship between $f(\theta)$ and l_h . The parallel dashed lines have a slope of -1/3 and are a guide to the eye. The error bars in <i>a</i>) and <i>b</i>) represent a standard 5% measurement error.	59
Figure 4-5. <i>a</i>) Representative force-displacement curves from tensile testing. <i>b</i>) Representative force-deflection curves from three-point bend testing. <i>c</i>) Initial portion of representative stress-strain curves from tensile testing. <i>d</i>) Initial portion of representative bending stress-bending strain curves from three-point bend testing. The legend in <i>b</i>) applies to all plots.....	61
Figure 4-6. The measured E from tensile testing, three-point bend testing, and Tape Drape Testing for each tested tape. The error bars represent one standard deviation.	62

Figure 5-1. Experimental approach for calibrating experimental MP activation to stress using FEA. *a)* Progression of MP activation as uniaxial force is applied to the PDMS/MP system. The similar behavior of *b)* experimental MP activation near a glass particle in a PDMS/MP system with associated *c)* stresses determine through FEA simulations of an identical system. By combining the MP activation in *b)* and the determined stresses from *c)*, *d)* a calibration between MP activation intensity can be determined by the slope of the curve once MP activation is observable. 68

Figure 5-2. Schematics and actual images of the experimental set-up. Schematics of *a)* the coupling of the mechanical testing and confocal microscopy using a 552nm laser and *b)* a PDMS/SPN embedded with a glass particle sample mounted for testing. Actual images of *c)* the mechanical testing frame coupled with a confocal microscope and a close-up of *d)* a PDMS/SPN sample with a glass particle embedded mounted for testing in the grips. 71

Figure 5-3. The reaction for synthesizing diene functionalized spiropyran. 72

Figure 5-4. $\sigma_{global} - \varepsilon$ behavior of the PDMS/SPN materials system when testing with the dropped down grips (before and after correcting for σ_{bend} and ν) and manufactured grips. 74

Figure 5-5. The finite element model for the PDMS/MP system. *a)* The mesh near the PDMS/MP glass bead interface (highlighted in red). *b)* The mesh of the PDMS/MS system with a glass particle. *c)* The axially loaded boundary conditions applied to the PDMS/MS system. 76

Figure 5-6. The mechanical behavior of the PDMS/SPN matrix embedded with a glass particle of different interfacial adhesion and corresponding confocal microscopy images as ε increases. *a)* Stress-strain curves of a PDMS/SPN with an imbedded glass particle with different interfacial adhesions. Images of the PDMS/SPN-glass particle behavior as ε increases for different interfacial adhesions with *b)* being the very high adhesion, *c)* being the high adhesion, *d)* being the medium adhesion case, and *e)* being the low adhesion case. 78

Figure 5-7. Relating and characterizing I with FEA determined σ_h as a function of x_2 and x_1 . Images comparing *ai-v)* the MP activation response and *bi-v)* the FEA determine σ_h concentration gradient for the high adhesion case. I as a function of *c)* x_2 and *d)* x_1 . The FEA determined σ_h as a function of *e)* x_2 and *f)* x_1 83

Figure 5-8. The UV activated calibration curves for intensity normalization of PDMS functionalized with 0.5wt%, 0.6wt%, and 0.7wt% SPN. The yellow data intensity values were taken a higher gain and laser power to increase sensitivity. The red dotted lines show how the normalization value was determined for each calibration curve. 84

Figure 5-9. The methodology for calibrating MP activation to stress. *a)* The calibration curve of I to σ_h . The solid black lines show the activation regimes as strain increases. *b)* The change in I with respect to σ_h as ε increases. The dashed black lines show the activation regimes. The unfilled data points represent I taken at different microscope settings. *c)* The comparison of the MP activation to σ_h calibration depending on the stress state. The yellow data points represent the stress state of the high adhesion case in the 2 direction and the blue data points represent the low adhesion case in the 1 direction. *d)* The comparison of the I to σ_h calibration depending on SPN concentration. The calibration was taken for the low adhesion case in the 1 direction. 86

Figure 5-10. $\sigma_{global} - \varepsilon$ results for a PDMS system functionalized with 0.5wt%, 0.6wt%, and 0.7wt% SPN. No change is observed in the mechanical behavior. 89

Figure 5-11. The change in I with respect to σ_h as ε increases showing the artificially high determined I to σ_h calibration value for the 0.5wt% system taken at higher imaging settings.... 91

ABSTRACT

In order for new materials to be implemented into industrial practice, rigorous characterization and performance assessment must be conducted. The ability to accurately characterize and assess these new materials is directly related to the delay between material development and implementation. Traditionally utilized characterization techniques may not be an appropriate method to characterize a material or materials system, thus warranting the development of new characterization and performance assessment techniques. For swift implementation of novel materials and materials systems, characterization and performance assessment methodologies must be developed simultaneously.

While many new materials characterization techniques have been developed over the past years, one area in need of further development is mechanical characterization techniques. For newly developed materials, understanding and accurately predicting the mechanical performance is essential for personnel safety and for preventing unexpected materials failure. The work presented here focuses on the development of mechanical characterization techniques employing two strategies: repurposing old tools and techniques to solve new problems and developing new tools and techniques to solve old problems.

By using the first strategy, classical buckling mechanics were deployed to create a robust elastic modulus characterization technique for brittle, glassy polymer films, and a technique developed to determine the “handle” or drape of textiles was repurposed to characterize the elastic modulus of temporary pavement marking tape to assess adhesion performance. Through the second strategy, newly developed molecules called Mechanophores (MP) that exhibit a color or fluorescence change upon the application of a mechanical stimulus are being considered for self-reporting damage sensing applications in polymeric material systems. The elicited fluorescent MP response increases with applied stress allowing for real time damage sensing that can prevent unexpected material failure. Here, a methodology is presented that calibrates the fluorescence MP response to applied stress. These strategies and methodologies can either be utilized or used as inspiration by other engineers for the development of material characterization methods for the rapid implementation of new materials into industrial practices.

1. INTRODUCTION

Before new polymer materials are implemented into industry, extensive materials characterization must be performed to fully understand material composition, structure, and properties to ensure proper performance upon application. As polymeric materials and technologies advance to satisfy industry needs, traditionally utilized techniques and methodologies cannot always be relied upon for materials characterization or materials performance assessments. The advancement and development of material characterization and assessment methodologies must occur simultaneously with the advancement and development of new materials otherwise implementation into industrial practices will be delayed.¹⁻⁴

To push forward the implementation of novel polymeric materials into industry, criteria for material characterization and assessment techniques are as follows: techniques must have a high sample throughput, be easy to implement into an industry setting, and have an easy data analysis procedure for rapid results. While many characterization techniques have been developed to fit this need⁵⁻⁷, one such area in need of further research and development are mechanical characterization techniques. Completely understanding how new materials will mechanically perform before implementation guarantees safety for personnel and mitigates unanticipated operation and materials costs caused from replacing failed or damaged materials systems. The work presented here focuses on the development of mechanical characterization techniques for novel or complex polymeric material systems.

Here, two possible strategies for the development of new mechanical characterization methodologies are elaborated upon. The first strategy is to repurpose old ideas, tools, and/or technologies for application outside the original scope to address new problems. For example, utilizing a technique that was created to determine the drapeability of textiles⁸ (Figure 1-1a) to instead determine elastic moduli of fragile polymeric materials or layered materials consisting of several different polymers, such as aged paper or industrial strength tapes (Figure 1-1b).⁹ The other strategy is to employ new ideas, tools, and technologies to solve older problems. For example, the development of molecular force sensors can forecast premature failure of expensive polymeric materials systems acting as real time self-reporting damage sensors (Figure 1-1c).¹⁰⁻¹²

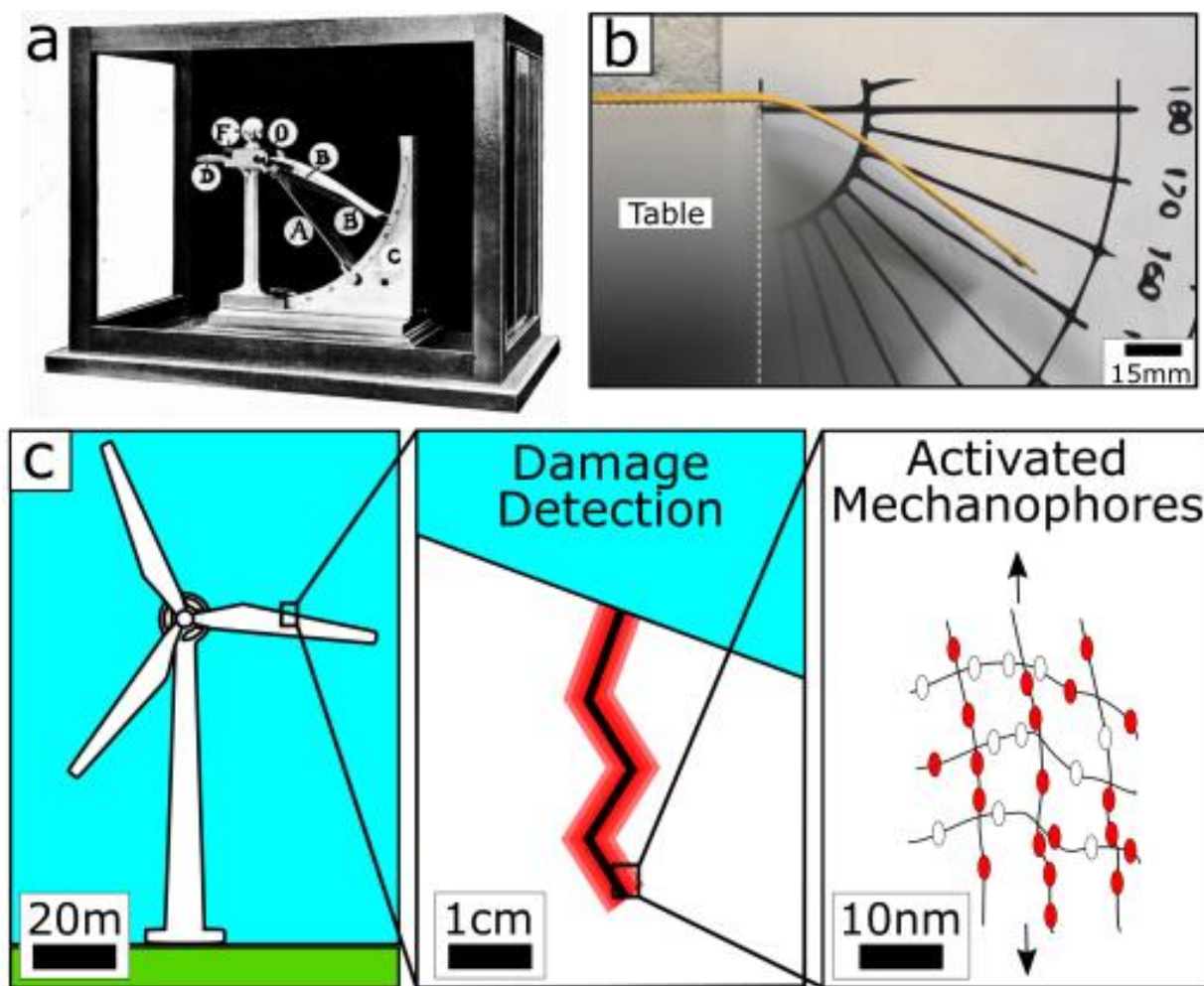


Figure 1-1. Examples of either employing old ideas new to new problems, such as employing *a*) a non-destructive technique designed to test the “handle” of fabrics from 1930⁸ to *b*) determine the elastic modulus of pavement marking tape in 2020 for the assessment of adhesion performance on asphalt roadways, or employing new technologies to solve current problems by *c*) implementing MPs into a wind turbine blade materials system to predict premature or unforeseen failure¹². Reproduced (a) from ref. 7 with permission from Taylor & Francis Group, copyright 1930, and (c) ref. 12 with permission from the Royal Society of Chemistry, copyright 2020.

Here, both of these routes are taken to develop mechanical characterization techniques of complex or novel material systems. Classical buckling and bending mechanics from Timoshenko¹³, Peirce⁸, and Southwell¹⁴ were reexamined and repurposed to develop techniques that characterize the elastic modulus of glassy polymer thin films or layered structures consisting of several different polymers. Elastic modulus is a crucial materials property to characterize as it greatly influences many mechanical behaviors such as stress-strain behavior, fracture toughness, and adhesion.¹⁵ Through revisiting and applying classical buckling and bending mechanics in innovative ways,

novel elastic modulus characterization techniques were developed. The new techniques presented here are a valid primary or alternative methods to determine the elastic modulus of structurally complex or glassy and brittle polymeric materials.

Molecular force sensors known as mechanophores (MP) have emerged over the past decade to be applied as real time self-reporting damage sensors for polymeric materials.^{12,16} When a polymeric material imbedded with MP undergoes damage, the MP activates creating a color change or fluorescent response.^{17,18} (Figure 1-2) The change in color or fluorescent caused by MPs activating is typically observed through microscopy as an intensity.¹⁹ If MP activation intensities can be calibrated to applied stresses, MPs can be used as an quantitative real time assessments of applied stress in polymeric materials. By utilizing finite element analysis (FEA) local stress values are able to be quantified to be correlated with and MP activation intensities. By coupling these two quantities, a systematic methodology for calibrating MP activation to applied stress can be created. Creating a method to calibrate MP activation to applied stress enables MPs to be employed as quantitative self-reporting damage that will mitigate unexpected material failure.

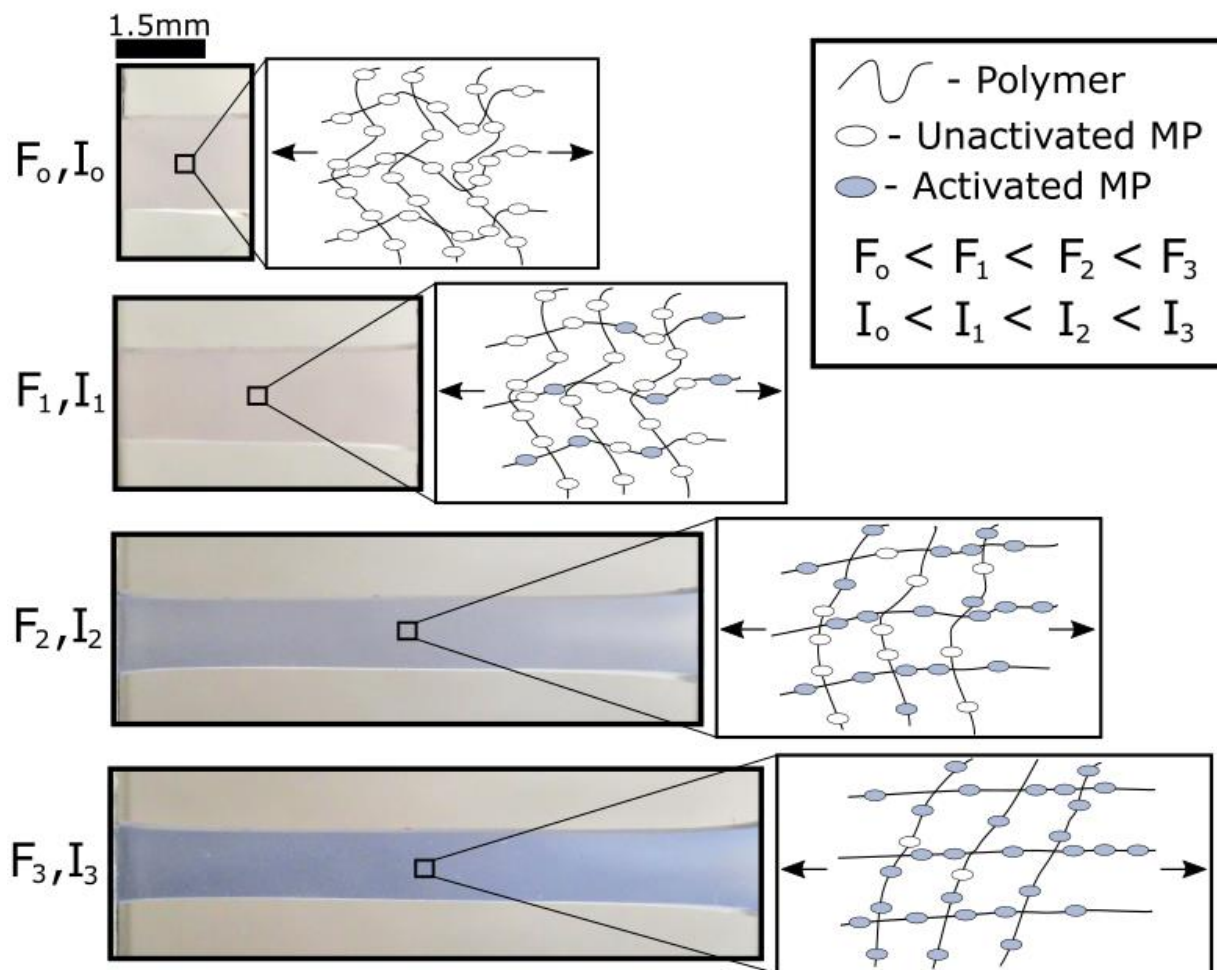


Figure 1-2. Images showing a color change with increasing force due to MP activation in an elastomer (*left*), and schematics of MP activation at the molecular level as force increases (*right*).¹² Reproduced from ref. 12 with permission from the Royal Society of Chemistry, copyright 2020.

Advancements in polymeric materials characterization and assessment techniques must progress alongside novel polymer material advancements to avoid delays in next generation materials implementation. While several new material characterization and assessment techniques have been implemented recently, mechanical characterization and assessments have not progressed as quickly. New mechanical characterization techniques have been developed by using classical buckling and bending mechanics to determine the elastic modulus of structurally complex or thin, glassy polymeric materials or by calibrating MPs with applied stress as a real time damage sensing assessment technique to address industry problems related to premature material failure.

In this dissertation, a buckling mechanics approach to characterize the elastic modulus of glassy thin films is presented. Through changing film length and width and by testing multiple glassy film material types the mechanics used in the methodology is validated. To confirm the accuracy of the determined moduli, the values were compared with moduli values determined through tensile testing which were found to have good agreement.

This buckling approach to determine elastic moduli of glassy polymer films was elaborated on further to assess potential materials or sample geometry limitations by testing a variety of nanocellulose films with different thicknesses. The buckling mechanics approach was found to be most effective for the stiffest, most brittle films as well as thicker films. Additionally, strategies are discussed to overcome sample geometry and stiffness limitations that enable the methodology to remain effective in determining the elastic modulus.

Through using a cantilever bending test developed in 1930, a practical way to measure the elastic modulus of temporary pavement marking (TPM) tapes, called “The Tape Drape Test” was developed. Tensile testing and three bend testing were employed to compare moduli determined by the three techniques. The Tape Drape Test was most effective, compared to tensile and three point bend testing, in determining the elastic modulus of three different commercial TPM tapes. Therefore, Tape Drape Test was determined to be the most suitable method for determining the elastic modulus of TPM tapes.

Lastly, A systematic methodology to calibrate MP activation intensities to applied stress is presented. FEA simulations were used to determine local hydrostatic stresses near a rigid particle in an elastomeric matrix and laser scanning confocal microscopy was used to experimentally determine the MP activation intensities near a glass particle in an elastomeric matrix as strain increased. By using distance from the particle interface as a correlator the two quantities were related. After the onset of MP activation, a linear relationship between MP activation and hydrostatic stress was found where the slope was taken as the calibration value. The robustness of the methodology was investigated by determining the MP activation to stress calibration value for different stress states and material systems. The methodology is shown to have the ability to calibrate MP activation intensity with applied stress for any MP functionalized polymer system.

2. A BUCKLING MECHANICS APPROACH TO ELASTIC MODULUS DETERMINATION OF GLASSY POLYMER FILMS

Reprinted (adapted) with permission from (Rencheck, M. L., Rodriguez, R., Miller, N. A. & Davis, C. S. A buckling mechanics approach to elastic modulus determination of glassy polymer films. *Journal of Polymer Science, Part B: Polymer Physics* (2018). doi:10.1002/polb.24755.) copyright 2018, John Wiley & Sons, Inc.²⁰

2.1 Introduction

Glassy polymer thin films are utilized in a host of industries ranging from commodity applications, including food packaging and protective coatings^{21,22}, to advanced uses, such as encapsulants for microelectronics^{23,24} and solar panels²⁵. However, a major engineering challenge lies in understanding and controlling the mechanical and fracture properties of these materials. Glassy thin films tend to be brittle, with a low elongation to failure, limiting the measurement techniques that can be used to determine their mechanical properties. Brittle polymer films have limited extensibility from hindered chain mobility due to their glassy nature at room temperature. The limited chain mobility can cause fracture at low strains under tensile deformation²⁶, making modulus determination difficult.

Additionally, due to their brittle nature, these films require careful sample preparation and mounting. Sample handling and mounting can lead to sample damage prior to testing, further complicating mechanical property measurements. Previous work on the tensile testing of brittle films has required a metal support frame to facilitate sample handling and mounting to prevent damage prior to testing.^{27,28} While innovative and effective, the extensive sample preparation required to mount each film sample in a metal frame is not practical for high throughput characterization.

In addition to tensile testing, two other elastic modulus characterization techniques for thin films are nanoindentation and surface wrinkling.^{29,30} Nanoindentation is a method that uses an area function with respect to penetration depth along with loading and unloading curves to determine the modulus.^{31,32} Though useful for hard materials, nanoindentation has difficulty measuring polymeric materials due to viscoelasticity as the contact area will be dependent upon time creating differences between actual and calculated values.³³

Surface wrinkling can be used to characterize the elastic modulus of brittle polymer thin films supported on an elastic substrate using buckling mechanics. In 2004, Stafford et al. developed a technique that utilizes strain-induced elastic buckling instabilities for modulus measurements.³⁴ In this technique, a compressive load is applied to a bilayer sample (comprised of a thin-glassy film adhered to a thick elastic substrate) until surface buckling or wrinkles are observed. The resulting wrinkle wavelength is directly related to the elastic modulus of the film.

Although the surface wrinkling modulus measurement technique is highly effective for characterizing the modulus of brittle polymers, this method is only appropriate under certain conditions. Films with thicknesses exceeding 1 μm cannot be characterized through surface wrinkles^{34–37}, the film must be fully adhered to the substrate, requiring specific interfacial interactions between the two materials. Additionally, sample preparation for this methodology can be more onerous than for more straightforward methods, such as tensile testing, as it requires thin film floating and attachment to soft substrates.

To improve upon these testing restrictions, a technique that uses a single material with minimal sample preparation and analysis is presented here. The surface wrinkling technique described above has demonstrated that brittle film buckling instabilities can be used to reliably determine the modulus of elasticity. Drawing inspiration from these substrate-supported surface buckling modulus measurements, free-standing film buckling mechanics with fixed end conditions were examined in the present work. A schematic representation of a free-standing column before and after buckling can be seen in Figure 2-1a-b.

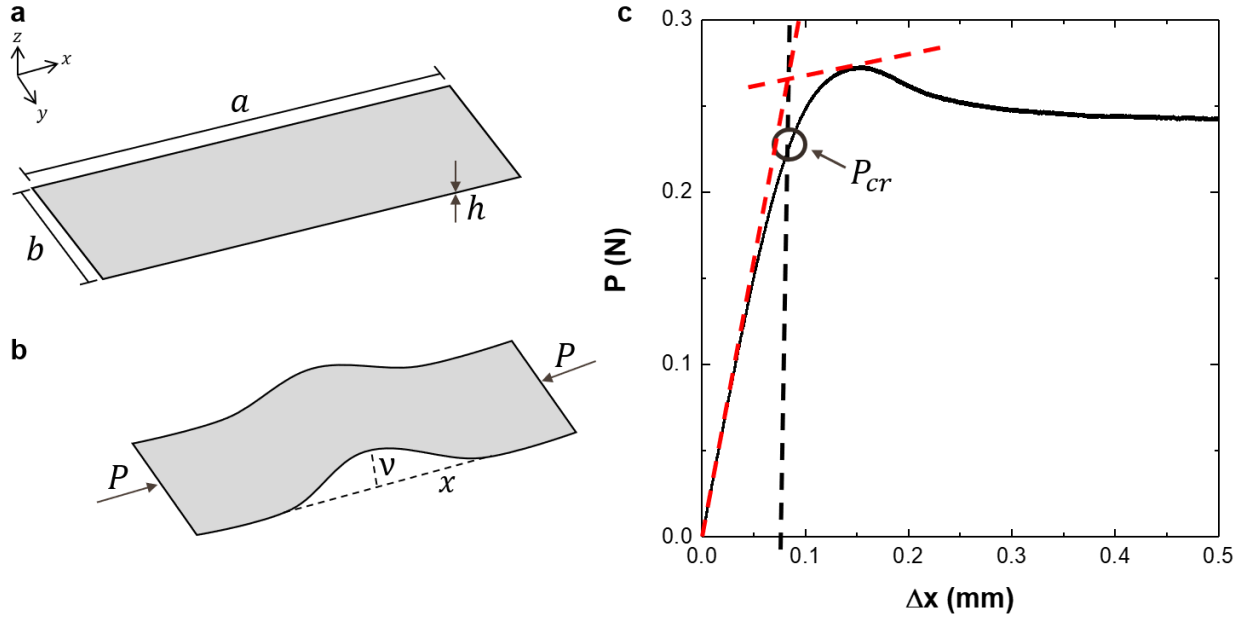


Figure 2-1. A schematic representation of *a*) an unbuckled and *b*) a buckled film with the key dimensions illustrated. *c*) Representative force, P , vs. change in displacement, Δx , experimental result for a typical buckling experiment. The red dashed lines show the tangent intersection approach used to determine the critical buckling load, P_{cr} . The black dashed line shows the displacement at which the film buckled, and the critical buckling load is labeled, P_{cr} .

To further understand this idea, free standing column buckling (FSCB) must be looked at in detail. By combining the moment and deflection expressions derived by Euler for FSCB, a relationship between the curvature of the buckle ($\frac{d^2v}{dx^2}$), the applied load (P), the deflection of the column (v), moment of inertia ($I = \frac{h^3b}{12}$ where b is the width and h is the film thickness), and the elastic modulus (E), can be obtained (Eq 2-1).^{13,38} The assumptions made for this derivation are that the columns are elastic and that small initial deflections are negligible.

$$\frac{d^2v}{dx^2} = \frac{-Pv}{EI} \quad (2-1)$$

Eq. 2-1 can be solved by assuming $v(x) = 0$ at both ends of the column to relate the critical buckling load (P_{cr}), effective column length (a_e), buckling mode (n), I , and E .¹³

$$P_{cr} = \frac{n^2\pi^2EI}{a_e^2} \quad (2-2)$$

The end conditions of a column determine the effective column length. The curvature of the deflection is symmetric about the midpoint. In this work the ends of the column are fixed. For

fixed ends, the curve begins to deflect at a distance of $a/4$ from each side of the deflection midpoint when buckling occurs which causes an effective length for the buckled column of one half of the column length.¹³ Other end conditions may be utilized but will result in a different a_e .

Rearranging Eq. 2-2, a relationship of sample geometry, E , and P_{cr} can be obtained.

$$P_{cr} = \left(\frac{\pi^2 h^3}{3} \right) E \left(\frac{b}{a^2} \right) \quad (2-3a)$$

$$E \sim P_{cr} \left(\frac{a^2}{b} \right) \quad (2-3b)$$

Eqs. 2-3a and 2-3b show the elastic modulus of an elastically buckled column is a function of P_{cr} and column geometry. For a given material, E is constant so P_{cr} should vary solely with sample geometry.

As for all new measurement systems, sources of error exist and must be identified to validate the technique. the free-standing column buckling (FSCB) modulus measurement yielded some experimental error. In FSCB, possible sources of experimental error have been discussed extensively in previous works.^{13,39} One possible source of error that likely impacted the present study is the initial curvature in the positive or negative z direction of the column before testing. An initial curvature can lead to prestrain within the column prior to testing, impacting the onset of buckling and resulting in a lower critical buckling load.⁴⁰ To mitigate initial curvature, the stages were adjusted after sample mounting to ensure the sample laid flat before testing.

Another potential source of experimental error can be caused by heterogeneities and defects in the material. Two of the most common sources of heterogeneity in the present system are attributed to variability in edge conditions due to sample preparation and variability in film thickness. The free edges of some samples were cut by hand with a razor blade. Cutting with a blade can result in small jagged tears or defects along the edges if care is not taken in sample preparation. While the scatter of the FSCB modulus data is greater than that of the elastic modulus determined by tensile testing, significant improvements to the experimental technique have reduced the error in the measurement system, allowing the elastic modulus of all films to be determined.

A more accurate value of P_{cr} can be calculated using a Southwell plot.^{41,42} This approach relates ν to the ratio of P_{cr} to the applied load (P_{app}). By measuring ν and P_{app} values, before P_{cr} occurs, the P_{cr} for that column can be determined graphically by taking the slope of linear

relationship between ν and $\left(\nu/P_{app}\right)$ when plotted.^{14,39} However, Southwell plots were not utilized in this work, but are used in Chapter 2, because determination of small deflections before reaching P_{cr} for each test requires specialized equipment and adds a significant level of complexity to the experimental setup, which contradicts the goal of developing a simple, straightforward modulus measurement technique presented here in Chapter 2.

Several different film materials were tested using FSCB to characterize the elastic modulus. Polyethylene terephthalate (PET) films were characterized extensively. PET was selected as the primary material to validate the measurement approach since it is a relatively tough, glassy polymer. Its toughness allows for orthogonal tensile characterization of the elastic modulus while its elastic modulus is similar to other brittle polymer moduli. Additional FSCB testing was conducted on films of polystyrene (PS) and hydroxyl-functionalized cellulose nanofiber (CNF).

FSCB modulus measurement relied on a buckling instability through a compressive load, which allowed the elastic modulus to be determined prior to the onset of plastic deformation. The technique is simple in sample preparation and post-testing analysis. In this study, the FSCB modulus measurement approach is validated using a variety of polymer films. For a given material over a range of sample geometries, P_{cr} is shown to vary proportionally with the length and width while the elastic modulus is expected to remain constant for a given material, independent of geometry. FSCB has the potential to be a simple and straightforward technique to characterize the elastic modulus of micron thick films that are difficult to handle and test tension.

2.2 Materials and Methods

2.2.1 Materials Preparation

PET (Transparency Film, 3M), PS (Sigma Millipore), CNF films were used for all experiments. Rectangular samples were cut into varying geometries with the width ranging from 4 mm to 18 mm and length ranging from 15 mm to 60 mm using a sliding blade cutter or laser cutter (MUSE, Full Spectrum). The geometries were restricted to these ranges based on the size of the mechanical buckling stage. The prepared samples had aspect ratios (a/b) ranging from 1 to 7. The film thickness was characterized with a confocal microscope (Leica SP8).

2.2.2 Tensile Testing

Dogbone specimens were prepared by hand cutting and laser cutting. The gauge width was 8 mm for PET and 1.5mm for PS and CNF. The gauge length was 35 mm for PET, and 12mm for PS and CNF. Tensile testing was performed on an ADMET MTEST Quattro with a strain rate of 0.015 s^{-1} for PET samples and a Psylotech μ TS for PS and CNF with a strain rate of 0.008 s^{-1} .

2.2.3 FSCB Modulus Measurement Methodology

A custom-built mechanical buckling stage was utilized for all buckling experiments. It was comprised of a miniature load cell (Futek S-beam, 50 g), a fiber optic displacement sensor (Philtec), and two linear piezo motorized stages (Newport). The experimental set-up is shown in Figure 2-2a-b. For the buckling tests, the compressive load was taken as positive. The sampling rate of the load cell was 960 s^{-1} . Each sample was mounted in the center of the sample holders with cyanoacrylate glue (Loctite). A $18\mu\text{L}$ drop of glue was placed in the middle of the sample and spread over the entire area of the sample holder with a cotton swab, forming a liquid glue layer approximately $5\text{ }\mu\text{m}$ thick. The glue was allowed to dry in air for 5 minutes before beginning each test. For each test, a compressive load was applied at a fixed displacement rate of $0.05\text{ mm}\cdot\text{s}^{-1}$. After the onset of buckling, an additional displacement of 0.5 mm was applied. For every trial, a new film was prepared and mounted. A minimum of 3 trials were conducted for each film geometry.

2.3 Results and Discussion

A custom mechanical testing frame was employed to measure the load and displacement of each sample as it was compressed and subsequently buckled. A schematic and photo of the experimental setup is given in Figure 2-2a-b, respectively.

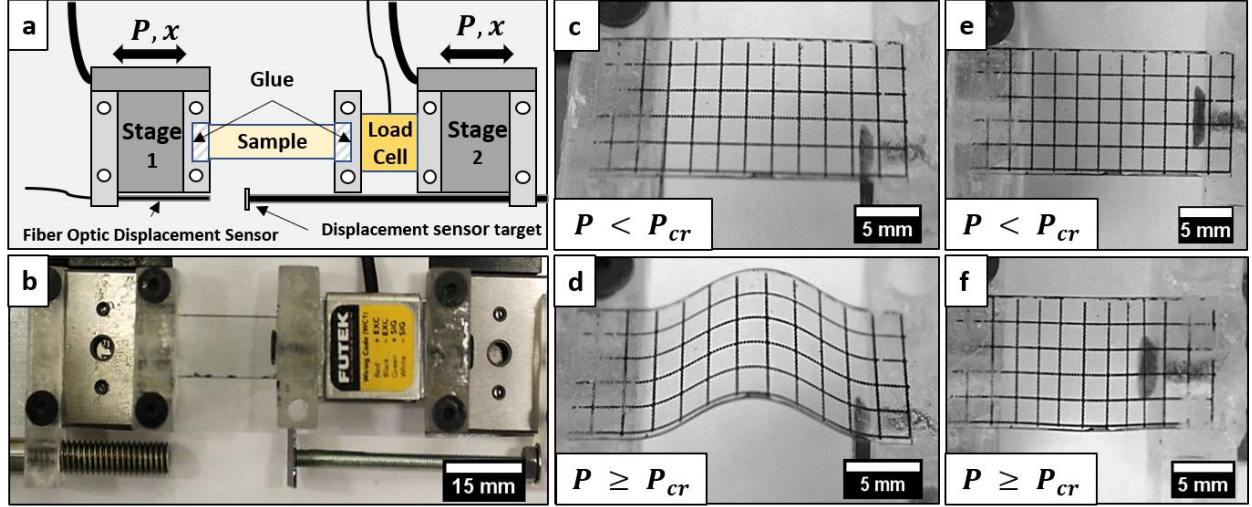


Figure 2-2. a) Experimental setup schematic. b) Top down image of experimental setup showing mechanical stage used for critical buckling measurements. Oblique and top down images of a film before (c and e) and after (d and f) it reaches P_{cr} .

PET, PS, CNF films of varying geometries were prepared with widths ranging from 4 mm to 18 mm and lengths ranging from 15 mm to 55 mm. The thickness of PET was held constant at $82.6 \pm 0.9 \mu\text{m}$, PS was held at $123.0 \pm 3.0 \mu\text{m}$, and CNF was held at $53.3 \pm 1.0 \mu\text{m}$. The standard deviation of the measured film thickness was roughly 2 % of the average value. Each sample was mounted and deformed laterally until a buckling instability occurred. A schematic of a typical film before buckling can be seen in Figure 2-1a and after buckling in Figure 2-1b. Figure 2-2c-f displays a PET film with a grid pattern before and after reaching P_{cr} showing that there is only a significant buckling mode in the x-direction. The FSCB elastic modulus method is strongly dependent on film thickness, given the third order relationship ($P_{cr} \sim h^3$) shown in Eq. 2-3a. Small variations in film thickness could potentially lead to significant variability of the elastic modulus measurement.

In this study, films were mounted to the translating stages with an air-curing glue. While great care was taken when mounting each sample to help mitigate experimental error, the mounting process has the potential to add significant error to the measurement system. There is potential variation in the amount of glue, pressure placed on each film during mounting, and the contact angle formed by the liquid glue flowing beneath the film before hardening (which could bias the buckling direction or lead to an unbalanced compressive load through the thickness of the sample).⁴³

The compressive load and displacement for a representative test are plotted in Figure 2-1c. As the distance between the fixed ends of the film decreases, buckling occurs when the lateral compressive load reaches P_{cr} . The P_{cr} is taken as the critical point indicated in Figure 2-1c. P_{cr} was determined for each test by a two line intercept method. Here, the intersection of a line extrapolated from the initial linear portion of the curve prior to buckling and a linear fit plotted from just prior to P_{max} (defined by a 2% offset of the maximum load) through P_{max} was utilized to determine P_{cr} . Beyond the critical buckling load, the compressive load drops. After buckling occurs, the film maintains its buckled shape and the amplitude of the buckle increases continually as the ends of the film come closer together.

Film geometries must be carefully selected to avoid yielding/ plastically deforming before buckling during experimentation. When the buckling stress exceeds the yield stress (σ_y) of a material, the sample will plastically deform before buckling resulting in inaccurate modulus determination.³⁹ To identify the sample geometry required to avoid this premature plastic yielding, an Euler curve was constructed (Figure 2-3), which examines the critical buckling stress in relation to the slenderness ratio (related to a_e and h).

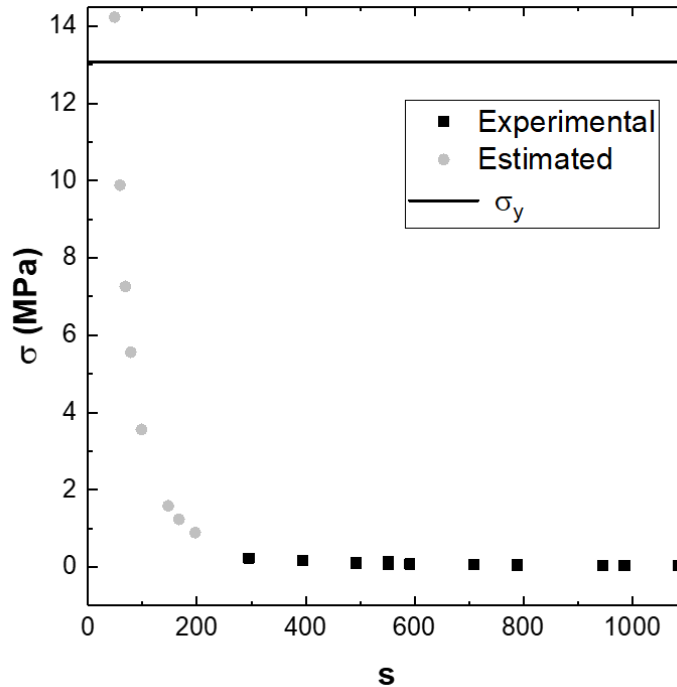


Figure 2-3. An Euler curve for the PET samples. The black points represent the experimental column. The grey points represent estimated points to show a complete curve, as these slenderness ratios were not experimentally tested. The black line displays the yield stress.

For the PET samples the σ_y was 13.07MPa and the maximum buckling stress (σ_{buck}) across all PET was 0.13MPa. All materials tested were ensured to buckle before plastically yielding. The greatest influencing factor on σ_{buck} occurring before σ_y is the slenderness ratio (s) which is defined as the ratio of a_e/r where r is the radius of gyration and can be simplified to $h/2\sqrt{3}$ for rectangular samples³⁹. When the curve meets σ_y , the elastic limit of the column has been reached. Typically a relatively large s value is needed for buckling to occur before yielding.³⁹ Therefore, care must be taken in designing specimen geometries, so the sample does not yield before buckling occurs. Typically for columns, a relatively large slenderness ratio is required to accurately predict P_{cr} .³⁹

The appropriateness of this FSCB modulus measurement approach can be seen by considering Eq. 2-3a. If b is varied while holding a and h constant, Eq. 2-3a shows that P_{cr} varies linearly with width ($P \sim b$). If b and h are fixed while varying a , P_{cr} varies inversely with length squared ($P \sim \frac{1}{a^2}$). Figure 2-4a-b highlights both relationships independently for PET films. As a increases, a decrease in P_{cr} is observed as the sample becomes more compliant. As b increases, an increase in P_{cr} is observed because the sample becomes stiffer. However, for both conditions, the material composition and, subsequently, the modulus remains constant. It should be noted that for the highest aspect ratio samples in this study, the sensitivity limit of the load cell was approached, resulting in significant error in P_{cr} (open symbols in Figures 2-4a-b).

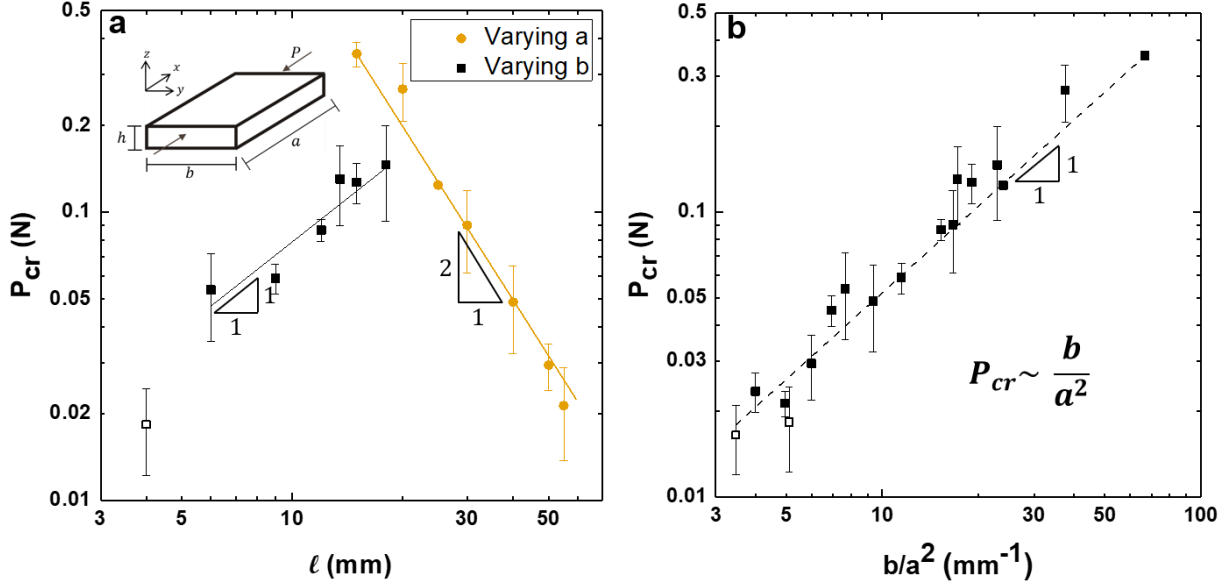


Figure 2-4. The effect of changing sample width and length on critical buckling load for PET. *a*) constant length of 28 mm while the film width was changed (black squares) and a constant width of 15 mm while the film length was changed (gold circles) are shown. *b*) The relationship of critical buckling load and $\frac{b}{a^2}$. Open symbols indicate tentative results due to the sensitivity limits of the instrument.

The effectiveness of the FSCB modulus measurement approach was further explored by examining the impact of changing length and width simultaneously on the critical buckling load. Figure 2-4b shows P_{cr} plotted against the width divided by the length squared, demonstrating that the measured data follows the relationship $\left(P_{cr} \sim \frac{b}{a^2}\right)$. The exponential fit in Figure 2-4b has a slope of unity, indicating that the buckling load varies as predicted by Eq 2-3a. For this data, the film thickness was held constant ($h = 82.6 \mu\text{m}$). The y-intercept of this exponential fit results in a modulus of 2.77 GPa for PET; this value is a rough estimation for the FSCB modulus measurement technique.

While E can be estimated from the intercept in Figure 2-4b, a more rigorous approach is to determine the elastic modulus for each tested geometry individually. The relationship of these individually calculated modulus values is given in Eq. 2-3b as a function of sample aspect ratio and P_{cr} . Averaging these individually determined moduli for PET resulted in a modulus of $E_{FSCB} = 3.06 \pm 0.58$ GPa, which is close to the tensile result of $E_{Tens} = 3.54 \pm 0.20$ GPa. Both average modulus results are shown as solid lines with shaded areas highlighting one standard

deviation in Figure 2-5a. To further illustrate the ability of the FSCB method to accurately measure film modulus, Figure 2-5b shows a ratio of $E_{FSCB}:E_{Tens}$ with respect to aspect ratio for all tested materials. The normalized moduli for all materials are within approximately 25% of unity, demonstrating that there is strong agreement between these two measurement techniques, with the exception of larger aspect ratio ($a/b \geq 6$, open symbols) samples for PET films.

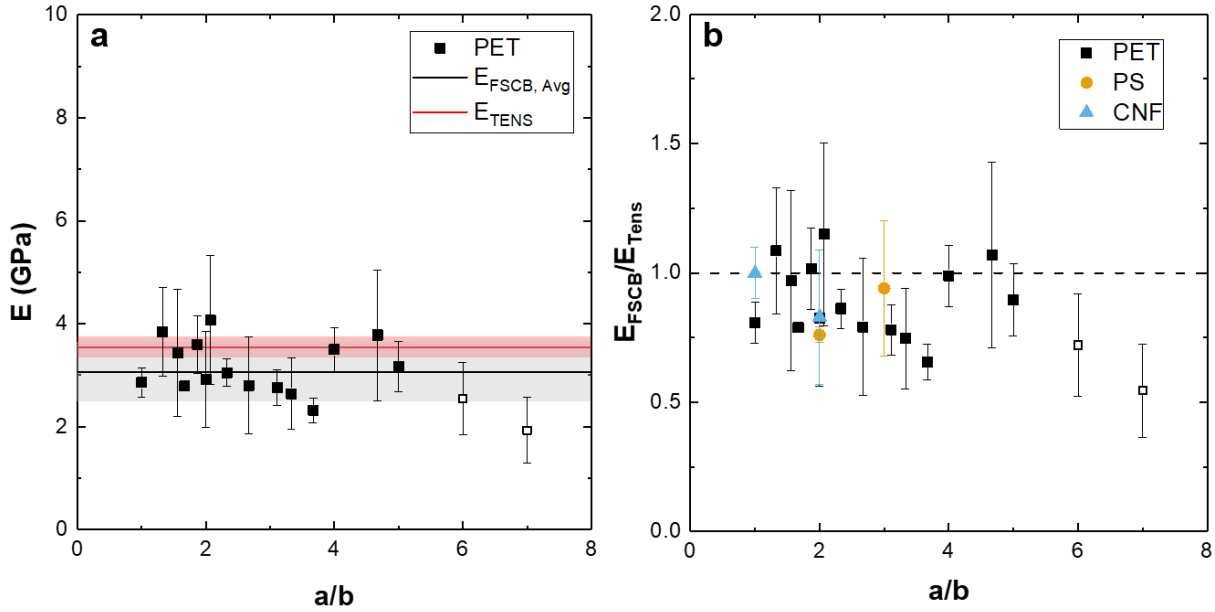


Figure 2-5. *a)* The average elastic modulus of each individual film geometry for PET. The black line represents the buckling modulus average and the gray shaded region is one standard deviation from the buckling average. The red line represents the tensile modulus average and the red shaded region is one standard deviation from the tensile average. *b)* The $E_{FSCB}:E_{Tens}$ ratio of each film geometry for all materials.

Initially, thin plate buckling mechanics relationships were considered as a likely mechanical deformation mode for the present system.^{13,39,44,45} However, column buckling mechanics relationships resulted in a more consistent modulus measurement even though film thicknesses were relatively thin ($0.001 < h/l < 0.02$ where l is either the sample length or width). It has been demonstrated previously that column buckling mechanics can be used for thin films.^{46,47} For a comparison of the E determined by the application of both relationships, Figure 2-6 shows the modulus for PET samples obtained from a host of experiments performed on a range of sample geometries. The black points represent column buckling mechanics $\left(E = \left(\frac{3}{\pi^2 h^3}\right) P_{cr} \left(\frac{a^2}{b}\right)\right)$, and

the blue points represent a plate buckling mechanics approach $\left(E = \left(\frac{3(1-\nu^2)}{\pi^2}\right) P_{cr} \left(\frac{b^2}{h^3}\right)\right)$ where ν is Poisson's ratio.

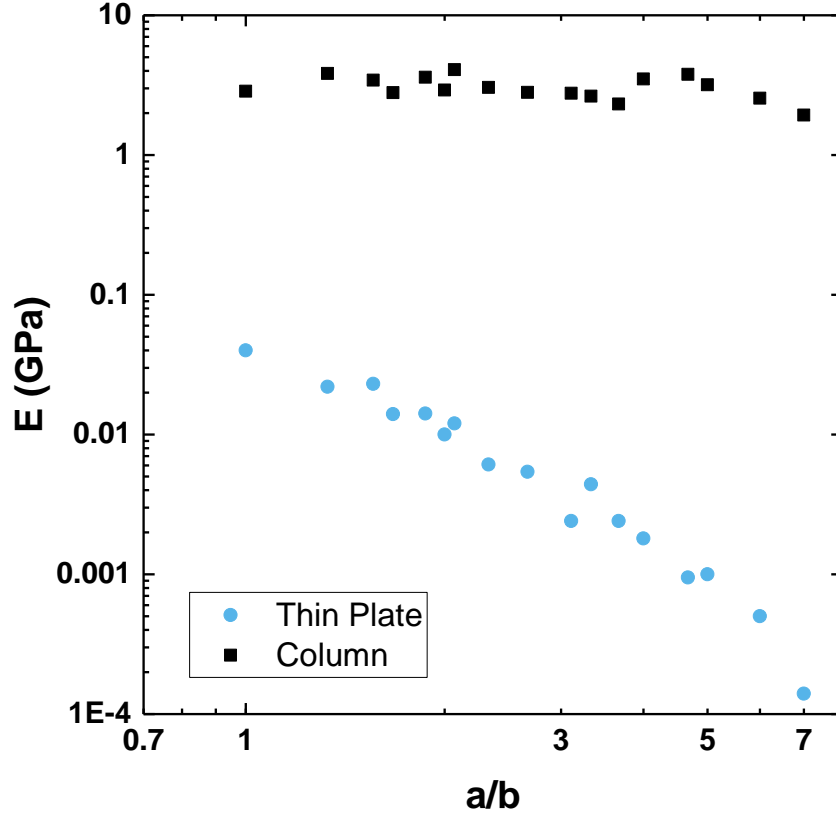


Figure 2-6. The comparison between thin plate and column buckling mechanics approaches for calculation of elastic modulus of the system. The same material was used for all experiments with (theoretically) the same modulus. The apparent change in modulus with aspect ratio of the sample by the thin plate buckling analysis (blue data points) indicates that one or more assumptions associated with this approach are not appropriate here.

Thin plate buckling has two differences when compared with column buckling: the inclusion of ν and the critical dimension (b^2 vs. a^2). The plate's resistance to anticlastic bending increases as the plate becomes wider. This causes a biaxial stress state within the material resulting in the introduction of ν ³⁹. Perhaps ν can be excluded in this case due the minute restraint to anticlastic bending caused by a smaller b compared to a . In addition, perhaps the suppression of transition of the critical dimension for determining P_{cr} , seen here, can be attributed to the size of b relative to a as well. Due to these hypothesized factors in our samples, a column buckling

mechanics approach was taken. However, it will be shown in Chapter 2 how changing geometry can warrant the use of thin plate column buckling mechanics or wide column buckling mechanics.

The FSCB modulus measurement technique is suitable for polymer films that are brittle, difficult to handle, and are more difficult to test in tension as demonstrated through testing PS and difficult to test in CNF. The purpose of selecting a tougher polymer film (PET) for the majority of this work was to allow for straightforward comparison of the modulus measured through orthogonal techniques. Comparing the tensile testing moduli with the FSCB moduli values show that the FSCB measurement approach is a valid technique. Future investigation will involve testing of layered brittle films, biologically-derived nanoparticle films such as neat cellulose nanocrystals, or films with a brittle, glassy coating on a softer substrate (where the two layers have equivalent thicknesses, prohibiting wrinkles from forming).

2.4 Conclusions

Column buckling mechanics were used to relate the critical buckling load to the elastic modulus. The critical buckling load for a range of film geometries were measured which allowed the elastic modulus of PS, PET and CNF films to be determined. A linear relationship between film width and the critical buckling load was observed while holding film length constant. An inverse quadratic relationship between film length and critical buckling load was observed while holding film width constant. The E_{FSCB} was found to be 3.06 ± 0.58 GPa and the E_{Tens} was 3.54 ± 0.20 GPa for PET. The agreement between all modulus values indicates the potential of the FSCB modulus measurement as an approach to determine the elastic modulus of brittle polymer films.

3. NANOCELLULOSE FILM MODULUS DETERMINATION VIA BUCKLING MECHANICS APPROACHES

Reprinted (adapted) with permission from (Rencheck, M. L, Weiss, A.J., El Awad Azrak S.M., Forti, E.S., Nuruddin, Md., Youngblood, J.P., and Davis, C.S. Nanocellulose Film Modulus Determination via Buckling Mechanics Approaches. *ACS Applied Polymer Materials*. **2**, 578–584 (2019). doi:10.1002/polb.24755.) copyright 2019, American Chemical Society.⁴⁸

3.1 Introduction

As previously mentioned in Chapter 2, Glassy polymer thin films are essential components in the manufacturing industry, specifically for food packaging and electronic substrates.^{22–25,49,50} Many films used in these applications are polyolefins derived from petroleum, which are becoming less sustainable for manufacturing due to resource limitations, pollution, and biodegradability issues.^{51–53} Therefore, a sustainable, biodegradable replacement for current polyolefin films is required to satisfy consumer demands for the future.

Cellulose nanomaterials have been proposed as potential alternatives to polyolefin films. Cellulose is a naturally occurring polymer found in the cell walls of abundant natural sources such as wood, bacteria, algae, and tunicates.^{54–56} Cellulose can be mechanically or chemically processed into cellulose nanocrystals (CNC) or cellulose nanofibers (CNF) which improve mechanical properties and can be cast into thin films from aqueous suspensions.^{28,54} CNC and CNF materials exhibit outstanding mechanical properties due to significant hydrogen bonding between the cellulose polymer chains that result in high theoretical specific strengths for single crystals comparable to Kevlar and axial moduli comparable with steel wire.^{54,57,58} Due to their desirable biodegradability, sustainability, and mechanical properties, CNCs are being considered for use in composites to toughen or strengthen the system and as coatings for barrier film applications.^{55,59}

In order for nanocellulose films to be implemented and scaled up for commodity production, reliable material property characterization methods must be developed. Even though these films are typically used as a single component in a composite system, understanding the mechanical behavior of each component is crucial to design the composite mechanical performance. A current challenge in mechanical property characterization of nanocellulose films lies in the reproducibility and accuracy of commonly used elastic modulus determination techniques. Depending on the processing conditions, nanocellulose films can be extremely brittle, resulting in low toughness and

strain to failure. This inherent brittleness leads to handling and measurement challenges with uniaxial tensile testing which creates challenges in the quality assurance of these materials for manufacturing.²⁷

Other thin film elastic modulus determination techniques, such as nanoindentation and surface wrinkling also have limitations for evaluating brittle polymeric films. A popular method for harder materials is nanoindentation, which uses the relationship between indentation and load to determine the elastic modulus.⁶⁰ However, films often fracture during indentation from the application of concentrated loads, resulting in an inaccurate modulus determination.^{31,61} Surface buckling (or wrinkling) has been used extensively to characterize the modulus of extremely thin glassy polymer films.^{34,35,62} In this method, a film is adhered to an elastic substrate and the bilayer sample is laterally compressed to induce wrinkling. The wrinkle wavelength, substrate modulus, and film thickness are used to determine the elastic modulus of the brittle film.^{34,63,64} Previous work by Cranston et al used surface wrinkling to characterize the modulus of multilayered CNF/polyethyleneimine films with thicknesses of 35-75nm.³⁵ While surface wrinkling has been utilized to characterize the modulus of nanocellulose composite films,^{65,66} this technique is more useful for films with submicron thicknesses. In addition, this technique requires strong adhesion between the film and substrate as well as delicate sample preparation procedures.^{34,67,68}

To overcome the measurement challenges associated with these existing methods, a free standing column buckling (FSCB) technique was developed to enable the measurement of the elastic modulus of glassy polymer films over a wide range of thicknesses which is discussed in more detail later.²⁰ FSCB is performed by applying a compressive axial load (P) to a glassy thin film until an out-of-plane buckling instability occurs. Given P_{cr} and the dimensions of a rectangular film, the elastic modulus (E) can be determined through Eq 3-1^{13,20,39,44}

$$E = \left(\frac{3}{\pi^2} \right) P_{cr} \left(\frac{a^2}{bh^3} \right) \quad (3-1)$$

where a is the length of the film between the clamps, b is the film width, and h is the film thickness. In our previous study, the results of the FSCB technique were compared with tensile testing and found to be in good agreement for the modulus determination of a tough, glassy film.²⁰

To further develop FSCB as a potential technique for determining E for brittle films, two P_{cr} determination methods are used here. The first method for determining P_{cr} was treated in detail previously.²⁰ In that method, referred to as the linear intercept (LI) method, P_{cr} was determined

using a two linear intercept approach to determine the critical load from the load-displacement curve collected during a FSCB experiment. The second method, referred to as the Southwell method, uses the vertical deflection ($v(x)$) of a column in relation to P prior to buckling to determine P_{cr} .^{14,41,45} Some significant differences between the Southwell method and the FSCB method are that the Southwell method measures P_{cr} prior to buckling and takes into account inherent initial deflections in the column which will be discussed in detail later. Tensile testing (where possible) was also utilized to determine E for several film types to provide further evidence of FSCB as an appropriate E characterization technique for nanocellulose and other brittle polymeric films.

To investigate ideal testing parameters for determining E , a variety of nanocellulose materials were selected with different E . Unpressed and pressed mechanically-fibrillated cellulose nanofibers (CNF) films, TEMPO-oxidized cellulose nanofiber (TOCNF) films, and CNC films were chosen for buckling and the results were analyzed to determine P_{cr} and calculate E . Three thicknesses were tested for each film type to further investigate the ideal sample geometries for FSCB to be utilized as an effective alternative metrology tool for characterizing E of nanocellulose films. Here, nanocellulose serves as a case study to demonstrate the applicability and robustness of this technique to characterize the E of a variety of stiff polymeric films with different E and/or sample geometries.

3.2 Materials and Methods

3.2.1 CNF Film Preparation

CNF was procured from the University of Maine (Orono, ME) (5-gallon, Batch #110, 3.1wt% CNF-water slurry) and was used as-received. The process of extracting and processing CNF is explained in detail by C.A. de Assis *et al.*⁶⁹ Films of CNF were prepared by diluting slurry (3.1wt%) to roughly 1wt% with deionized water. The mixture was shear mixed (SpeedMixerTM, FlackTek Inc.) at 2500 RPM for 2 min. Batches of approximately 15g, 25g, and 40g of the diluted mixture were cast into 10cm diameter circular petri dishes and left to dry in a controlled humidity chamber (50% relative humidity, RH) for 7 days until all the water has evaporated. Once dried, the films were removed from the petri dishes.

To flatten and alleviate potential residual stresses within the CNF films, several of the prepared films were pressed with a hydraulic heated laboratory press (Carver, 3690). Prior to pressing, the CNF films were submerged in deionized water for 10s to 30s, depending on thickness, for rehydration and softening. The wet films were placed between two polyethylene terephthalate films and hot pressed for 35min at a pressure of 0.4 MPa and a temperature of 126°C. After hot pressing, the heating elements were turned off and the films were cooled overnight in the press while the pressure was maintained.

3.2.2 TOCNF Film Preparation

A TOCNF suspension (1.1wt% in water with carboxylate content ranging from 0.2 to 2.0 mmol/g solids) was obtained from the University of Maine (USDA FPL, Madison, WI, Lot #2018-FLP-CNF-080). The TOCNF suspensions were diluted further with deionized water to 0.73wt%. Batches of approximately 30g, 45g, and 70g of diluted mixture were cast into a 10cm diameter circular petri dishes.⁵⁴ The suspensions were placed in a humidity chamber at 25%RH for about 7 to 15 days to allow the water to evaporate slowly (preventing residual stress build up due to differential drying). The dried films were carefully removed from the petri dishes.

3.2.3 CNC Film Preparation

CNCs were procured in aqueous suspensions from the University of Maine (batch no-2015 FPL-071 CNC, 12.2wt% in water containing 1 wt% sulfur with Na⁺ counterion on dry CNC). Based on previous TEM analysis, the average particle length and width were 99±27nm and 5.4±1.8nm, respectively.⁷⁰ Batches of 30g and 40g aqueous suspensions of 2 wt% CNC were cast into 10cm diameter petri dishes and left to dry at a relative humidity of 50%RH and room temperature for 7 days until fully dry. Once dried, the CNC films were carefully removed from the petri dishes.

3.2.4 Tensile Testing

Dogbone specimens with a gauge length of 12mm and a gauge width of 1.5mm were laser cut (Muse Hobby Laser, Full Spectrum) for all films (except CNC, which was too brittle for testing), using a sample geometry modified from ASTM D638-14.⁷¹ Tensile tests were performed

at a strain rate of $2.4 \times 10^{-4} \text{ s}^{-1}$ until failure (Psylotech, μTS). Films that failed prior to sufficient data collection were not used to determine E . A minimum of 6 samples were measured for each film at a single thickness.

3.2.5 FSCB Testing

All samples were laser cut (Muse Hobby Laser, Full Spectrum) into rectangles to have a testing area of 1 cm^2 (Figures 3-1a) and film thicknesses were characterized using a high accuracy digital micrometer (Digimatic Micrometer, Mitutoyo). All final film thicknesses had a standard deviation (SD) of less than $3 \mu\text{m}$ and are summarized in Table 1.

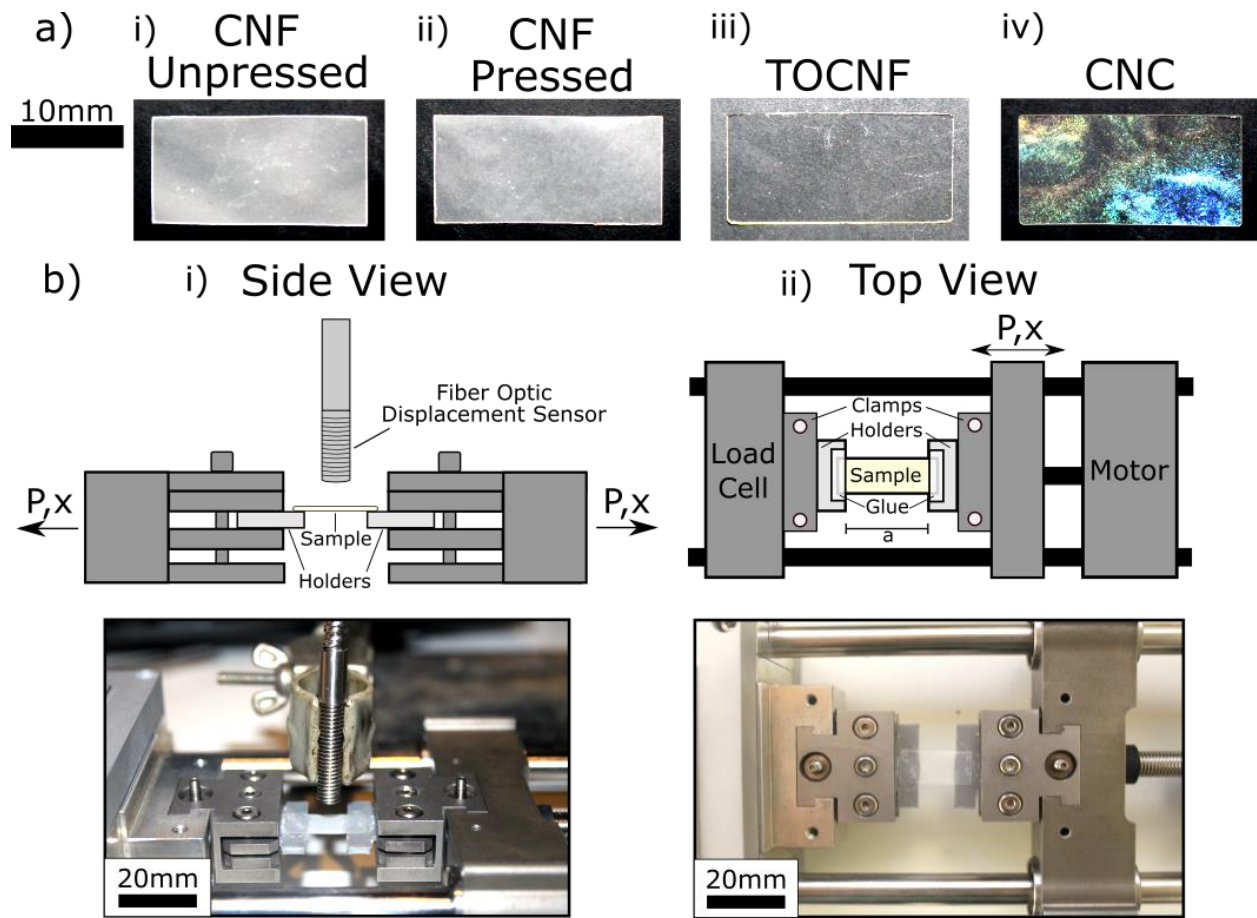


Figure 3-1. Images of rectangular laser cut *ai)* unpressed CNF, *aii)* pressed CNF, *aii)* TOCNF, and *aiv)* CNC films for buckling. *bi)* A top and *bii)* side view schematic and image of the experimental set-up for buckling.

Table 3-1. Nanocellulose Film Thicknesses

	CNF, Unpressed	CNF, Pressed	TOCNF	CNC
Thickness 1 (μm)	41	32	26	66
Thickness 2 (μm)	56	54	42	98
Thickness 3 (μm)	72	68	54	110

Sample holders were clamped into the load frame, and the films were subsequently fixed to the sample holders with cyanoacrylate glue (Loctite, Henkel Corp.) following the same procedure described in Rencheck et al.²⁰ For each FSCB test, a compressive load was applied at a lateral displacement rate of $1\mu\text{ms}^{-1}$, and the vertical deflection ($v(x)$) was collected at $x = (a - \Delta x)/2$ during each buckling experiment using a fiber optic displacement sensor (Philtex, muDMS-D100) at a sampling rate of 20Hz. To ensure that films were not pre-buckled prior to buckling, a small tensile load of two orders of magnitude smaller than the typical P_{cr} was applied to each film. A schematic and image of the experimental setup is shown in Figure 3-1b. A minimum of 6 samples were measured for each film type at each thickness, and a new film was mounted and tested for each trial.

3.3 Results and Discussion

Prior to buckling experimentation, the elastic limit of all the nanocellulose films needed to be determined since purely elastic deformation is a key assumption in FSCB mechanics. Once the elastic limits were determined through the use of an Euler curve, which will be discussed in detail later, the FSCB modulus experiments were performed on the nanocellulose films. The LI and Southwell methods were employed to determine P_{cr} and E , and compared with E determined via tensile testing. Larger film thicknesses were found to increase geometric film stiffness and E measurement reliability due to an increase in freestanding film stability.^{39,45} Overcoming the limitations caused by freestanding film stability at small h can be achieved by adjusting a and b and by utilizing freestanding wide column buckling mechanics instead of FSCB mechanics.

3.3.1 Establishing Buckling and Failure Criteria for Nanocellulose Films

Before FSCB testing, the yield (σ_y) or fracture stress (σ_f) of each nanocellulose film type must be determined so that the material will not plastically deform or fracture prior to the onset of

buckling. If failure modes other than buckling occur, an inaccurate or indeterminable P_{cr} will result due to the violation of a key assumption that the film deforms purely elastically during column buckling. A common method used to find the elastic buckling regime of materials is to construct an Euler curve.¹³ An Euler curve for the nanocellulose films was created (Figure 3-2) by plotting the predicted/estimated stress at which the film will buckle, referred to as the critical buckling stress (σ_{cr}), as a function of the slenderness ratio (s). Critical buckling stress values were estimated using Eq 3-2b and the experimentally determined tensile E values. For CNC films, the middle value of the range of previously reported E was used. s is given by the ratio of a and the radius of gyration (R) of the film. The radius of gyration can be defined as $R = \sqrt{I/A}$ where I is the moment of inertia and A is the cross-sectional area. For rectangular geometries, $I = h^3b/12$ and $A = bh$ which simplifies to $R = h/2\sqrt{3}$, allowing s to be obtained in terms of film geometry as shown in Eq 3-2a.

$$s = \frac{2\sqrt{3}a}{h} \quad (3-2a)$$

$$\sigma_{cr} = \frac{\pi^2 E}{s^2} \quad (3-2b)$$

As h increases or a decreases, the column becomes less slender and a greater stress is required to buckle the film.

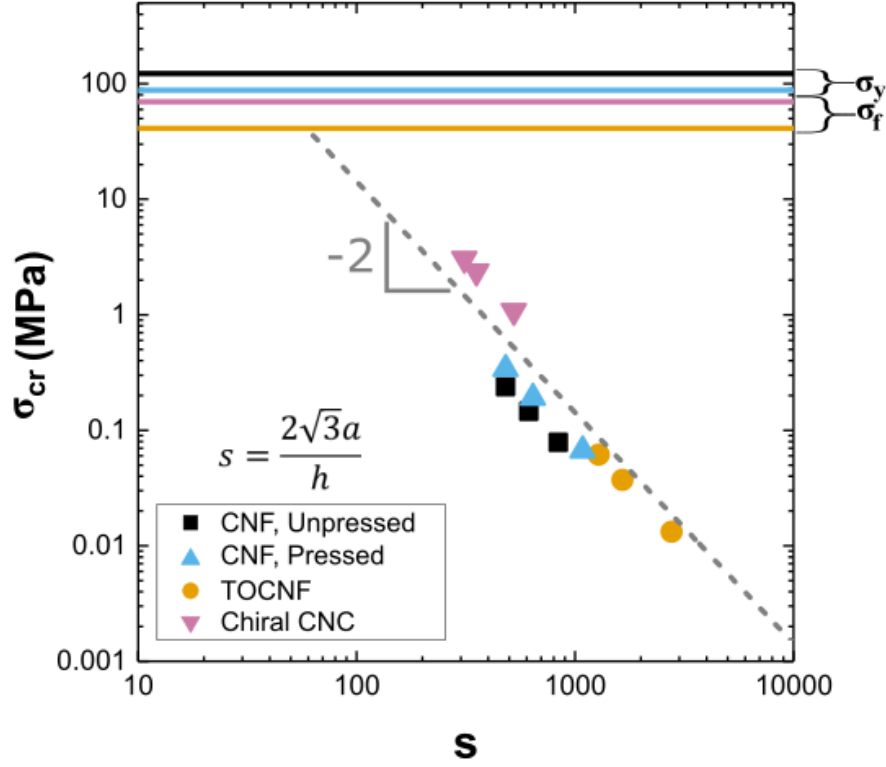


Figure 3-2. An Euler curve for the nanocellulose films. The horizontal lines represent the yield stress or fracture stress depending on the film type (corresponding to the colors in the legend). The dotted line has a slope of -2 and is a guide to the eye.

In the Euler curve in Figure 3-2, the dotted line has a slope of -2, highlighting the relationship of $\sigma_{cr} \sim s^{-2}$ (Eq 3-2b).^{13,72} The horizontal lines representing σ_y or σ_f for each film (determined through tensile testing or the middle value of a range of reference values in the case of CNC²⁷) indicate the upper limit for elastic buckling. Above these values, the σ_y or σ_f will exceed the expected σ_{cr} . The CNF films yield, while the more brittle TOCNF and CNC films fracture prior to yielding. The maximum predicted/estimated σ_{cr} for the CNC films was 3.04MPa, while literature reports σ_f of CNC films to be 70 ± 29 MPa.²⁷ The order of magnitude difference between the buckling and fracture stresses is a significant advantage of our approach since a main concern of tensile testing of brittle films is that, due to their high modulus and relatively low strain to failure, the fracture stress is often reached before sufficient data can be gathered for accurate modulus measurement. Assuming the selection of sample geometries has an appropriate slenderness ratio, FSCB can be used effectively to determine E when testing brittle films with low fracture stresses. To ensure that purely elastic deformation occurred, the slenderness ratios of all

FSCB samples were fixed between 300 and 3000 (depending on the film thickness) so that critical buckling stresses were reached prior to failure or yielding of each film..

3.3.2 *E* Determination by FSCB

After establishing that all the films will buckle in the elastic regime, FSCB experiments were conducted by monitoring in-plane load (P), in-plane displacement (Δx), and out-of-plane deflection ($v(x)$) with time. Both the LI and Southwell methods were utilized to determine P_{cr} . By using film geometries and the P_{cr} values determined by each method, E was determined through Eq 3-1.

The LI Method

The LI method determines P_{cr} by finding the critical point of the P - Δx curve for a buckling experiment using the x-intercept of two linear regressions taken at portions of the curve before and after buckling. Further detail on this methodology is given in Rencheck et al.²⁰ Representative P vs. Δx plots (for similar film thicknesses, $54 \mu\text{m} \leq h \leq 66 \mu\text{m}$) are shown in Figure 3-3a for each film type, along with a graphical explanation of this method.

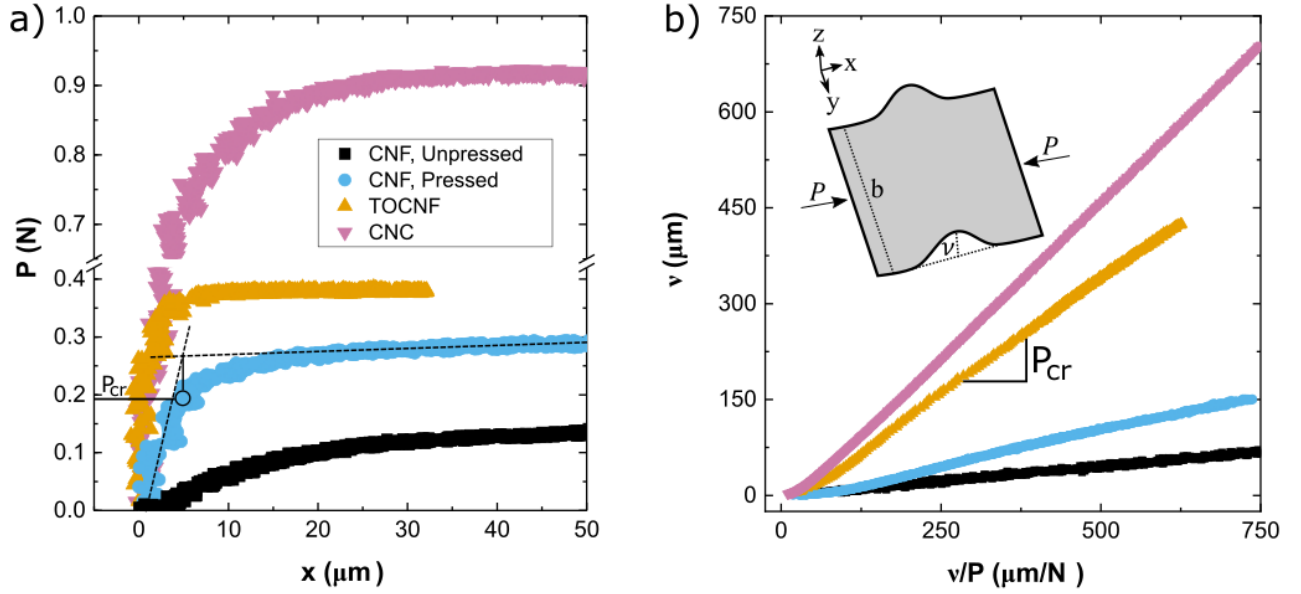


Figure 3-3. *a)* Representative force-displacement curves for P_{cr} determination using the LI methodology for all film types. Note the break in the y-axis. *b)* Representative $v(x)$ vs. $v(x)/P$ curves for P_{cr} determination using the Southwell methodology for all film types.

The Southwell Method

While the LI and Southwell methods both determine E through Eq 3-1, the Southwell method determines P_{cr} prior to the onset of the buckling instability and assumes that the column has an initial, non-zero deflection ($v_o(x)$). The Southwell method uses P and $v(x)$ to determine P_{cr} . In this method, the error normally associated with $v_o(x)$ is accounted for in quantifying P_{cr} because the P_{cr} determination relies on the rate of change between P and $v(x)$. The inherent $v_o(x)$ is accounted for in the Southwell method by incorporating an initial curvature expression into the 4th order equilibrium equation (Eq 3-3) of an imperfect freestanding column, which can be solved to find a relationship between P and $v(x)$.^{14,39,42}

$$\frac{d^4 v}{dx^4} + \frac{\alpha^2 d^2 v}{dx^2} = -\frac{\alpha^2 d^2 v_o}{dx^2} \quad (3-3)$$

where

$$\alpha^2 = \frac{P}{EI} \quad (3-4)$$

As P approaches P_{cr} ($P \sim 0.8P_{cr}$), the fundamental buckling mode dominates and allows $v_o(x)$ to be related to $v(x)$. Assuming that $v(x) = 0$ at both boundaries, the $v(x)$ and $v_o(x)$ functions can be written as a Fourier series, and substituted into Eq 3-3 to obtain Eq 3-5.

$$v(x) = P_{cr} \left(\frac{v(x)}{P} \right) - v_o(x) \quad (3-5)$$

Representative Southwell plots for all film types (for similar film thicknesses, $54 \mu\text{m} \leq h \leq 66 \mu\text{m}$) are shown in Figure 3-3b. The unpressed and pressed CNF have the shallowest slope, resulting in the lowest P_{cr} . As E increases, P_{cr} increases, reflected in the steeper slope of the CNC curve relative to the CNF films' responses. After P_{cr} was determined for each sample via the Southwell method, Eq 3-1 was used to determine E .

3.3.3 Comparing FSCB and Tensile Testing for E Determination

The determined P_{cr} and E values of the FSCB methods (and Southwell) were compared to the modulus determined through tensile testing (E_{TENS}) to identify any differences between buckling and conventional approaches. The P_{cr} comparison between the LI and the Southwell methods of the thickest films of each nanocellulose type is shown in Figure 3-4a. The Southwell method tended to measure a slightly higher P_{cr} than the LI method which was most likely caused by the LI method assumption of $v_o(x) = 0$. Another cause of the difference between the two methods could come approximating at $v(x)$ as a 1 dimensional function which is valid when only assuming small film deflections away from the x-axis. However, in the case of large deflections, $v(x)$ can be generalized as a parametric function along the film's arclength (l) ($v(l) = v(x(l), y(l))$).³⁹

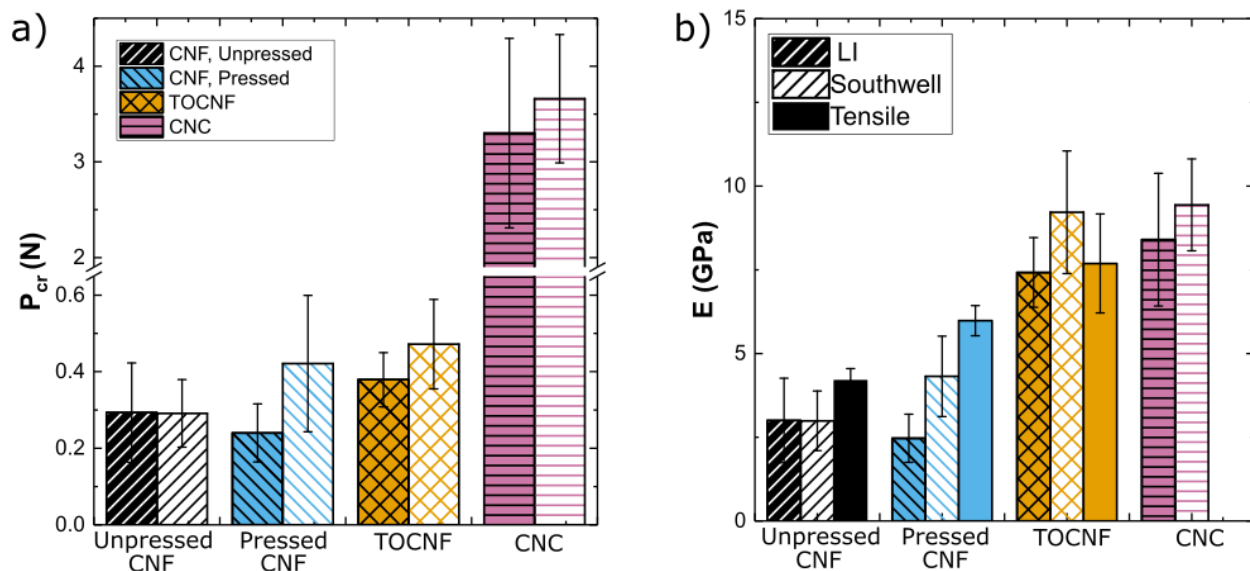


Figure 3-4. a) P_{cr} for the LI and Southwell methods at the largest thickness for each film type. Note the break and change in scale in the y-axis. b) E for the LI method, the Southwell method, and tensile testing approaches at the largest thickness for each film type. The filled rectangle with the dotted outline denotes the range of reported literature values of the CNC tensile modulus.^{27,73} The error bars represent one standard deviation of the average in both plots.

When comparing the modulus determined through the LI method (E_{LI}) and the modulus determined through the Southwell method (E_{South}) to E_{TENS} for each material, the LI and Southwell methods resulted in a lower E for the CNF films and a similar E for the TOCNF films. A comparison of E_{LI} and E_{South} with E_{TENS} for each material is shown in Figure 3-4b. The error shown in Figure 3-4 can be attributed to instrumental error in the collection of out-of-plane deflection (displacement sensor) or load data (tensile frame load cell), experimental error during sample mounting from manual sample alignment and fixation procedures, and/or error from material heterogeneities and defects within samples. A more detailed discussion of error in buckling experiments is provided in previous works.^{20,39} The CNF films exhibited the lowest E while the CNC films were stiffest. This is expected since the CNC films have the highest density of hydrogen bonding among the tested films and very little amorphous cellulose chains.⁵⁴ The E_{TENS} for the CNC films was unmeasurable due to their brittle nature. The E_{LI} and E_{South} values measured here are reasonable and within the range of reported literature values.^{27,73} These literature values were determined by tensile testing and required complicated sample mounting procedures (i.e. utilizing a steel tab assembly to support the CNC film) or calculating the modulus

of a CNC layer within a laminated composite system. The range of CNC moduli values reported in literature is likely caused by differences in sample preparation, inherent batch to batch variation in the cellulose, and/or environmental conditions during testing. Ultimately, Utilizing the LI or Southwell method was able to determine E for the stiffer nanocellulose films.

3.3.4 The Effect of Stiffness on Measurement Precision Through FSCB

In mechanical buckling experiments, a column must satisfy a strength and stiffness criteria to ensure structural stability during testing. The strength criterion was satisfied through the application of the Euler curve that ensured the tested films buckled before plastic deformation or fracture. The stiffness criterion ensures that the film is stiff enough so that it will not experience any undesirable deflection behavior during loading.³⁹ Therefore, the geometric film stiffness should be considered to understand its effect on determining E .

The geometric stiffness of a column, K , can be defined as the amount of force required to cause displacement over a specific distance and can be related to E and sample geometry.^{74,75}

$$K = E \left(\frac{bh}{a} \right) \quad (3-6)$$

By substituting Eq 3-6 into Eq 3-1 and rearranging, the geometric stiffness of a freestanding film can be related to P_{cr} .

$$P_{cr} = K \left(\frac{\pi^2 h^2}{3a} \right) \quad (3-7)$$

To understand how K effects measuring P_{cr} , sample dimensions can be adjusted. The effects of aspect ratio (a/b) on P_{cr} were previously investigated and showed that films with an aspect ratio approaching unity (from infinity) are stiffer. The increased geometric film stiffness led to an overall increase in the reliability of E measurements.²⁰ Here in Chapter 2, film thicknesses were varied to further investigate the role of sample geometry effects on E reliability.

Three thicknesses were measured for each nanocellulose film type with FSCB, using both the LI and Southwell methods to determine E . The P_{cr} values as a function of h for each film type are shown in Figure 3-5a with both a and b held fixed at 1cm. All P_{cr} values increase with h as expected. Based on the predicted/estimated σ_{cr} values utilized to create the Euler curve in Figure 3-2, FSCB testing occurred within the elastic buckling regime for all experiments conducted here. A modified Euler curve is shown in Figure 3-5b with measured σ_{cr} values. Lines with slope of one

represent perfect agreement with Eq 3-2b. The buckling response of the TOCNF and CNC films show good agreement with a slope of one while the mCNF, especially the samples with the largest s , deviate significantly from the expected relationship. Given that the mCNF films buckled at stress well below the yield stress, plastic deformation does not explain the deviation from the expected slope of one in Figure 3-5b. Since all the films' strength criterion was satisfied, an examination of the films' stiffness criteria should be considered as potential reasoning for the deviation seen in Figure 3-5b.

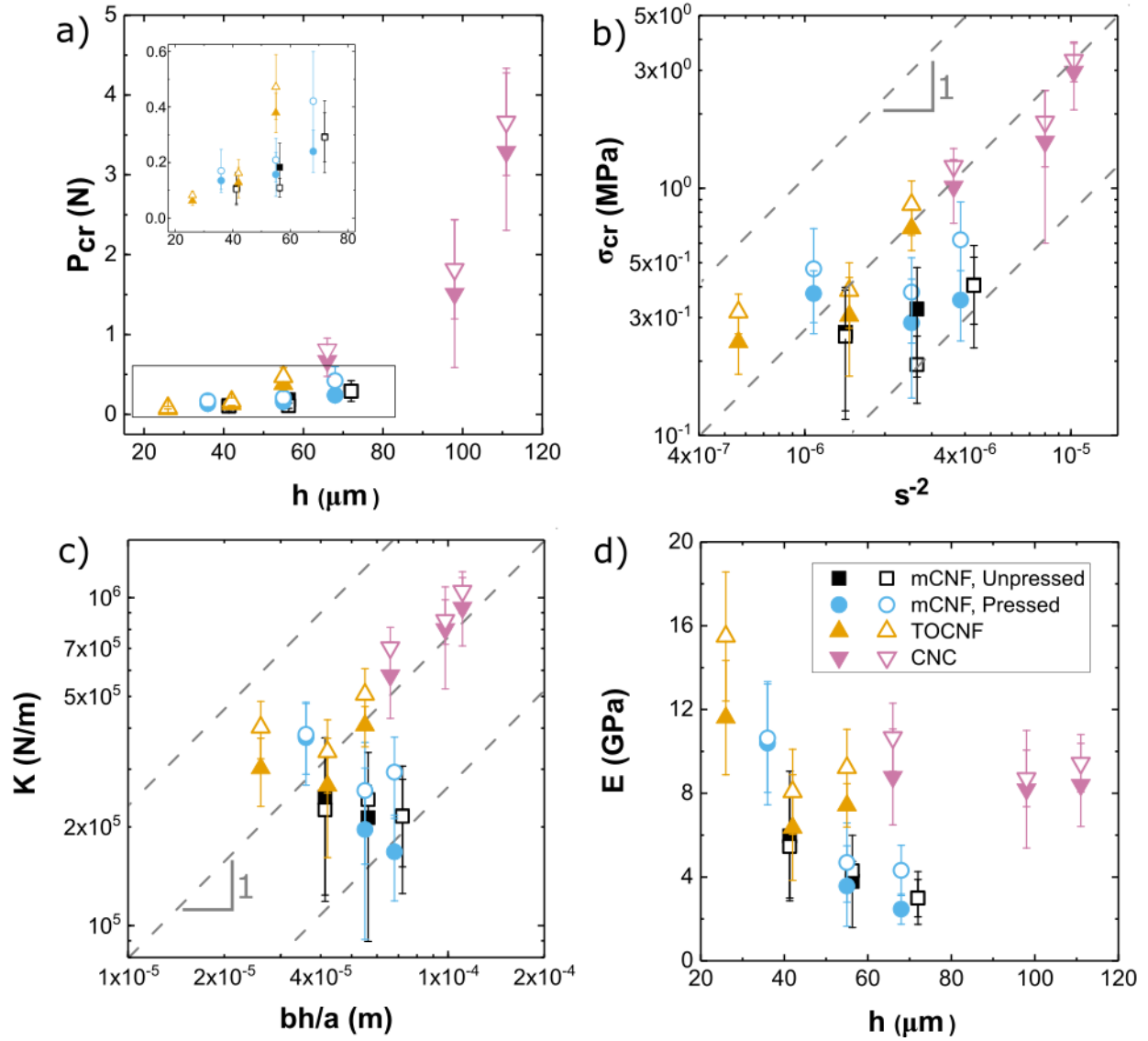


Figure 3-5. *a)* The effect of thickness on P_{cr} for both the LI (filled) and Southwell (open) methods. *b)* A modified Euler curve. *c)* K dependence on sample geometry. *d)* The effect of thickness on E for both the LI (filled) and Southwell (open) methods. The dashed lines in *b)* and *c)* have a slope of one and are a guide to the eye. The error bars represent one standard deviation of the average.

When K is plotted as a function of bh/a (Figure 3-5c), a slope of one between data for each material indicates that the expected linear relationship between K , sample geometry, and E given in Eq 3-6 holds. When the data deviates from this trend, it is likely that the limitation of the material's stiffness criteria has been reached. The CNC films, which were the stiffest (and in this case the most brittle) films, exhibited good agreement with a slope of one, confirming that the FSCB measurement of E is a reliable approach. However, based on the deviation of the thinnest

TOCNF films and most of the mCNF samples from a linear trend, the stiffness criteria for these samples may not be satisfied. For the unpressed mCNF samples, no relationship between K and sample geometry is observed regardless of h , which is likely caused by the initial waviness of these samples resulting from residual stresses induced by the sample preparation process. The P_{cr} values were used to determine E , through Eq 3-1 for either FSCB method (Figure 3-5d). As h increased, the LI and Southwell methods were able to more reliably determine E with the exception of the thinnest TOCNF sample and the mCNF films. As a result, E of the two thickest TOCNF and all the CNC films, which were also the most brittle, were able to be characterized and are even further confirmed when compared to the tensile tested values in Figure 3-4b.

K plays an important role in determining the stability of a freestanding film. The freestanding stability of a film can be defined as the load bearing ability of a sample with a given geometry and loading conditions.^{39,76} As h decreases, K becomes smaller which results in a lower freestanding film stability. At low freestanding film stabilities, the film becomes more susceptible to mechanical vibrations which can introduce error into P_{cr} measurements causing a less reliable E determination.⁴⁵ High film compliance is a significant reason why thinner films are typically supported when determining E in conventional testing methods. Therefore, it is important to select a h that gives the film a K value that satisfies the stiffness criterion which allows for a reliable E determination through FSCB.

Further, samples with higher geometrics stiffnesses (achieved either through sample geometry selection or E) are more appropriate for the FSCB buckling technique presented here. Eq. 3-6 shows that K is inversely proportional to the sample aspect ratio. However, for FSCB, the aspect ratio must be greater than or equal to unity to avoid the introduction of a biaxial stress state. FSCB mechanics should not be applied in a biaxial stress state because the assumption of a uniaxial stress state is no longer valid. When a biaxial stress state is caused by a smaller a and/or larger b the governing buckling mechanics relationship transitions from FSCB to freestanding wide column buckling.³⁹ When using a buckling mechanics approach to determine E for films constrained to smaller thicknesses, an aspect ratio less than 1 along with wide column buckling mechanics should be utilized to ensure reliability in measuring E .

Although this work operates in a mesoscale film thickness range ($25\mu m \leq h \leq 111\mu m$), this approach could be scaled to measure the moduli of films with micro and nanoscale thicknesses. Until continuum mechanics assumptions fail as the film thicknesses approach the

micro/nanostructure length scales of the material, the FSCB modulus measurement will be an effective measurement tool. Sample geometries can be adjusted according to Eq. 3-6 to satisfy the stiffness criterion, and with the application of the appropriate buckling mechanics relationships (FSCB, plate buckling, or wide column buckling), E can be quantified over a wide range of film thicknesses. However, the same stiffness criterion is not applicable for all materials with identical geometries and should be calculated for each material class because K is related to E . Ensuring that the stiffness criterion is satisfied when using FSCB allows this technique to measure E of a large variety of materials at a range of length scales.

3.4 Conclusion

Two different methods were utilized to determine the P_{cr} of unpressed CNF, pressed CNF, TOCNF, and CNC films using buckling mechanics to ultimately determine E . First, the LI method uses the critical point of a load-displacement curve of each buckling experiment to determine P_{cr} . Second, the Southwell method utilizes out-of-plane deflection, $v(x)$, in relation with P to determine P_{cr} . An Euler curve was used to verify that all buckling occurred in the elastic deformation regime. Then, films with varied thicknesses of each nanocellulose type were tested and analyzed using both methodologies to determine P_{cr} and E . The LI and Southwell methods resulted in similar E when compared to the largest thickness of each material. When E_{LI} and E_{South} were compared to E_{TENS} , the most effective E determination techniques were able to be identified for each nanocellulose film type. FSCB is most effective for the stiffest materials (TOCNF and CNC).

Film thickness was an important factor to consider when determining the elastic modulus due to geometric film stiffness effects. As film thickness increased, the geometric stiffness and freestanding film stability increased, which led to a more reliable modulus determination. In order to satisfy the stiffness criterion required for reliable buckling of very thin films, the aspect ratio can be modified to be less than one in conjunction with implementing freestanding wide column buckling mechanics instead of FSCB mechanics. While film thickness is an important factor to consider before testing, film length and width can be adjusted to allow for a reliable determination of elastic modulus. Using buckling mechanics as a modulus measurement technique has the ability to determine the modulus of brittle, stiff films as demonstrated here for various nanocellulose materials. By modifying sample geometries and applying the appropriate buckling mechanics

analysis, a variety of brittle polymeric materials can be characterized over a wide range of length scales.

4. THE TAPE DRAPE TEST – A PRACTICAL AND NONDESTRUCTIVE WAY TO ASSESS ELASTIC MODULI OF PAVEMENT MARKING TAPES IN THE FIELD

Reprinted (adapted) with permission from (Rencheck, M. L, Grennan, H.P., Gohl, J.A., Erk, K.A., and Davis, C.S. The Tape Drape Test – A Practical and Nondestructive Way to Assess Elastic Modulus of Pavement Marking Tapes in the Field. Transportation Research Record.) copyright 2020, SAGE Publishing.⁴⁸

4.1 Introduction

Temporary pavement marking (TPM) tape adhesion with roadway surfaces is critical for tape performance. The two main TPM performance issues both stem from the adhesive strength. Weak adhesion results in premature detachment and excessive adhesion requires extensive removal processes that often leave ghost markings, both of which can cause dangerous confusion in road construction zones. Tape adhesion is directly related to the elastic modulus (E) of TPM tapes. Thus, accurate characterization of E prior to tape installation is essential to fully understand and predict the adhesion performance and ultimately the durability of TPMs. An accurate assessment of E in the field is essential for predicting performance as E of TPM tape changes with temperature. Traditional E characterization techniques, such as tensile and three-point bend testing, may not be able to accurately measure E due to the complex structure of the tapes and are difficult to conduct at temperatures above or below room temperature without special equipment. Here, a new methodology that can be utilized which accounts for the complex tape structure and can be conducted in the field with minimal equipment.

TPMs are commonly deployed in construction work zones and temporary roadway areas. Highly visible, durable, and easily removable TPMs are necessary to provide drivers with a clear travel path through work zones without damaging the roadway surfaces.^{77,78} In many areas, TPMs are also required to temporarily cover and/or replace existing permanent pavement markings to avoid potential lane confusion for drivers.^{79–81} Durability and ease of installation and removal are high priorities for TPMs because reapplication and intensive tape removal processes can significantly increase both material and labor costs, delay roadway reopening, and damage roadway surfaces from grinding or milling.^{82–86}

The components and structure of TPM tapes impact their overall performance on roadway surfaces. Generally, TPM tapes are comprised of synthetic polymer and pigment as well as glass beads added for increased retroreflectivity.⁸⁷ The top layer consists of glass beads embedded in polymer paint followed by a flexible rubber filled with additional glass beads, a reinforcing fabric, and a polymer-based pressure sensitive adhesive (PSA) on the bottom that allows the tape to adhere to surfaces. Some TPM tapes have raised surface features that improve friction and retroreflectivity properties of the tape (Figure 4-1c) while others do not (Figure 4-1a-b). Other factors such as the application procedure, environmental conditions, and roadway surface conditions have a significant impact on tape performance as well but are not investigated in the scope of this work.^{88–}

91

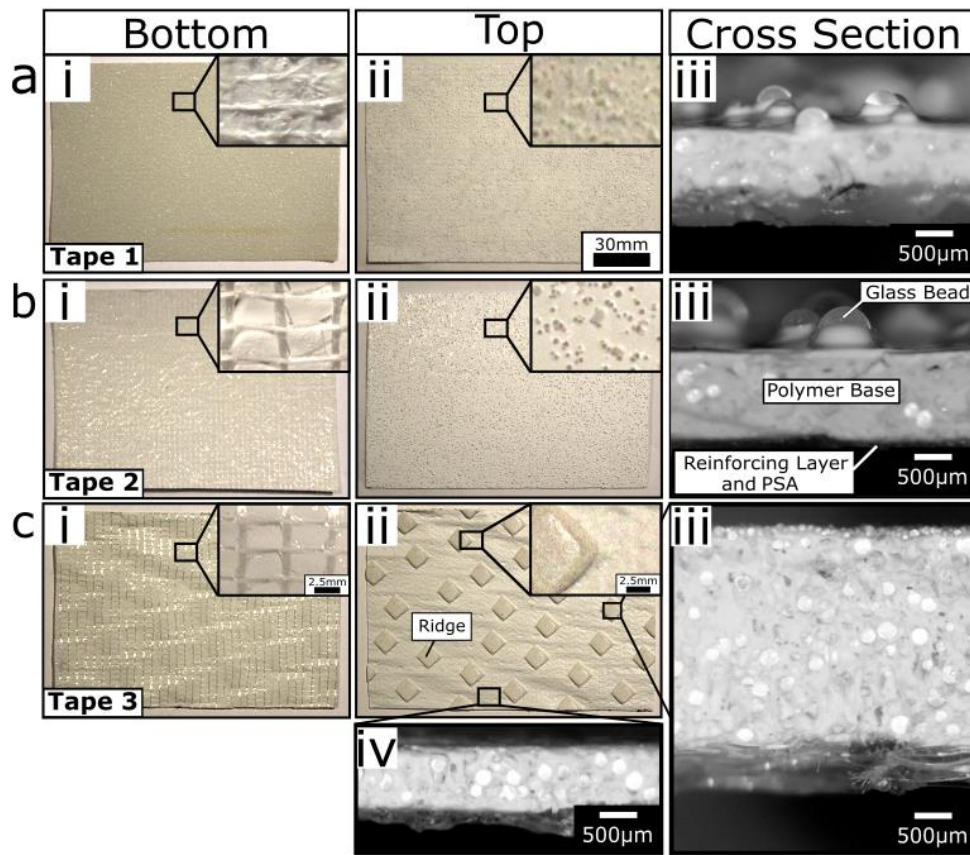


Figure 4-1. Representative images of TPM tapes. A macroscopic image of the *ai*) back, *a ii*) front, and *a iii*) cross-sectional image of Tape 1. A macroscopic image of the *bi*) back, *b ii*) front, and *b iii*) cross-sectional image of Tape 2 with labels of structural features. A macroscopic image of the *ci*) back, *c ii*) front, and cross-sectional image *c iii*) through a raised ridge and *c iv*) away from a ridge.

To remove a PSA from a surface, a critical force required for debonding (F_c) must be achieved. F_c can be related to the ratio of the surface area (A_s) to compliance (C) by Eq. 4-1,⁹²

$$F_c \sim \sqrt{G_c} \sqrt{\frac{A_s}{C}} \quad (4-1)$$

where G_c is the critical strain energy release rate, a property of the interfacial energy between the TPM tape and substrate. C can be defined by Eq. 4-2 and is dependent on the geometry and effective modulus of the tape (E).^{93,94}

$$C = \frac{1}{E} \left(\frac{t}{ba} \right) \quad (4-2)$$

Here, t is the tape thickness, a is the tape length, and b is the tape width. Eq. 4-2 can be substituted into Eq. 4-1 to show the dependence of F_c on G_c and E (Eq. 4-3).

$$F_c \sim \sqrt{G_c} \sqrt{(E) \left(\frac{baA_s}{t} \right)} \quad (4-3)$$

Eqs 4-1 and 4-2 show that the main material properties that govern TPM adhesion performance are G_c and E . G_c is determined by the surface energies of the PSA and the substrate. Since most TPM tape PSA chemistries are similar, G_c values are effectively constant amongst all TPM tapes⁹² when contacting the same substrate (e.g., asphalt pavement). If G_c is considered to be constant, then E of the tape becomes the most significant material property that impacts the critical adhesion force of TPM tapes on roadway surfaces (Eq. 4-4).

$$F_c \sim \sqrt{E} \quad (4-4)$$

TPM tape adhesion must be durable enough to remain affixed to the roadway over a range of traffic loads and environmental conditions yet must be easily removed once construction is complete.^{87,91} PSAs with lower E tend to have a stronger adhesive bond with surfaces, but from a TPM tape perspective can cause removal difficulties. Therefore, E must be low enough to ensure sufficient adhesion with pavement surfaces but high enough to allow for easy removal and durability throughout the project lifetime.⁹⁵ Given the impact of E on TPM tape performance, it is critical to accurately measure this value for various products.

Measuring E of TPM tapes in the field is important because changes in temperature can significantly affect E .⁹⁵ Pavement and air temperatures can drastically change day to day or even hour to hour depending on the location and season. Since temperature significantly affects E and

subsequently adhesion on pavements, it is essential to test TPM tapes in an environment similar to the application environment for quality assurance.⁹⁶ The change in E due to temperature are attributed to the glass transition temperature (T_g) which is the temperature that polymers and bulk plastic materials transition between a brittle glassy state to a rubbery, more ductile state.¹⁵ Interestingly, T_g of most commercial TPM tapes lies within the range of potential application temperatures at the work-zone depending on the geographical location and time of year.^{97,98} TPM tapes that are applied at temperatures below their T_g may not make full contact with the pavement surface during application due to the temperature-induced increase in E or be more difficult to remove due to brittle fracture, preventing detachment as one piece. Alternatively, when temperatures exceed T_g , the tapes can transition to a more ductile regime leading to an increase in F_c that prevents effective tape removal. The ability to characterize E in the field enables temperature effects to be accounted for during application.

Traditional E measurement techniques are unable to be employed in the field to accurately assess E due to changes in temperature. Techniques that are traditionally employed to characterize E are tensile testing and three-point bend testing. Both techniques require large stationary, expensive equipment that does not typically integrate well with testing above or below room temperatures. Additionally, these methods are destructive examination techniques requiring tapes to be cut before testing, and plastic deformation of the tapes caused by testing does not allow tapes to be applied afterward. While tensile and three-point bend testing can determine E for TPM tapes, the composite structure of the tape and textured surface of some products lead to high variability in these measurements. Further, specimen preparation, specifically how the specimen is sectioned, such as size and orientation relative to the machine direction, can play a significant role on the measured value of E .

In this study, three commercial brands of TPM tape approved by the Indiana Department of Transportation were tested to compare traditional E characterization techniques with one other potential technique that may be implemented in the field. Tensile testing following ASTM D638-14 and three-point bend testing following ASTM D790-17 were the selected commonly utilized techniques. The Peirce cantilever test herein referred to as the Tape Drape Test follows ASTM D1388-18. This test, developed by F.T. Peirce in 1930, was selected as the potential field test because it requires minimal sample preparation and no heavy or stationary equipment.⁸ By comparing the measured E values from the tensile and three-point bend testing with the results

from Tape Drape Testing, a proper E determination method can be verified for TPM tapes and other material systems similar to TPM tapes. Accurately assessing E of TPM tapes will aid in the selection process of which TPM tapes to apply under a given set of environmental conditions.

4.2 Materials and Methods

All TPM tapes used in this study are commercially available and were chosen from an Indiana Department of Transportation list of approved TPM materials. Tensile testing and three-point bend testing have typically been used to characterize E of polymeric materials. While these methods are appropriate for polymeric materials with a uniform cross section, TPM tapes have a complex structure that complicates specimen preparation and data interpretation. The new methodology proposed here to characterize E of TPM tapes is the Peirce cantilever test, referred to here as the “Tape Drape Test”. The Tape Drape Test can consistently measure the effective E of TPM tapes as a whole and can be conducted with minimal equipment in the field.

4.2.1 Tensile Testing E Determination

Tensile testing was conducted based on ASTM D638-14.⁹⁹ The experimental set-up for tensile testing is shown in Figure 4-2a. The tapes were supplied by the manufacturers and used as received. The thickness (t) of Tape 1 (1.19 mm), Tape 2 (1.19 mm), Tape 3 without ridges (0.91 mm), and Tape 3 with ridges (2.37 mm) were measured. The standard error across all thickness measurements was 0.1 mm. The TPM tapes were cut into dogbone specimens with a gauge width (w) of 3.80 ± 0.3 mm and gauge length (l_o) of 15.25 ± 0.5 mm. Tensile tests were performed at a rate of $0.5 \text{ mm} \cdot \text{s}^{-1}$ (TA.XTplusC Texture Analyser, Stable Micro Systems). A minimum of three trials were performed for each TPM tape using a different specimen each trial.

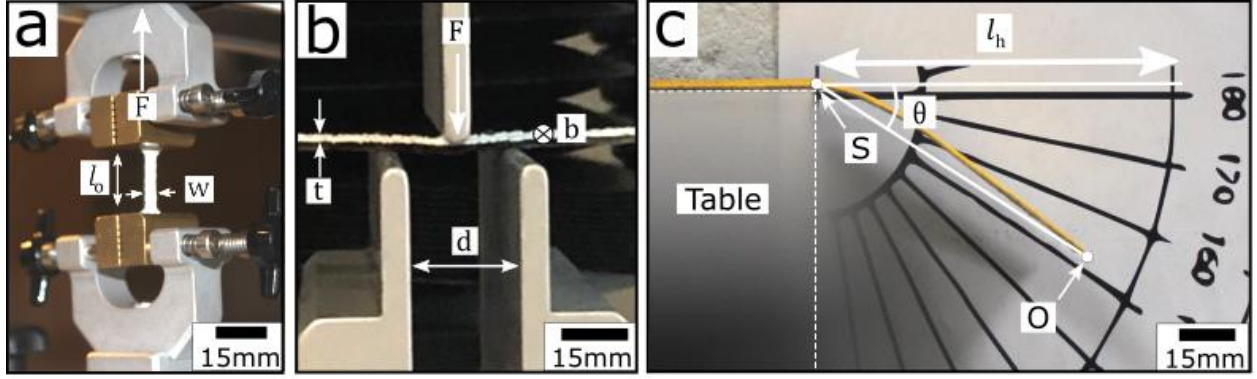


Figure 4-2. Experimental set-ups of *a)* tensile testing, *b)* three-point bend testing, and *c)* Tape Drape Testing.

Force (F) and displacement (Δl) values from each tensile testing trial were captured to determine the stress (σ) and strain (ε) behavior of each tape. σ was calculated from Eq. 4-5 where A_x is the cross-sectional area ($A_x = wt$) and ε was calculated from Eq. 4-6 where l_o is the initial length of the tested sample.

$$\sigma = \frac{F}{A_x} \quad (4-5)$$

$$\varepsilon = \frac{\Delta l}{l_o} \quad (4-6)$$

At small strains, each tape exhibited a linear elastic behavior governed by Hooke's law (Eq. 4-7). E was determined from the initial slope of each tensile curve until a strain of 0.02 to ensure the tapes were in the elastic regime.

$$\sigma = E\varepsilon \quad (4-7)$$

Using Hooke's law, E of each tape can be determined from the slope of the elastic region of each σ - ε curve.

4.2.2 Three-Point Bend E Determination

Three-point bend testing was conducted based on ASTM D790-17.¹⁰⁰ The experimental set-up for the three-point bend testing is shown in Figure 4-2b. The TPM tapes were cut into rectangular specimens for three bend testing with widths (b) of 12.7 ± 0.1 mm and lengths of 65.0 ± 0.1 mm using a span (d) of 25 mm. Three-point bend tests were performed at a rate of

0.01 mm·s⁻¹. A minimum of three trials were performed for each TPM tape using a different specimen each trial.

Three-point bend testing was employed to determine the flexural modulus (E_{Flex}) of the TPM tapes. At low strains below the proportionality limit, E_{Flex} can be considered to be equivalent to E . Therefore, by determining E_{Flex} via three-point bend testing, E is also determined. During each trial, the crosshead moved in the y-direction to cause a lateral bending deflection (δ) in a rectangular tape specimen spanning the bottom two points. δ was taken as equivalent to the crosshead displacement.

Similar to tensile testing, F and δ values were collected and analyzed to determine E_{Flex} . A similar analysis technique for determining E_{Tens} was used to determine E_{Flex} , where the bending stress (σ_{bend}) and bending strain (ε_{bend}) are plotted instead of σ and ε . σ_{bend} was calculated through Eq. 4-8, and ε_{bend} was calculated through Eq. 4-9.

$$\sigma_{bend} = \frac{3Fd}{2bt^2} \quad (4-8)$$

$$\varepsilon_{bend} = \frac{6\delta t}{d^2} \quad (4-9)$$

E_{Flex} was determined from the slope of the elastic region of each $\sigma_{bend} - \varepsilon_{bend}$ curve.

4.2.3 Tape Drape E Determination

The Tape Drape Test was performed based on ASTM D1388-18.¹⁰¹ The experimental set-up for the Tape Drape Test is shown in Figure 4-2c. The TPM tapes were trimmed from the as-received roll to have a length of 160 mm. The edges of each tape were unmodified so that width (b) was set by the manufacturer. For Tape 1, Tape 2, and Tape 3, b was 60 mm, 70 mm, and 100 mm, respectively. A digital camera (EOS Rebel TS5 DSLR, Canon) was employed for imaging. Before each trial, the camera was leveled with the 0° mark on the protractor. The TPM tape was tested with the PSA side facing down. Before recording the drape angle (θ), the specimens were allowed to equilibrate for 60 s to improve the consistency of the measurement. A minimum of three θ values were taken for 3 separate specimens for each tape.

Determining θ for the Tape Drape Test

Measuring θ is a straightforward process that is shown in Figure 4-3. Here, ImageJ was used for the analysis of θ for the Tape Drape Test, but an image processing software should be capable. The image file was uploaded to ImageJ, and the angle tool in ImageJ was selected as the method to measure θ (Figure 4-3a). The line segment from the draped end of the tape (Point “O”) to the point where the tape leaves the table (Point “S”) was drawn (Figure 4-3b) for each trial. It is important to note the y-coordinate of Point “S” as this will help define the horizontal line needed to determine θ . Using the y-coordinate of Point “S”, a horizontal line is drawn to an arbitrary length which defines the reference line from which θ was measured (Figure 4-3c). The measurement function was used to determine θ which was 27.9° for this trial.

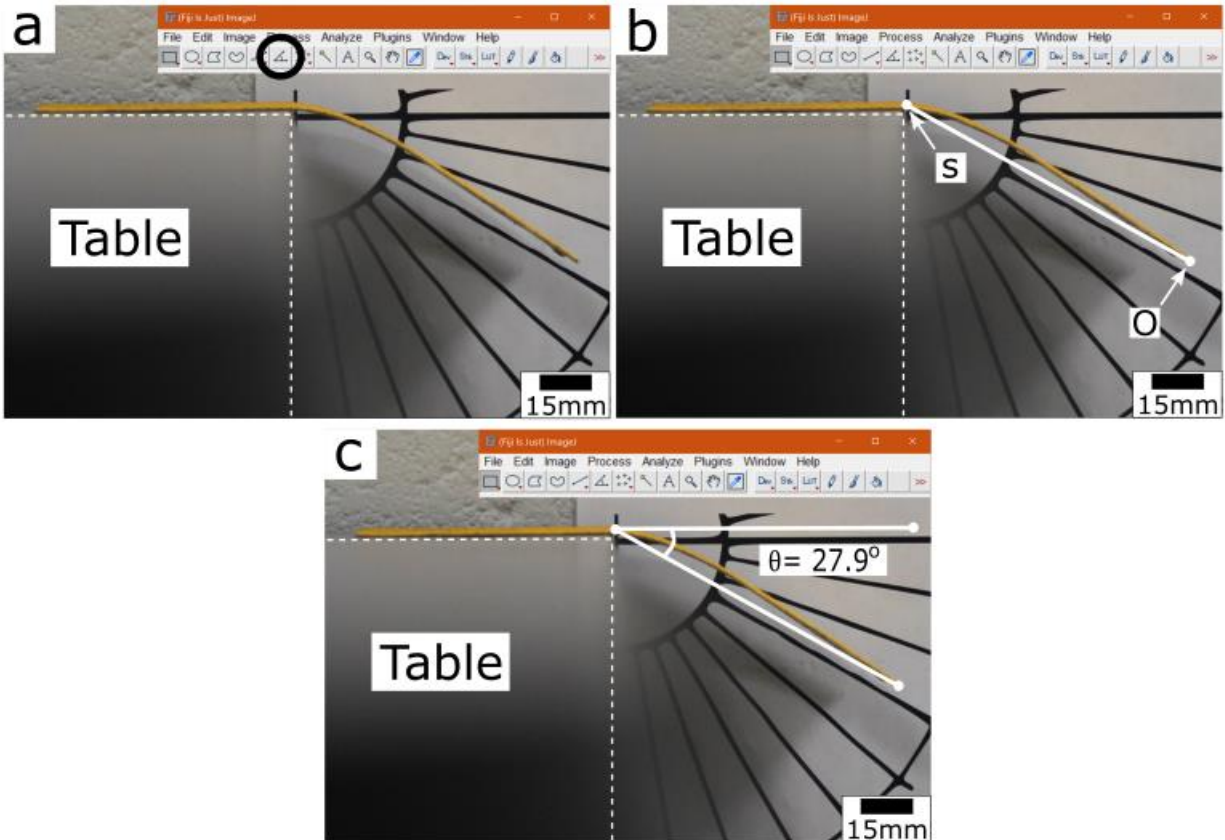


Figure 4-3. An example of the ImageJ analysis used to determine θ for the Tape Drape Test. *a)* The angle tool was selected from the toolbar at which point *b)* a line was drawn from the edge of the table (point S) to the specifying the endpoint of the tape to the horizontal (point O). *c)* A second horizontal line was drawing starting from the edge of the table (point S) which established the horizontal to calculate θ which equaled 27.9° in this example.

Determining E from θ for the Tape Drape Test

In the Tape Drape Test, θ is measured from the end of the tape draping off a ledge (“O” in Figure 4-2c or Figure 4-3b) and the edge of the ledge (“S” in Figure 4-2c or Figure 4-3b) while the other end is fixed. The horizontal line going through “S” sets the reference for $\theta = 0^\circ$. The bending length (c) which is roughly related to the contour length of the bent portion of the tape can be related to l_h and θ (Eq. 4-10a).¹⁰² Figure 4-4a shows that as θ increases, c decreases which corresponds well with Eq. 4-10a. In literature, the expression containing θ is often substituted for $f(\theta)$ (Eq. 4-10b).^{9,102,103}

$$c = (l_h) \left(\frac{\cos \frac{\theta}{2}}{8 \tan \theta} \right)^{1/3} \quad (4-10a)$$

$$f(\theta) = \left(\frac{\cos \frac{\theta}{2}}{8 \tan \theta} \right)^{1/3} \quad (4-10b)$$

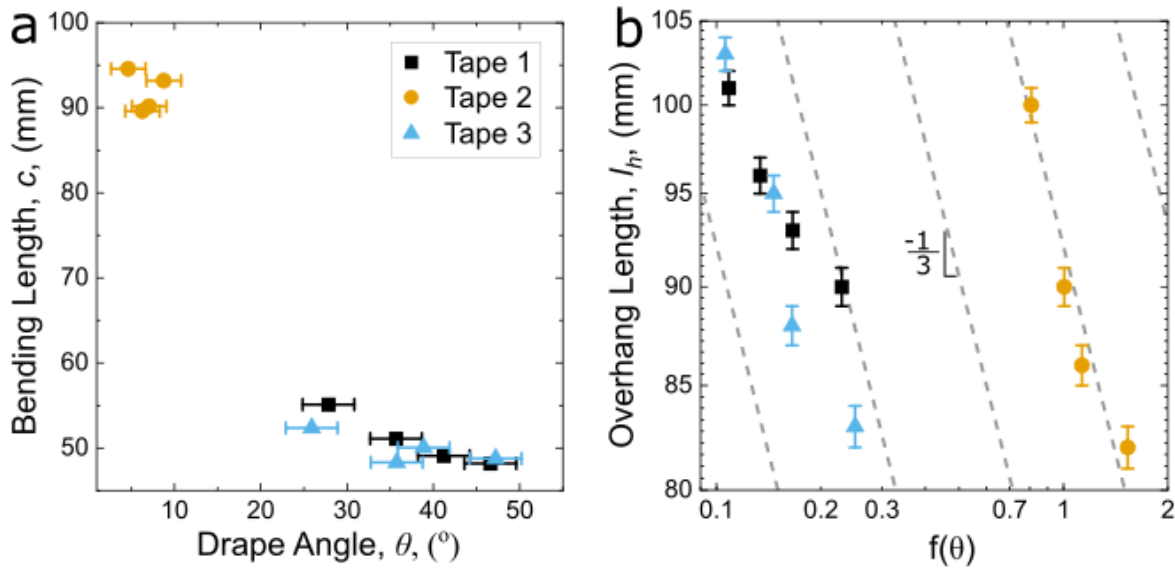


Figure 4-4. *a*) Tape Drape Testing plot of c with respect to θ . *b*) The scaling relationship between $f(\theta)$ and l_h . The parallel dashed lines have a slope of $-1/3$ and are a guide to the eye. The error bars in *a*) and *b*) represent a standard 5% measurement error.

The relationship between θ and l_h is shown in Figure 4-4b where the slope of the dashed lines are $-1/3$ which corresponds to $l_h \sim f(\theta)^{-1/3}$ when plotted on a log-log scale. Figure 4-4b shows that the relationship between θ and l_h in Eq. 4-10a holds for TPM tapes. Since the Tape Drape Test is typically used with textile materials, it is important to validate the test by showing that the methodology follows the relationship in Eq. 4-10a when testing TPM tapes. Once the Tape Drape Test is validated, c can be used to determine the flexural rigidity (G) through Eq. 4-11^{102,104},

$$G = (9.81 \times 10^{-12})(\omega)(c^3) \quad (4-11)$$

where ω is the areal density with units of g/m^2 ($\omega = m/ab$) and m is mass. G be related to E through t and the Poisson's ratio (ν) which was assumed to be 0.49 (Eq. 4-12).

$$E_{Drape} = (G) \left(\frac{12(1-\nu^2)}{t^3} \right) \quad (4-12)$$

Eq. 4-12 was used to determine E from the Tape Drape Test.

4.3 Results and Discussion

4.3.1 E Determination Technique Comparison

Representative F - Δl and σ - ε plots used to determine E from tensile testing are shown in Figure 4-5a and Figure 4-5c, and F - δ and σ_{bend} - ε_{bend} plots from three-point bend testing in Figure 4-5b and Figure 4-5d. E determined through tensile testing (E_{Tens}), three-point bend testing (E_{Flex}), and the Tape Drape Test (E_{Drape}) are reported in Table 2. E_{Flex} values reported in Table 2 are in relatively good agreement with E_{Tens} values of Tape 1 and Tape 2. Due to this agreement, E_{Flex} can be approximated as E_{Tens} .

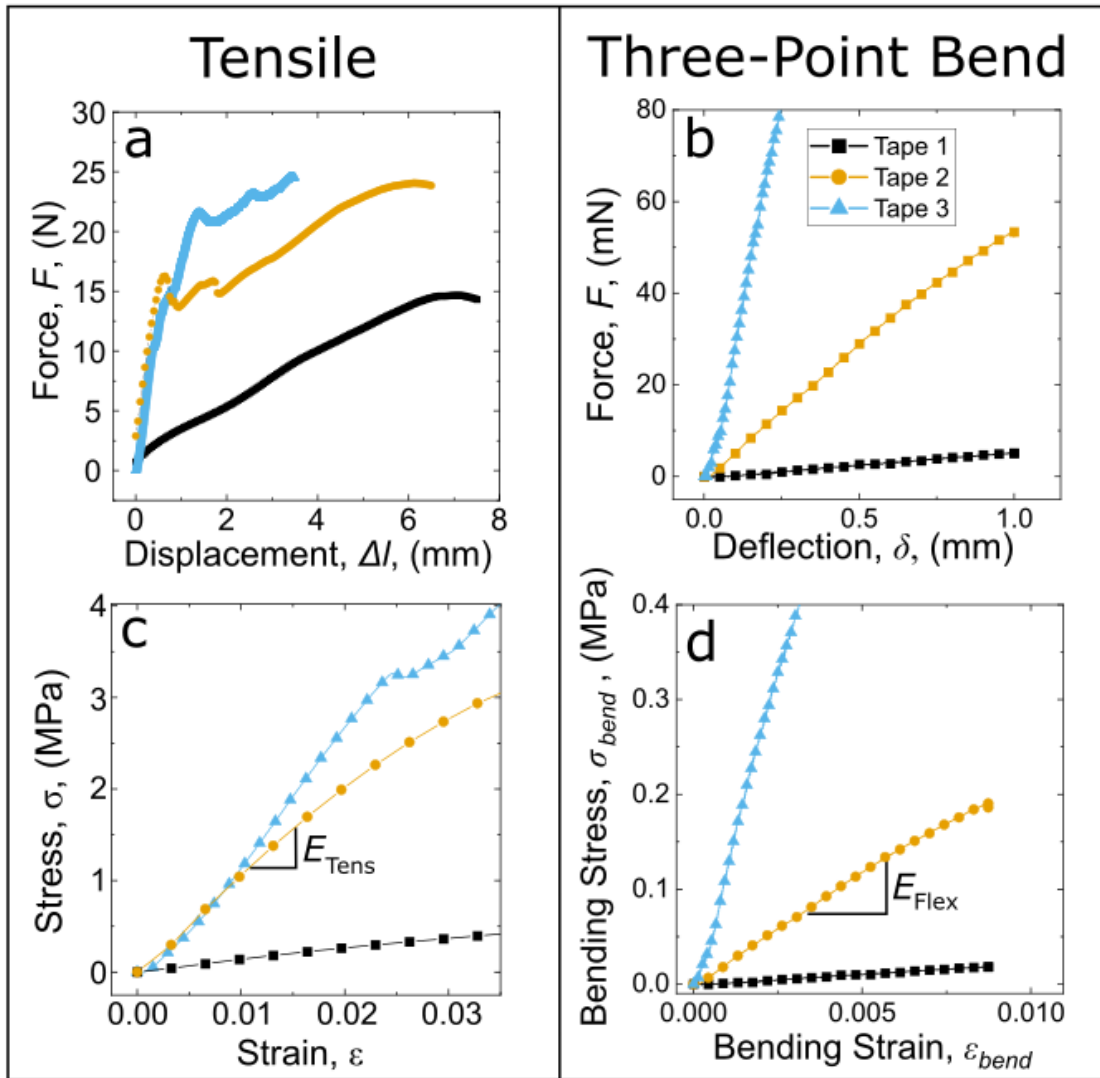


Figure 4-5. *a*) Representative force-displacement curves from tensile testing. *b*) Representative force-deflection curves from three-point bend testing. *c*) Initial portion of representative stress-strain curves from tensile testing. *d*) Initial portion of representative bending stress-bending strain curves from three-point bend testing. The legend in *b*) applies to all plots.

Table 4-1. Comparison of E Determined by Various Test Methods

	E_{Tens} (MPa)	E_{Flex} (MPa)	E_{Drape} (MPa)
Tape 1	7.70 ± 1.10	9.90 ± 2.40	14.8 ± 2.40
Tape 2	52.0 ± 13.20	44.6 ± 6.30	46.9 ± 1.80
Tape 3	124 ± 48.9	94.1 ± 10.1	15.9 ± 3.60

A graphical comparison of E determined by each measurement technique is shown in Figure 4-6. E values between all measurement techniques were in good agreement for Tape 1 and Tape 2 while Tape 3 had an average percent difference of 148% for E_{Tens} and E_{Flex} when compared to E_{Drape} .

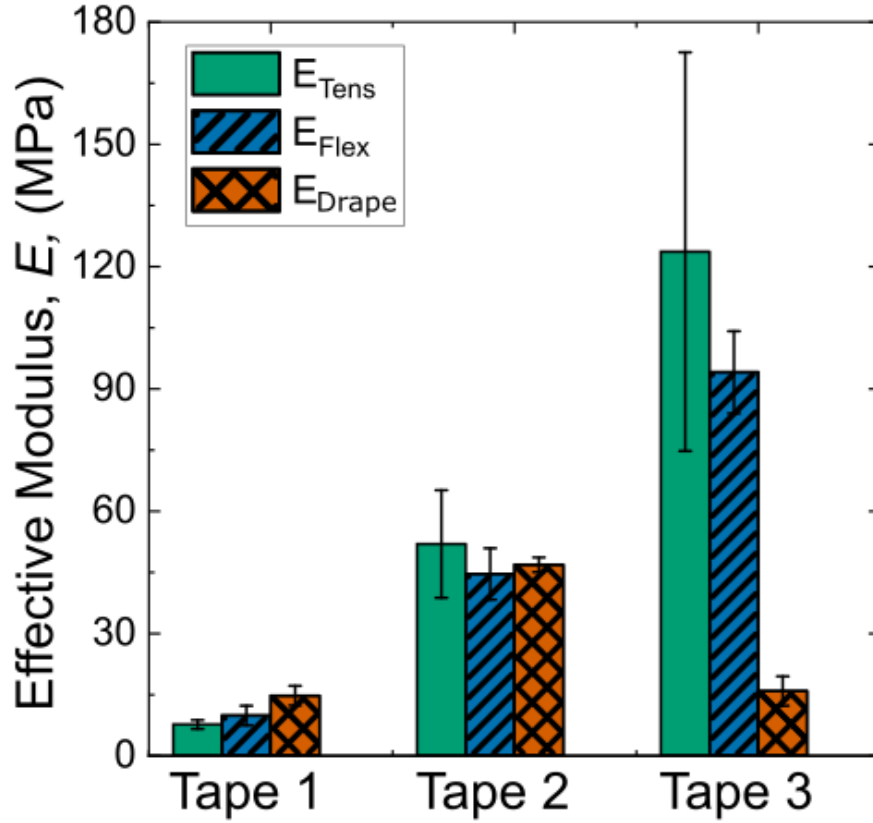


Figure 4-6. The measured E from tensile testing, three-point bend testing, and Tape Drape Testing for each tested tape. The error bars represent one standard deviation.

E is an intrinsic materials property that describes the resistance to deformation and can be qualitatively observed when handled. When physically manipulating Tape 1 and Tape 3, these two tapes appear to have similar E . However, the measured result found E_{Tens} of Tape 3 to be 177% different than E_{Tens} of Tape 1, 162% different for E_{Flex} , and 7% different for E_{Drape} . The large discrepancy between the measured E_{Tens} and E_{Flex} of Tape 1 to Tape 3 and the predicted E based on qualitative handling and manipulation indicate the traditional E characterization techniques have difficulty characterizing a trustworthy E value for TPM tapes.

The small percent difference between E_{Drape} of Tape 1 and Tape 3 correspond well with the physical hypothesis developed from handling the tapes. The agreement of the measured E values with the expected result from handling is a positive indicator that the Tape Drape Test can accurately measure E of TPM tapes while having the ability to be implemented in the field.

4.3.2 Tape Geometry and Composition Effects on E Measurement Techniques

A major difference between the traditional modulus measurement methods (tensile testing and three-point bend testing) and Tape Drape Testing is the requirement to cut specimens to a specific geometry for the conventional methods. The geometry and composition of the TPM tapes play a major role in E of the tapes. Tape 3 had significant variation in measured E values between the techniques, while Tape 1 and Tape 2 had relatively good agreement across all methods. While all the tapes are comprised of similar materials, the composition of the various layers and surface topographies are different. To ensure an appropriate assessment of tape modulus, tested specimens should be representative, when possible, of the product geometry that will be deployed on roadways.

Referring back to Figure 4-1, the most noticeable difference between the surface structures of all the tapes are the ridges on the top surface of Tape 3 (Figure 4-1cii). Upon further observation, the ridges on Tape 3 have a greater thickness, and therefore stiffness, than the underlying flat regions of this tape. Depending on whether one of these ridges was present on the three-point bend specimens, the measured E_{Flex} varied greatly. The Tape 3 specimens with ridges had a measured $E_{Flex} \approx 94\text{MPa}$ while a specimen without ridges measured $E_{Flex} \approx 21\text{MPa}$. By measuring E on portions of Tape 3 containing these raised ridges, a larger than expected value of E_{Flex} was observed in three-point bend test results for Tape 3.

During tensile testing, it is unlikely that the presence of ridges would create such a discrepancy in E_{Tens} from the expected value because deformation will occur first in the part of the gauge (i.e. between the ridges) with the smallest cross sectional area. Each tested tape has a plain weave fabric reinforcement between the polymer substrate and the adhesive layers. The woven structure on each tested TPM tape is shown in the inset of Figures 4-1ai, bi, and ci. This fabric backing layer increases the overall stiffness and strength of the TPM tapes. If the threads in the backing are stiff and strong, this feature will be effective in transferring load applied in the

axial direction causing an artificially high E_{Tens} . Additionally, the number of threads in the axial direction of a prepared sample will affect E_{Tens} . Depending on the number of threads in a tested sample the E_{Tens} value will vary which can cause high variability in the measurement of E_{Tens} . It is possible that these factors caused an artificially high value with a large variability of E_{Tens} for Tape 3.

The presence of ridges and the probable higher stiffness of the plain fabric weave reinforcement in Tape 3 specimens led to a large discrepancy between E_{Flex} and E_{Tens} measurements in comparison to the Tape Drape Test values. E_{Drape} reflected the expected E values from a tactile examination while E_{Flex} and E_{Tens} did not follow the expected trend for Tape 3 as a result of tape geometries affecting E determination during testing. The Tape Drape Test was not sensitive to the dramatic increase in E because these specimens were much larger, and the methodology does not call for any sample preparation or application of external forces allowing for the measured E to accurately characterize the tape.

The Tape Drape Test can easily be implemented for E characterization for TPM tapes. Prior to installation on roadway surfaces, the Tape Drape Test may be performed to assess E at the exact temperature of installation. Based on temperatures, a TPM tape with a higher or lower modulus can be selected to improve tape performance under the specific environmental conditions during installation. Further testing needs to be conducted to determine the exact effect that temperature has on E and therefore adhesion strength of TPM tapes on roadway surfaces. Currently, the Tape Drape Test will allow for real-time assessment of E prior to installation and inform decisions on which TPM tapes to apply based on temperature.

4.4 Conclusion and Implications

Traditional E characterization techniques require specific sample geometries that are not necessarily representative of the complete structure of TPM tapes. The three-point bend and tensile testing methods both require specific geometries prior to testing, while the Tape Drape Test only required specimens to be cut to length, leaving the structural features of the as-received materials intact. E was consistently characterized for Tapes 1 and Tape 2. For Tape 3, the results of the traditional test measurements were different from the Tape Drape Test results due to tape geometries. The Tape Drape Test was the only technique with the ability to characterize E of the

tapes with what is expected from a tactile assessment due to the sample being reflective of the as-received tape geometry. This reason leads to the conclusion that the Tape Drape Test is the most accurate of the three E characterization techniques when determining E for the TPM tapes.

One advantage the Tape Drape Test has over the tensile and three-point bend test is its simplicity, leading to the ability to be conducted in the field. Tensile testing and three-point bend testing both require a load cell and actuator, while the Tape Drape Test requires only a camera, ruler, and protractor. Most portable electronic devices can act as a camera, ruler, and protractor, making the implementation of the Tape Drape Test simple and straightforward. The major requirement to employ this technique is the need for a horizontal ledge. Some suitable ledge selections that can commonly be found on a roadway construction site are the edge of a truck bed, pieces of equipment, or hoods of vehicles.

Characterizing E in the field is important for TPM tapes because E of TPM tapes can change depending on the temperature. When temperatures drop below T_g , the TPM tapes will transition into a glassy phase, resulting in an increase in E . At room temperature (approximately 25 °C), TPM tapes are ductile, but as temperature increases, E of the tapes can decrease when the tape transitions to an even more ductile state. For most commercial TPM tapes, these transitions occur at temperatures that can be reached outside depending on the climate and season.

In laboratory conditions, room temperatures are customary unless special equipment is employed to characterize E at higher or lower temperatures. Characterizing E exclusively at 25 °C when tapes will be applied and removed over a fairly wide temperature range can adversely affect the prediction of tape adhesive performance in the field. The Tape Drape Test can be employed to overcome this challenge and allow for on-site E characterization of TPM tapes under the conditions in which they will be utilized.

Depending on the characterized E based on the temperature, the application and removal procedure may need to be modified to ensure tape durability and ease of removal. When the tape is in a more ductile state, a slower application rate will reduce stretching and any potential plastic deformation caused by the application procedure, thus improving durability. However, during the removal process, a faster removal rate will improve the ease of removal of TPM tapes. As a result of measuring E in the field, a more effective approach can be taken for the application and removal of TPM tapes.

Tensile testing and three-point bend testing were unable to effectively determine E of all the TPM tapes due to the presence of ridges on the surface of Tape 3 and plain fabric weave. The Tape Drape Test is able to account for these tape geometries which makes the technique more appropriate for characterizing E of TPM tapes. Additionally, the Tape Drape Test can be employed in the field, accounting for the temperature-dependent E variation upon application. The Tape Drape Test can effectively determine E of TPM and allows the option to be implemented in the field.

5. A METHODOLOGY FOR CALIBRATING MECHANOPHORE ACTIVATION INTENSITY TO APPLIED STRESS

5.1 Introduction

A MP is a molecule that undergoes a chemical change as a result of a mechanical stimulus^{105,106}. MPs are an up and coming technology to be used as self-reporting damage sensors in polymeric material systems in aeronautical¹⁰⁷, energy generation¹⁰⁸, and automotive industries^{109,110}. MPs that change color after a mechanical stimulus is applied are called mechanochromic MPs, and ones that change fluorescence behavior are called mechanoluminescent MPs¹². These types of MPs are usually selected for self-reporting damage sensing applications as a color/fluorescence change will indicate areas of mechanical deformation. By incorporating these molecules at interfaces or into the backbone of a polymer matrix real-time damage sensing can be observed in thermoplastic and thermoset based materials systems (Figure 5-1a). Previous work has shown MP incorporated materials systems can be utilized as non-destructive examination techniques¹¹¹, scratch damage detectors for coatings, and detectors for interfacial failure^{112–114}.

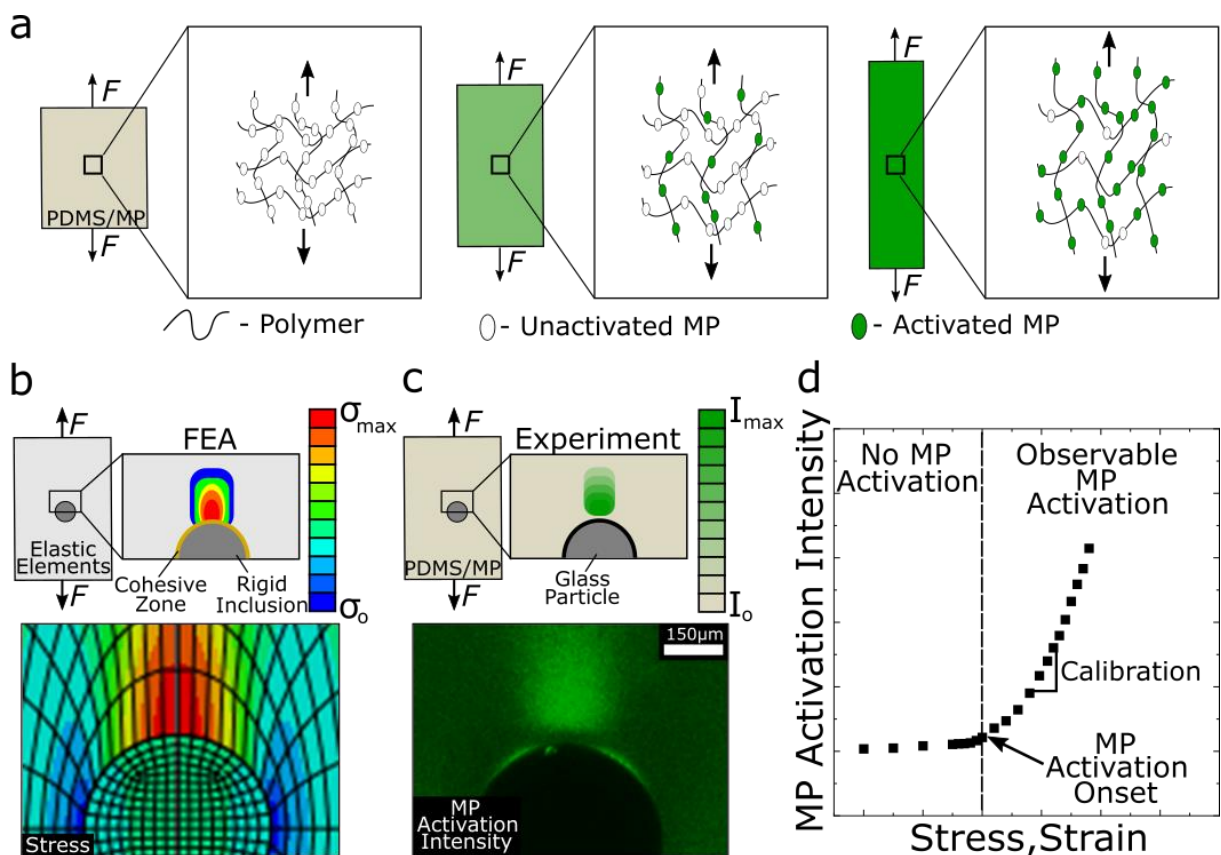


Figure 5-1. Experimental approach for calibrating experimental MP activation to stress using FEA. *a)* Progression of MP activation as uniaxial force is applied to the PDMS/MP system. The similar behavior of *b)* experimental MP activation near a glass particle in a PDMS/MP system with associated *c)* stresses determine through FEA simulations of an identical system. By combining the MP activation in *b)* and the determined stresses from *c)*, *d)* a calibration between MP activation intensity can be determined by the slope of the curve once MP activation is observable.

One of the most common MPs to be incorporated into polymeric systems is spiropyran (SPN). This was first done by Davis *et al.* who successfully incorporated SPN into PMA by observing an increase in chromatic intensity as deformation increased.¹⁷ In recent years, SPN has been incorporated into many different polymer matrices^{115,116}, with full-field fluorescence/fluorescence microscopy being utilized to observe the fluorescence activation.^{117,118} One such polymer matrix is polydimethylsiloxane (PDMS) which was first shown by the Craig group from Duke University.¹¹⁹ PDMS has been a widely used polymer matrix^{120,121} to aid engineers and researchers in understanding MP activation due to its well-characterized mechanical behavior and transparency.

SPN incorporated into PDMS or any other polymer backbone will only activate once the C-O spiro bond is broken which causes a molecular rearrangement that creates a series of conjugated C-C double bond that bridges the indole and pyran-benzene side (many schematics of the activation of SPN can be found in literature^{119,122,123}). The breaking of the C-O spiro bond will only occur once enough energy is input into the system to overcome the intrinsic activation energy of the SPN (ΔE_{act}). The rate of MP activation ($k(F)$) is then described by Eq. 5-1^{12,120,124},

$$k(F) \propto e^{-(\Delta E_{act} - F\Delta x)/RT} \quad (5-1)$$

where F is the applied force, Δx is the change in distance of the force path across the MP from the unactivated to the activated state, R is the gas constant, and T is the temperature. Eq. 5-1 reveals that the force required to activate a MP has a time scale dependence. As F increases, the rate in which MPs activate increases which results in areas of high MP activation being the areas of highest F or stress (Figure 5-1a).

MP activation has been mainly used as a qualitative or semi-quantitative assessment of deformation that correlates increasing MP activation intensity (I) with an increase in stress.^{112,113} To move MP technologies from the laboratory into industrial applications full quantification of applied stress as a function of I is required. Efforts to quantify this relationship have been conducted by Dee *et al.* who coupled digital image correlation (DIC) with a fracture experiment to determine a power law relationship between I and stress¹²⁵, and Chen *et al.* who mapped stress using a strain field around a crack tip during propagation from DIC with experimentally collected I of the same geometry.¹⁹

Here, a similar approach to Chen *et al.* is employed to propose a methodology for calibrating I to stress using stress concentrations create by a rigid inclusion in a PDMS matrix along with finite element analysis (FEA) to quantify stress. In fracture experiments, the crack tip acts as a stress concentrator that amplifies the stress at the crack tip. The amplified stress decreases as a function of distance from the crack tip creating a local stress gradient within the material moving away from the crack tip. The same phenomenon occurs in particulate composite systems. In this case, the particulate in a matrix acts as a stress concentrator causing a local stress concentration gradient within the material moving away from the particulate/matrix interface (Figure 5-1b).^{126,127} Since I scales with stress, a stress concentration gradient caused by a rigid inclusion creates a I gradient (Figure 5-1c).¹²⁸ Through using distance from the particle interface

as a correlator, the stress concentration gradient to the I gradient can be directly paired at every strain value until failure creating a systematic methodology for calibrating I to stress.

By modifying the rigid inclusion adhesion to the matrix creates different stress states within the materials system at similar strains (ϵ). With access to a variety of stress states, each corresponding to I , a comprehensive evaluation, and verification of the proposed calibration methodology is able to be rapidly performed. However, without knowing the exact stress at each point along the stress concentration gradient, the I correlation to stress remains semi-quantitative. To characterize stress at each point along the stress concentration gradient, FEA is employed to model the material system and quantitatively predict the stress concentration gradient. Through combining experimentally determined I with FEA determined hydrostatic stresses (σ_h) as ϵ increases of the same materials systems, a systematic I to applied stress calibration methodology is achieved (Figure 5-1d).

In this study, experimental I from a PDMS/SPN system embedded with a spherical glass particle is characterized through micro-mechanical testing coupled with laser scanning confocal microscope (Figure 5-2) and paired with FEA of the same system to develop a calibration methodology between σ_h and I . The adhesion of the glass particle to the matrix was modified to create three different adhesive strengths (low, moderate, and high) allowing for the calibration to be performed utilizing multiple stress states.¹²⁹ Several FEA simulations of different adhesions of the glass particle to the matrix were ran to find a solution that most closely matched the three different particle adhesions. The highest adhesion case is utilized to propose the methodology while the low adhesion case is presented as verification and to show the robustness of the presented I to σ_h calibration methodology. Additionally, the MP concentration in the PDMS matrix was changed to show the ability of the methodology to determine a I to σ_h calibration with different material systems. By using the experimentally determined I and FEA determined σ_h profiles as a function of distance from the glass particle/PDMS interface as a correlator, a quantitative relationship between I and σ_h was determined, called the calibration value, and a systematic calibration methodology was established. The method described here to calibrate I to σ can be used to calibrate any MP functionalized polymer system to applied stress.

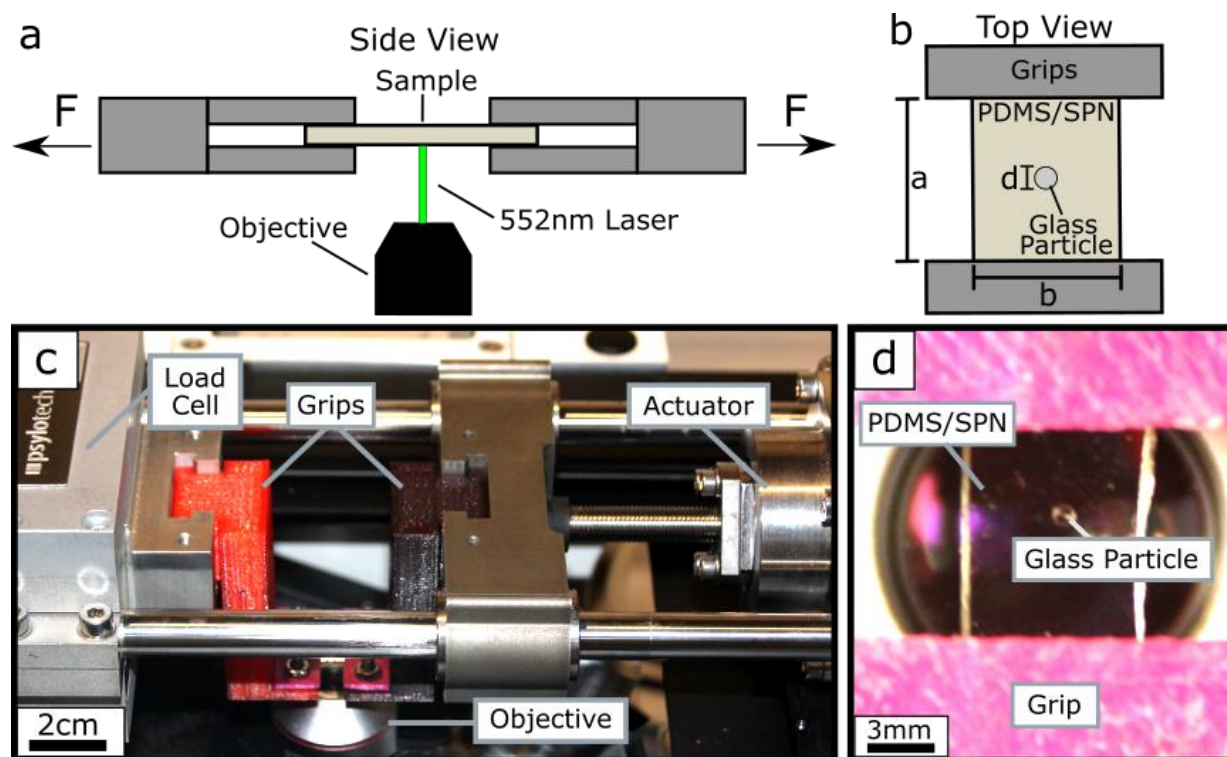


Figure 5-2. Schematics and actual images of the experimental set-up. Schematics of *a*) the coupling of the mechanical testing and confocal microscopy using a 552nm laser and *b*) a PDMS/SPN embedded with a glass particle sample mounted for testing. Actual images of *c*) the mechanical testing frame coupled with a confocal microscope and a close-up of *d*) a PDMS/SPN sample with a glass particle embedded mounted for testing in the grips.

5.2 Materials and Methods

5.2.1 Materials Preparation

Spiropyran Synthesis

Compound 1, shown in Figure 5-3, was synthesized in accord to the previous literature report.¹⁸ Compound 1 (3 g, 8.14 mmol, 1.0 equiv), *N,N'*-dicyclohexylcarbodiimide (4.20 g, 20.35 mmol, 2.5 equiv), 4-dimethylaminopyridine (248.61 mg, 2.035 mmol, 0.25 equiv) and 200 ml of dichloromethane were added into a round bottom flask. 4-Pentenoic acid (2.08 ml, 20.35 mmol, 2.5 equiv) was added and then the reaction mixture was stirred for 12 h. The reaction mixture was passed through a plug of silica gel with dichloromethane as the eluent until the filtrate became transparent. Removal of solvent *in vacuo* yielded a viscous purple oil and subsequent recrystallization from boiling hexanes afforded SP1 as a yellow crystal (3.74g,

86.4%). Characterization by ^1H NMR is in good agreement with literature data.¹⁸ HRFD-MS (m/z): $[\text{M} + \text{H}]^+$ calcd for $\text{C}_{30}\text{H}_{32}\text{N}_2\text{O}_7$, 532.22; found, 532.2204.

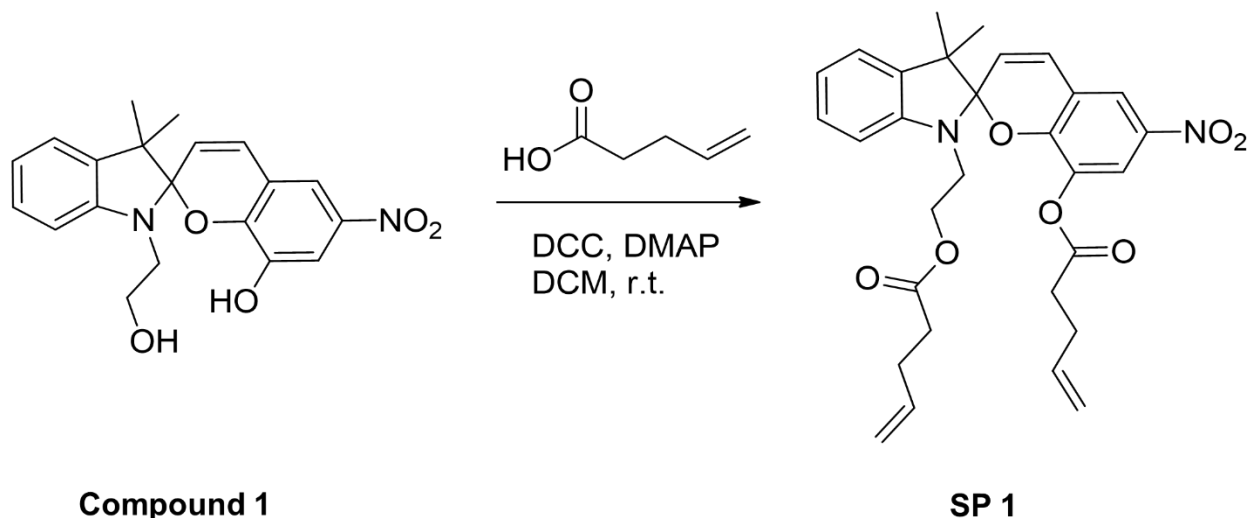


Figure 5-3. The reaction for synthesizing diene functionalized spiropyran.

Preparation of PDMS-SPN-Glass Inclusion Materials System

The PDMS/SPN samples were made in accordance with previously reported preparations in literature.^{18,130,131} 1.5g of Sylgard 184 Part A was mixed with 0.15g of Sylgard 184 Part (PDMS). A ratio of 15mg of SPN to 1mL of xylene was used to make samples containing 0.5wt%, 0.6wt%, and 0.7wt% SPN, and added to the PDMS mixture. The PDMS/SPN mixture was vortex mixed for 5 min at 2000 RPM. After degassing, half the mixture was poured into a glass mold and cured at 70°C for 5 min at which point a glass particle was added then covered with the remaining PDMS/SPN mixture. The PDMS/SPN was cured at 70°C for 24 hrs.

Glass Particle Surface Modification

Glass particles (Sigma-Aldrich) with a diameter (d) of 0.5mm were washed with hexane and rinsed with water. The particles were placed in an oven at 70°C until dry. For the low adhesion case, the glass particle was incorporated into the PDMS/SPN mixture directly after drying. For the medium adhesion case, the glass particles were incorporated into the PDMS/SPN mixture after oxygen/plasma (Glow, Glow Research) treating for 30 min and allowed to rest for 20min. For the high adhesion case, the glass particles were incorporated into the PDMS/SPN mixture immediately after oxygen/plasma treating for 30min.

5.2.2 Methodologies

Uniaxial Micro-Mechanical Testing

Rectangular samples with a length (a) of 7 ± 0.1 mm, width (b) of 4 ± 0.1 mm, and thickness (h) of 1 ± 0.05 mm were cut with a razor blade. The samples were tested uniaxially at a displacement rate of $15\text{ }\mu\text{ms}^{-1}$ (Psylotech, μTS) until fracture using 3D printed polylactic acid grips that allow for the sample to be in a proper working distance of the microscope objective (Figure 5-2b-d). A comparison between the global stress (σ_{global}) - strain (ϵ) behavior of the PDMS/SPN samples when testing with the dropped down grips instead of the Psylotech manufactured grips shows a significant difference in mechanical behavior (Figure 5-4). Testing the sample below the plane where actuation occurs creates a bending stress (σ_{bend}) and deflection (v) in the dropped down grips. The bending stress in the dropped down grips causes an underestimation in the force (F) measured by the load cell while the deflection causes an underestimation in the displacement of the displacement encoder of the μTS .

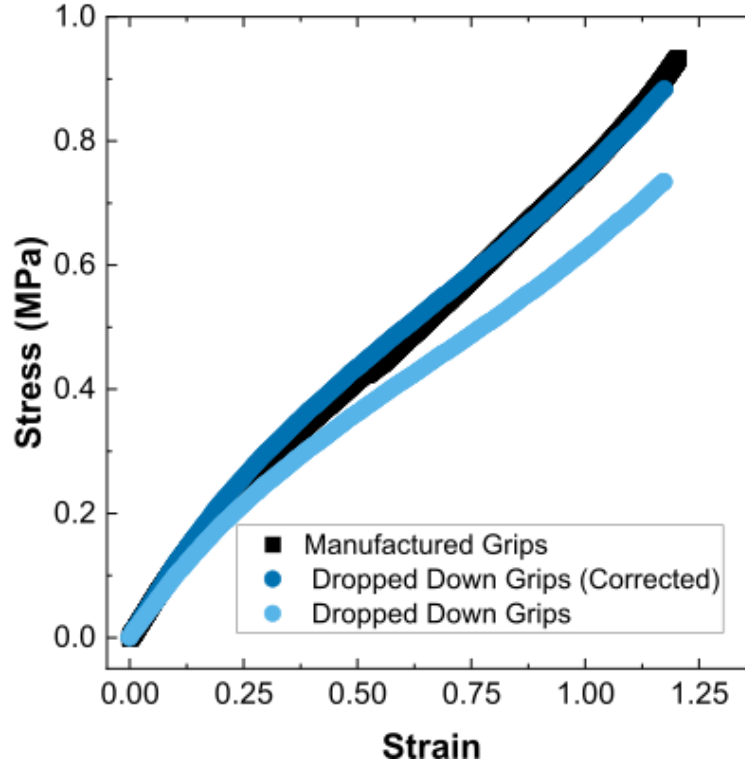


Figure 5-4. $\sigma_{global} - \epsilon$ behavior of the PDMS/SPN materials system when testing with the dropped down grips (before and after correcting for σ_{bend} and v) and manufactured grips.

By using, $\sigma_{bend} = My/I$ and $v = FL^3/3EI$ where M is the bending moment, y is the vertical distance from the neutral axis, I is the moment of inertia, L is the span, and E is the elastic modulus of the dropped down grips a correction was made to the $\sigma_{global} - \epsilon$ data for the dropped down grips.^{13,132} To obtain the corrected σ_{global} and ϵ values, σ_{bend} was added to calculated σ_{global} values and v was added to the calculated ϵ for each trial. After applying the σ_{bend} and v corrections to samples tested with the dropped down grips, the $\sigma_{global} - \epsilon$ behavior agreed well with the Psylotech manufactured grips (Figure 5-4). For each particle surface modification, a minimum of seven trials were conducted using a new sample every trial.

Confocal Microscopy

During micro-mechanical testing, laser scanning confocal microscopy (SP8, Leica) was employed to observe the fluorescence I . The microscope setting configuration was set-up with a gain of 550, pixel size of $4.55 \mu\text{m} \times 4.55 \mu\text{m}$, and an image size of $2.32\text{mm} \times 2.32\text{mm}$. For each

trial, a 12-bit image was captured at the mid-plane of the glass particle every 30 μ m of displacement illuminating the sample with a 552nm laser at 10% power and observing light wavelengths from 625nm-750nm¹⁸ with a photomultiplier tube.

Image Processing

All images were processed using ImageJ. The template matching plug-in was utilized to center the glass inclusion in all frames. The mean gray value measurement was used to determine MP activation intensity and normalized using the procedure discussed in a later section. No image modifications or processes were performed before determining the MP activation intensities.

Finite Element Analysis

FEA was performed using Abaqus. A 2D mesh geometry was created using symmetry about the 2 direction to model the PDMS/SPN/glass particle system using the same geometries as the experiment. The PDMS/SPN system was modeled using elastic elements and the adhesion of the particle to the matrix was modeled using cohesive zone elements (Figure 5-5a-b). The elastic modulus and Poisson's ratio selected to model the rigid inclusion elements are typical values for glass which were 70 GPa and 0.2, respectively^{133,134}, while the elastic modulus chosen for the PDMS/SPN elements was determined experimental to be 0.95 MPa and a literature value for Poisson's ratio was chosen to be 0.49.¹³⁵ The boundary conditions were selected based on the experimental set-up where the bottom of the mesh was fixed with the top of the mesh experiencing the applied force (Figure 5-5c).

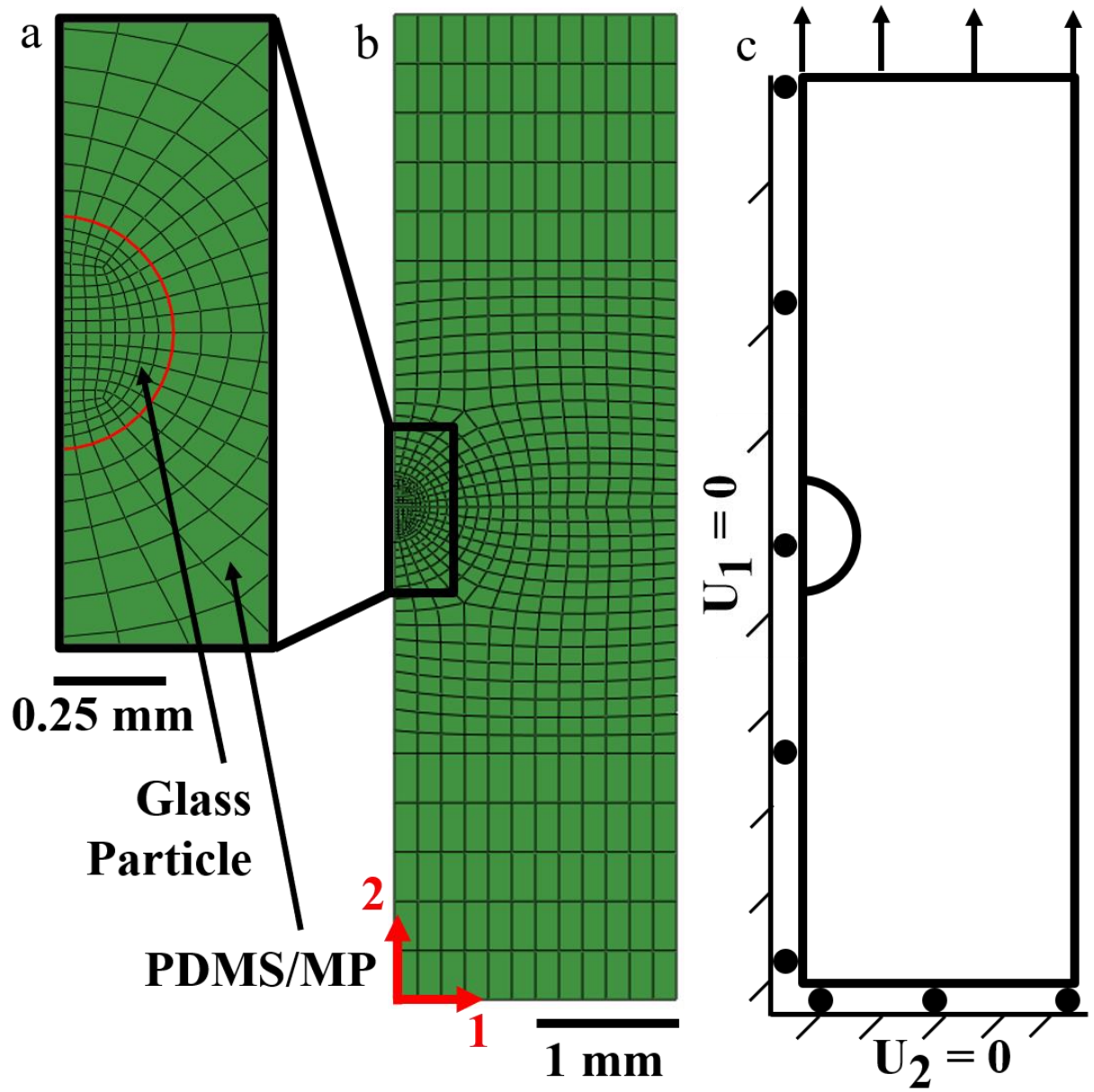


Figure 5-5. The finite element model for the PDMS/MP system. *a)* The mesh near the PDMS/MP glass bead interface (highlighted in red). *b)* The mesh of the PDMS/MS system with a glass particle. *c)* The axially loaded boundary conditions applied to the PDMS/MS system.

5.3 Results and Discussion

5.3.1 MP Activation Near a Glass Particle

The volume percent (vol%) of particles in a matrix and the adhesion of each particle to the matrix affect the mechanical behavior of the materials system.¹³⁶ Here, the particle vol% is less than 2% and would not be expected to have a significant effect on the mechanical behavior. To ensure similar global mechanical responses between the particle adhesion cases, $\sigma_{global} - \varepsilon$ a comparison between all particle adhesion cases results in similar mechanical responses (Figure 5-6a).

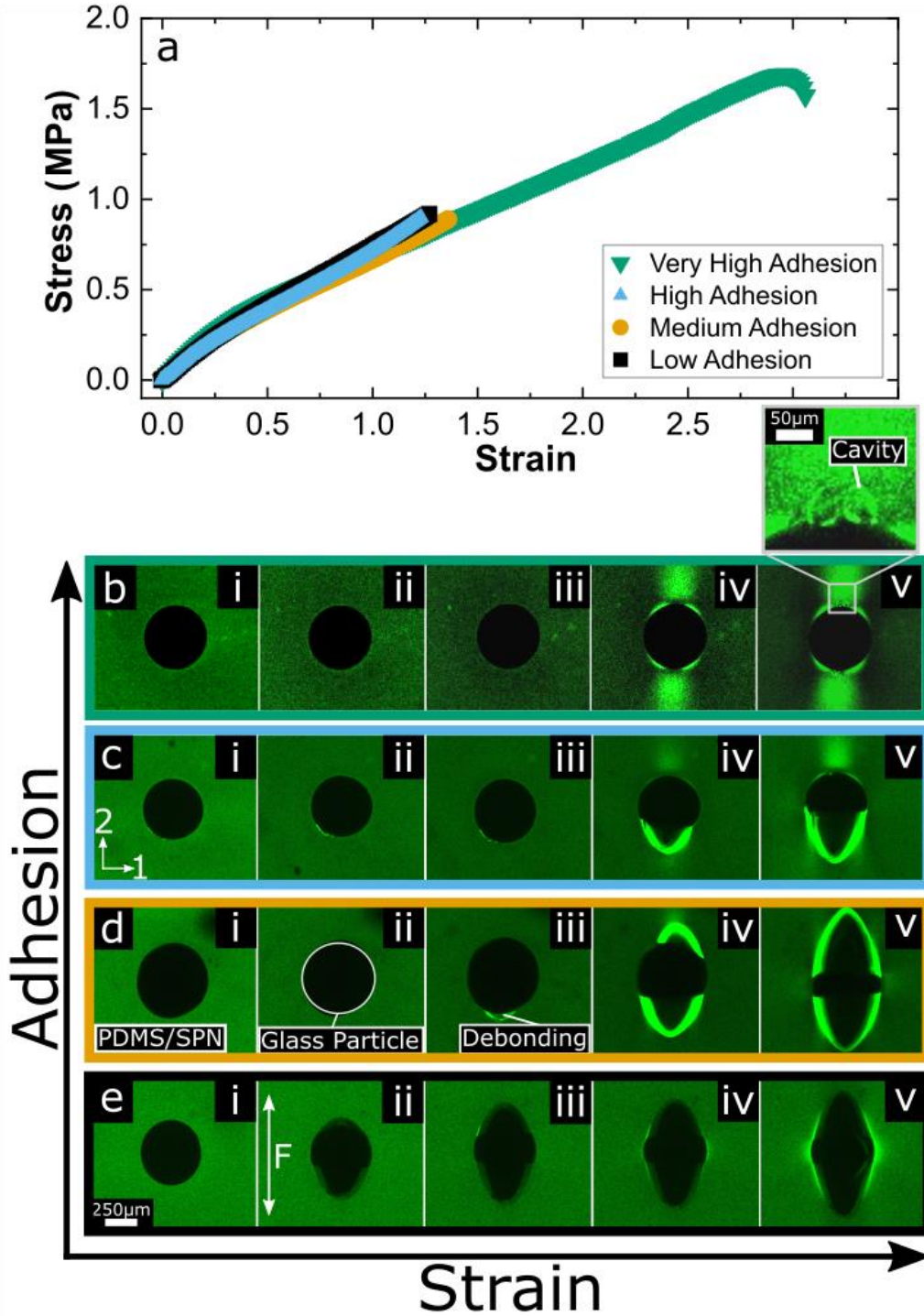


Figure 5-6. The mechanical behavior of the PDMS/SPN matrix embedded with a glass particle of different interfacial adhesion and corresponding confocal microscopy images as ε increases. *a)* Stress-strain curves of a PDMS/SPN with an imbedded glass particle with different interfacial adhesions. Images of the PDMS/SPN-glass particle behavior as ε increases for different interfacial adhesions with *b)* being the very high adhesion, *c)* being the high adhesion, *d)* being the medium adhesion case, and *e)* being the low adhesion case.

To further verify our assumption of negligible particle and particle adhesion effects on mechanical behavior, a very high particle adhesion case was tested and compared to the other three adhesion cases in Figure 5-6a. For the very high adhesion case, the material system was able to double the elongation of the other adhesion cases due to no debonding of the matrix from the particle. The main mechanical behavior differences between the very high adhesion case and the low, medium, and high adhesion cases is the strain at which the particle debonds from the PDMS/SPN matrix. Debonding occurred much earlier during testing for the low, medium, and high adhesion cases than the very high adhesion case (Figure 5-6b-e) causing fracture to occur earlier.

Debonding initiates from an already debonded region or flaw initially at the interface and expands gradually or catastrophically depending on the magnitude of the applied stress once the critical value is met.^{137,138} Once debonding occurs, the newly created free surface from the debond becomes the site of crack propagation initiation as deformation continues leading to failure. For the very high adhesion case, the particle remained bonded to the matrix until fracture preventing crack propagation caused by the free surface created from debonding (Figure 5-6bi-v) which was not observed in the low, medium, and high adhesion cases.

At large strain values, the local dilatant stresses near the interface are enough to cause cavitation which is the rapid expansion of a small spherical cavity in elastomeric materials.^{139,140} Cavitation is observed for the very high adhesion, seen in the inset of Figure 5-6bv which is indicative of large a local hydrostatic stress concentration near the particle-matrix interface. Observing cavitation near the interface with the $\sigma_{global} - \epsilon$ response while maintaining the same mechanical behavior as the other adhesion cases is further evidence of the particle adhesion having no effect on the global mechanical behavior of the materials system allowing for I to be compared for each case.

In each adhesion case, the stress far away from the particle-matrix interface (σ_{∞}) were all similar, but near the particle-matrix interface, the three different surface treatments of the glass particle resulted in three different local stress states (Figure 5-6c-e). As F is applied in the 2 (vertical) direction, the high adhesion case (oxygen plasma treated with immediate incorporation into the matrix) had sufficient adhesion to observe a MP activation gradient in the 2 direction near the particle-matrix interface.^{126,141}

The high adhesion case had no changes near the glass particle during the early stages of deformation (Figure 5-6ci-iii). Without an early onset of debonding, the stress concentration in the 2 direction increases leading to observable MP activation (Figure 5-6civ). As deformation continues to increase, debonding occurs at one of the poles of the particle while the MP activation gradient increasing at the opposite pole. Due to the polymer chains near the interface having a greater resistance to deformation when bonded to the glass particle a stress concentration develops in the PDMS/SPN matrix that increases as deformation increases.^{126,127} The debonded region elongates and I gradient continues to increase in intensity comparing Figures 5-6civ-v until fracture occurs. For the high adhesion case, I was characterized in the 2 direction to be paired with the FEA determined σ_h of the same response.

The medium adhesion case (oxygen plasma treated with a 20 min wait before embedding) caused a stress state and debonding behavior of the matrix to be in between the low and high adhesion cases. The material system had no changes near the glass particle/matrix interface (Figure 5-6di-ii) until debonding occurs seen in Figure 5-6diii. As deformation continues, the debonded region grows with the opposite pole eventually debonding (Figure 5-6div). Both debonded regions continue to grow in the 2 direction until crack propagation occurs at the newly created free surface from debonding (Figure 5-6dv).

The presence of interfacial adhesion is evident from the debonding event causing MP activation (Figure 5-6div). Before debonding occurs stress concentrates near the particle/matrix interface in the 2 direction on the poles of the particle. When the matrix debonds at both poles of the particle, the stress concentration moves from the poles in the 2 direction to the poles in the 1 direction which can be seen comparing Figures 5-6div-v. Because of the stress concentration switching directions during the experiment and the time rate dependency on MP activation, I is unable to be accurately compared to σ_h determined by FEA.

As F is applied in the 2 direction, the low adhesion case (only rinsed with hexane and DI water) caused a full slip condition that behaved similarly to a spherical void.^{126,142} The PDMS detached early during deformation (Figure 5-6ei-ii) from the glass particle and continued to grow (Figure 5-6biii) until the onset of MP activation (Figure 5-6eiv). Upon further deformation, the stress concentration gradient is observed at 90° from the pulling direction (1 direction) causing a MP activation gradient in the same direction (Figure 5-6ev).^{126,143} In the low adhesion case, the reduction in cross-sectional area is greatest at the mid-plane of the spherical cavity created by the

full slip condition of the glass particle causing the greatest stress to occur near the particle/matrix interface which decreases moving away from the interface in the 1 direction. For the low adhesion case, I was characterized in the 1 direction to be paired with the FEA determined σ_h of the same response.

5.3.2 FEA Simulations of a Rigid Inclusion Imbedded in a PDMS/SPN Matrix

Hyperelastic materials, such as PDMS, are known to have complex non-linear mechanical behavior which creates difficulty in determining stresses experimentally, especially at the mm to μm length scales. FEA of hyperelastic materials has been well studied utilizing many different models to predict mechanical behavior.^{144–146} Models for hyperelastic mechanical behavior are derived for the strain energy function (W) (Eq. 5-2)¹⁴⁷,

$$W = f(I_{v,1}, I_{v,2}, I_{v,3}) \quad (5-2)$$

where $I_{v,1}$, $I_{v,2}$, and $I_{v,3}$ are the strain invariants in the 1, 2, 3 direction, respectively. The strain invariants are typically defined in terms of principal stretch ratios in the 1 (λ_1), 2 (λ_2), and 3 (λ_3) directions (Eq. 5-3a-b)¹⁴⁸,

$$I_{v,1} = (\lambda_1)^2 + (\lambda_2)^2 + (\lambda_3)^2 \quad (5-3a)$$

$$I_{v,2} = (\lambda_1\lambda_2)^2 + (\lambda_2\lambda_3)^2 + (\lambda_3\lambda_1)^2 \quad (5-3b)$$

with $I_{v,3} = 1$ when assuming PDMS is incompressible and $\lambda = 1 + \varepsilon$.

Three constitutive hyperelastic models (Ogden¹⁴⁹, Neo-Hookean^{150,151}, Mooney-Rivlin^{150,151}) previously used for PDMS and that are available in Abaqus, were selected as potential candidates to model the PDMS/SPN material system^{144,152,153}. By inputting experimental σ_{global} and ε data, the selected hyperelastic models were simulated and compared with the experimental σ_{global} - ε data for accuracy. The Neo-Hookean and Mooney-Rivlin models diverged from the experimental data at larger strain values, respectively, while the Ogden model fit the experimental data well and was selected as the constitutive hyperelastic model for FEA, where α_i and μ_i are temperature dependent coefficients (Eq. 5-4).

$$W = \sum_{i=1}^N \left(\frac{2\mu_i}{\alpha_i^2} \right) (\lambda_1^{\alpha_i} + \lambda_2^{\alpha_i} + \lambda_3^{\alpha_i} - 3) \quad (5-4)$$

The Ogden model was used to simulate the hyperelastic behavior of the PDMS/SPN matrix (Eq. 5-4), while the glass particle/PDMS interface was modeled by a cohesive zone element

formulation. The cohesive zone element formulations follow normal traction and shear separation curves using the quadratic nominal stress criteria¹⁵⁴ to model the interface before damage and the Benzeggagh-Kenane fracture criterion¹⁵⁵ to model the damage evolution after debonding occurs. By modifying the cohesive zone parameters (cohesive stiffness (k), cohesive strength (t), and critical fracture energy (G)) different adhesions of the glass particle to matrix were simulated. The ranges of k , t , and G were selected based on previous work.^{156–159}

Twenty seven different simulations were ran, each with a different combination of k , t , and G to capture a similar local mechanical behavior near the glass particle/matrix interface to the observed responses in the three adhesion cases. Runs that numerically diverged or fractured prior to fracture strains experimentally observed were not considered. For the remaining runs, the simulated σ_h , stress in the 2 direction (σ_{22}), and stress in the 1 direction (σ_{11}) were analyzed to determine the appropriate stress type to correlate to I . It is expected that the hydrostatic stress near the interface (σ_{Int}) of a rigid inclusion adhered to an elastomeric matrix or spherical cavity in an elastomeric matrix is $2\sigma_\infty$.^{126,136} Because of this known relationship σ_h was chosen as the stress type to be compared to I where $\sigma_{Int} = 2\sigma_\infty$ was used to select the appropriate FEA simulation

The run selected to model the low adhesion case modeled the stress concentrating in the 1 direction with $\sigma_{Int} \approx 1.8\sigma_\infty$, and the selected run to model the high adhesion case modeled the stress concentrating in the 2 direction with the hydrostatic stress at the interface being $\sigma_{Int} \approx 1.9\sigma_\infty$. Since the FEA determined σ_h values agree well with estimated local stress values near the interface, comparing σ_h to I is appropriate.

5.3.3 Characterizing the I and σ_h Concentration Gradients

Due to the asymmetric debonding behavior seen in the high adhesion case, a distinct I gradient is observed consistently in the 2 direction at higher strains. Therefore, the high adhesion case will be utilized to establish I to σ_h calibration methodology and compared to the results when the same methodology is used for the low adhesion case. Images of the chosen FEA simulation to model the high adhesion case are compared to images of the MP activation for the high adhesion case as strain increases in Figure 5-7ai-v and Figure 5-7bi-v.

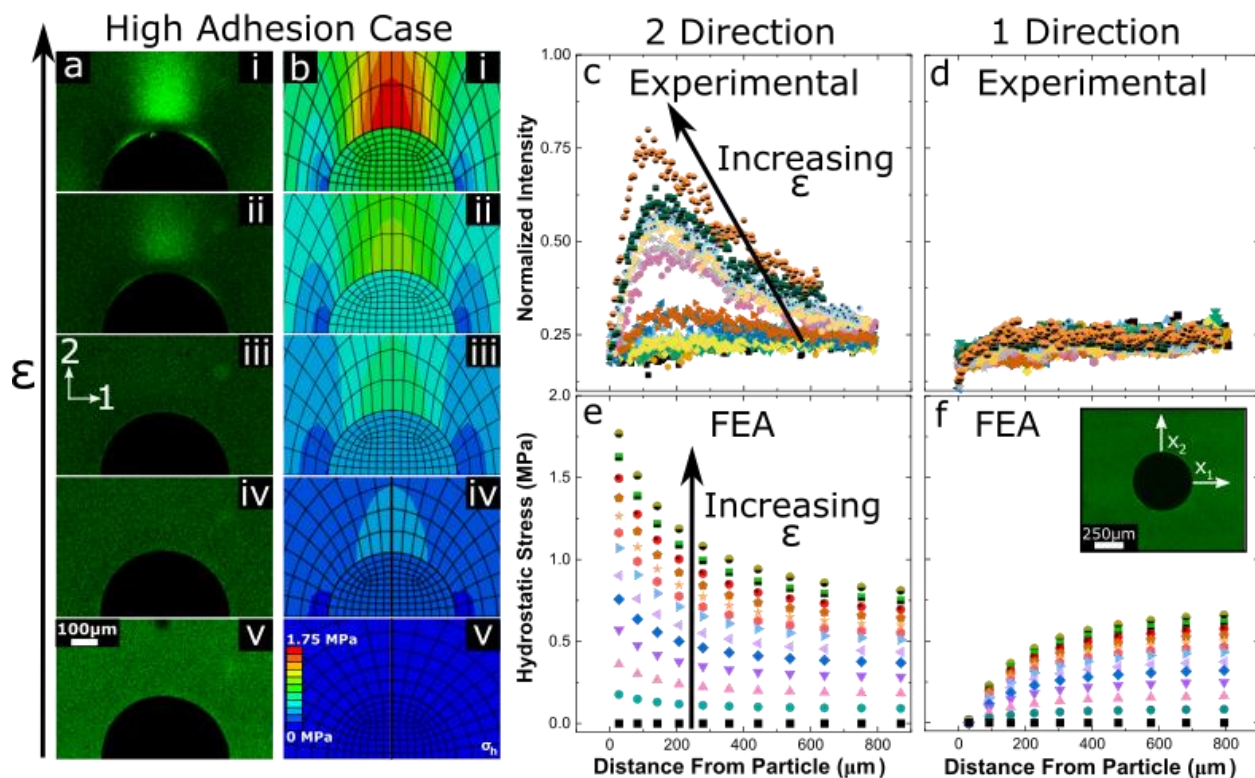


Figure 5-7. Relating and characterizing I with FEA determined σ_h as a function of x_2 and x_1 . Images comparing *ai-v*) the MP activation response and *bi-v*) the FEA determine σ_h concentration gradient for the high adhesion case. I as a function of *c*) x_2 and *d*) x_1 . The FEA determined σ_h as a function of *e*) x_2 and *f*) x_1 .

The region of interest for correlating I to σ_h is the stress concentration gradient and MP activation gradient seen in the upper half of the images in Figure 5-7a-b. The behavior of the pole opposite to the pole examined in Figure 5-7a-b does not affect I or σ_h of the examined pole. Therefore, only one pole needs to be characterized for the two quantities to be correlated. As ϵ increases, the experimentally determined I (Figure 5-7ai-v) increases with the FEA determined σ_h concentration gradient increases (Figure 5-7bi-v). Since the I or σ_h behaviors match well, σ_h and I concentration gradients as a function of distance from the particle/matrix interface were characterized to be paired.

The I gradient was characterized by examining the I profile as a function of distance from the glass particle/PDMS interface in the 2 direction (x_2) (Figure 5-7c) and 1 direction (x_1) (Figure 5-7d). The I profile was taken over a distance of approximately 800 μm with a line width of 30 μm in 2 and 1 directions. The mechanophore activation intensities were initially taken as gray scale

values via ImageJ, and normalized using a UV activated calibration curve specific to the SPN concentration and imaging settings (Figure 5-8). The yellow curve in Figure 5-8 was taken at the higher, more sensitive imaging settings for the 0.5wt% system and the black curve was taken at the same microscope settings as the 0.6wt% and 0.7wt% for the 0.5wt% SPN system. To obtain the UV calibration curves, each PDMS/SPN system was progressively activated by a 405nm laser at 1% power that scanned the sample every 1.5 sec over the course of 240 sec. The normalization value used to normalize the gray scale intensities was determined by finding the corresponding intensity value at the x-coordinate (time) of the intersection of linear regressions taken 25 sec from the global maximum and minimum of each curve. In Figure 5-8, I was normalized relative to the critical point of a UV activation calibration curve for a 0.6wt% SPN/PDMS system. Normalizing I to UV activated SPN have been previously performed.^{116,160}

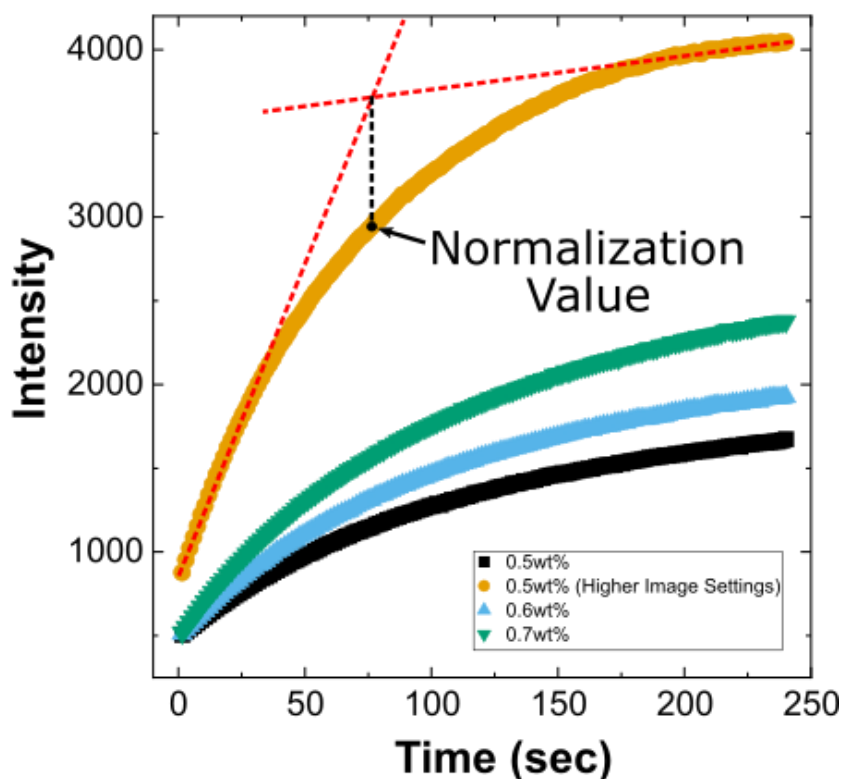


Figure 5-8. The UV activated calibration curves for intensity normalization of PDMS functionalized with 0.5wt%, 0.6wt%, and 0.7wt% SPN. The yellow data intensity values were taken a higher gain and laser power to increase sensitivity. The red dotted lines show how the normalization value was determined for each calibration curve.

To remove a decrease in intensity due to volumetric changes during testing^{116,117}, the normalized intensities were adjusted to the background intensity just before the onset of MP activation (the normalized intensity background value at $\varepsilon = 0.8$ for the high adhesion case). As ε increases, I in the 2 direction became observable at $\varepsilon \geq 0.8$ and begins increasing until fracture at $\varepsilon = 1.3$ (Figure 5-7c). I reaches a peak value near at $x_2 \cong 100\mu\text{m}$ which corresponds to Figure 5-7ai. The area of low stress near the glass particle/matrix interface has been observed in previous work^{141,142,161}, and most likely attributed to stiffness differences in the matrix near the glass particle/matrix interface. Beyond the peak of I , as the distance from the glass particle/PDMS interface increases, I decreases which is dependent on the decrease in σ_h until σ_∞ is reached which is the expected behavior for σ_h in the 2 direction (Figure 5-7e).¹⁶²⁻¹⁶⁴

I in the 1 direction has no sudden increase near the glass particle/PDMS interface as the glass particle only acts as a stress concentrator in the 2 direction for the high adhesion case (Figure 5-7d). The corresponding σ_h profile in the 1 direction increases as ε increases moving away from the glass particle/PDMS interface until σ_∞ is reached which is the expected behavior for σ_h in the 1 direction (Figure 5-7f).^{142,163,165} The σ_h and I profiles in the 1 direction provide evidence that a stress concentration is only occurring in the 2 direction. The I and σ_h profiles moving away from the glass particle/PDMS interface in their respective directions correspond well with one another which indicates the two quantities are related and can be paired to one another via x_2 to create a I to σ_h calibration.

5.3.4 The Methodology for Calibrating I to σ_h

Since I and σ_h behave similarly moving away from the glass particle/PDMS interface, the two quantities are related by matching I and σ_h at identical x_2 values for a direct comparison. The relationship between I and σ_h is shown in Figure 5-9a. Until the onset of MP activation at $\varepsilon = 0.8$, there is no change in I as σ_h increases. Once the onset of MP activation occurs, a transition state regime is observed between $0.9 \leq \varepsilon < 1.0$ before a linear steady state regime is established with a slope of at $0.280 \pm 0.002 \text{ MPa}^{-1}$ for $\varepsilon \geq 1.0$ where \pm represents one standard deviation (Figure 5-9b). The constant rate of change between I and σ_h in the steady state regime is taken as the calibration value of I to σ_h for the high adhesion case.

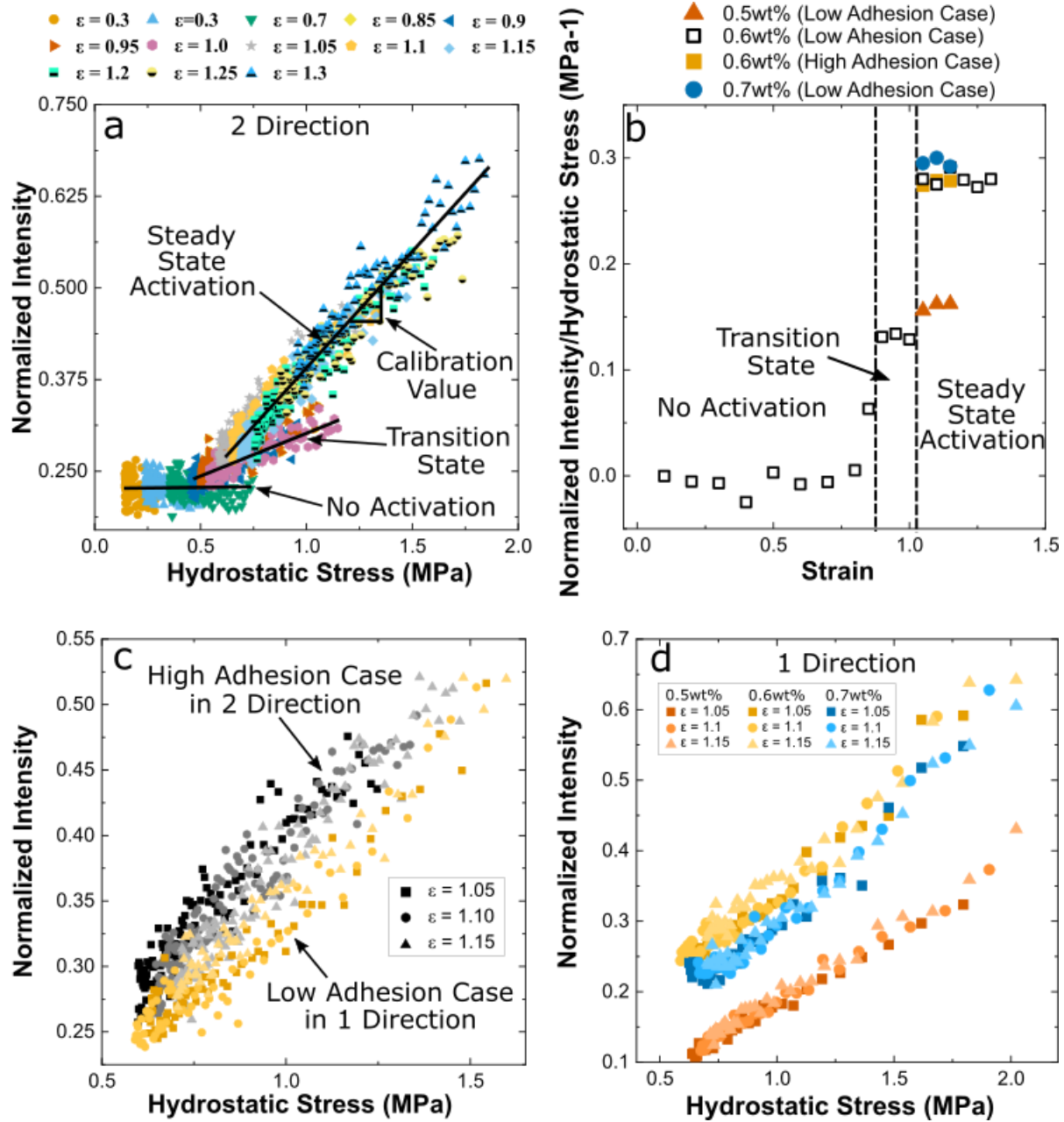


Figure 5-9. The methodology for calibrating MP activation to stress. *a*) The calibration curve of I to σ_h . The solid black lines show the activation regimes as strain increases. *b*) The change in I with respect to σ_h as ε increases. The dashed black lines show the activation regimes. The unfilled data points represent I taken at different microscope settings. *c*) The comparison of the MP activation to σ_h calibration depending on the stress state. The yellow data points represent the stress state of the high adhesion case in the 2 direction and the blue data points represent the low adhesion case in the 1 direction. *d*) The comparison of the I to σ_h calibration depending on SPN concentration. The calibration was taken for the low adhesion case in the 1 direction.

The I to σ_h calibration is taken in the steady state regime ($\varepsilon > 1$) due to the time dependency (Eq. 5-1) on MP activation as well as anisotropic MP activation.^{118,120,122,124,166} Once

enough stress is applied to the matrix at $\varepsilon = 0.8$, MP activation is first able to be observed seen by the increase in Figure 5-9b at $\varepsilon = 0.8$. At the onset of observable MP activation, not all of the SPN molecules activate immediately. As time progresses, while maintaining enough applied stress for MP activation, more MP molecules begin to activate causing I to increase.^{12,124} In the transition regime, the SP molecules are activating, but at a slower rate than in the steady state regime which does not accurately describe the relationship between I and σ_h .

Along with time dependency on MP activation, the location of SPN molecules with respect to the loading direction also attribute to the transition state regime seen in Figure 5-9a. Even though SPN is attached isotropically into the backbone of the PDMS chains achieved through mixing, the SPN molecules will activate anisotropically with SPN molecules that lie in the 2 direction activating first followed by the SPN molecules in the other directions. The polymer chains aligned in the 2 direction undergo loading prior to the chains aligned in other directions causing the SPN molecules aligned in the 2 direction to activate preferentially. In the transition state regime, only SPN molecules in the 2 direction may be activating until $\varepsilon = 1.0$ is reached at which point enough stress has been applied to activate SPN molecules in the other directions. The anisotropic MP activation along with the time dependency on MP activation are factors that possibly explain the transition state regime seen in Figures 5-9a-b. To ensure that anisotropic MP activation and time dependent activation do not affect the determined calibration value, the I to σ calibration value should be taken in the steady state regime.

The I to σ_h calibration methodology presented here requires the ability to experimentally determine a MP activation gradient near a stress concentrator, and model the stress state of the same system using FEA or any other technique. As shown by Dee *et al.*¹²⁵ and Chen *et al.*¹⁹ a crack tip or, shown here, a rigid inclusion are appropriate candidates to act as a stress concentrator in a polymer matrix. Once the FEA simulations match well to the experimental mechanical behavior, characterization of I and σ_h is achieved by plotting I and σ_h as a function of x_2 or x_1 depending on the direction of the MP activation and stress concentration gradients. For the methodology to be implemented, the characterization of I and σ_h must be taken in the same direction. By relating the characterized I and σ_h values at the same x_2 or x_1 depending on the direction of the MP activation and stress concentration gradient, a I to σ_h calibration is determined from the slope of the steady state regime. This methodology is a systematic calibration technique that is capable of calibrating I to σ_h for any polymer-matrix functionalized with MP where I is observable.

5.3.5 Calibrating I to σ with Different Stress States and MP Concentrations

The previous section highlights and outlines the ability of the presented methodology to calibrate I to σ_h . However, this methodology is not constrained to the materials system and stress state presented above. Any observable MP activation gradient caused by a stress concentrator is appropriate to calibrate I to σ_h if the stress state has been characterized. The high adhesion case in the 2 direction was employed to present the methodology, but the low adhesion case is also able to calibrate I to σ_h that should result in the same calibration value when using the same materials system. By changing the material systems, done here by modifying the wt% of SPN functionalized into PDMS, the calibration value will change based on the MP concentration loading.

Using the methodology from above, a I to σ_h calibration was determined utilizing the low adhesion case (Figure 5-6e) with characterizing I and σ_h as a function of x_1 which was then compared to the I to σ_h calibration determined from the high adhesion case (Figure 5-9c). The slope of I to σ_h relationship for the low adhesion case in the 1 direction is $0.277 \pm 0.003 \text{ MPa}^{-1}$ which corresponds well to the slope of I to σ_h relationship for the high adhesion case in the 2 direction (Figure 5-9b). The similar I to σ_h calibration value for the low adhesion case in the 1 direction and high adhesion case in the 2 direction shows a stress state independence for the calibration methodology.

The I to σ_h calibration curves in Figure 5-9c are specific to the materials system of PDMS functionalized with 0.6wt% using the imaging settings mentioned in the materials and methods section. Regardless of the materials system and microscope settings a I to σ_h calibration is achievable following the presented methodology. Before the I to σ_h calibration values were determined, the mechanical behaviors were compared to ensure the stress states determined by FEA were still applicable to the new materials system (Figure 5-10). The intensity normalizations were performed for the 0.7wt% SPN and 0.5wt% SPN systems using the same procedure as the 0.6wt% except calibrating with respect to the 0.7wt% SPN curve and 0.5wt% SPN curve, respectively, in Figure 5-8. To be able to observe activation of the 0.5wt% samples the gain was increased to 600 and laser intensity to 20% when imaging to improve the sensitivity of the imaging system. To compare the 0.5wt% SPN system that was taken at more sensitive imaging settings with the 0.6wt% and 0.7wt% systems a correction factor was multiplied to the normalized intensity for the 0.5wt% system that was taken at more sensitive imaging settings. The applied correction

factor is the ratio of the normalization value of the 0.5wt% system taken at the same imaging settings as the 0.6wt% and 0.7wt% systems to the 0.5wt% system taken at the more sensitive imaging settings.

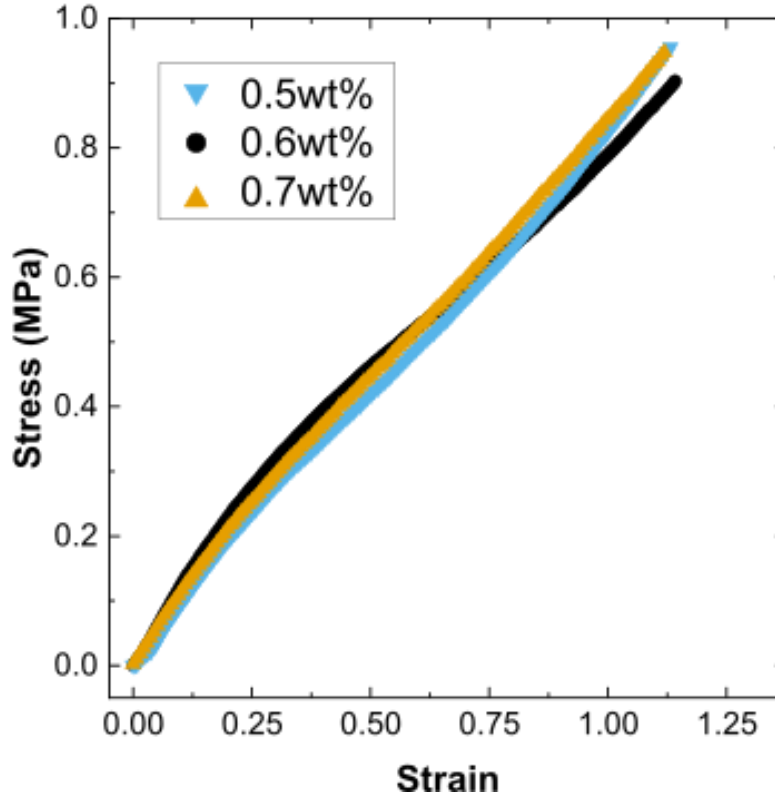


Figure 5-10. $\sigma_{global} - \varepsilon$ results for a PDMS system functionalized with 0.5wt%, 0.6wt%, and 0.7wt% SPN. No change is observed in the mechanical behavior.

When applying the calibration technique to a PDMS system functionalized with 0.7wt% and 0.5 wt% SPN a I to σ_h calibration value was determined (Figure 5-9d). By changing the material systems through increasing the MP concentration to 0.7wt%, the I to σ_h calibration value slightly increased to $0.296 \pm 0.004 \text{ MPa}^{-1}$ (Figure 5-9b) which is expected due to a larger density of SPN molecules in the materials system. Therefore, a I to σ_h calibration will need to be performed when changing the materials system which includes that matrix material, MP, and/or MP concentration.

For the PDMS matrix functionalized with 0.5wt%, the expected result is for a decrease in the I to σ_h calibration value as there will be a smaller density of SPN molecules compared to the 0.6wt% SPN system. By applying the imaging settings correction factor to the 0.5wt% SPN I

values previously mentioned, a comparison is made to the 0.6wt% SPN and 0.7wt% SPN systems. When the MP concentration was decreased to 0.5wt%, the slope of the I to σ_h calibration curve or the 0.5wt% SPN system decreased (Figure 5-9d) resulting in a calibration value of $0.160 \pm 0.004 \text{ MPa}^{-1}$ (Figure 5-9b). Imaging settings have a strong dependence on the I to σ_h calibration value while MP concentration has a weaker dependence. Before applying the imaging settings correction factor to the 0.5wt% SPN system I values, the calibration value significantly increased compared to the 0.6wt% and 0.7wt% SPN systems. Not correcting for the change in imaging settings for the 0.5wt% system and leads to the determination an artificially high I to σ_h calibration value (Figure 5-11). Therefore, before calibrating I to σ_h it is essential to either optimize the imaging settings for a given materials system or create a set of I calibration curves as seen in Figure 5-8.

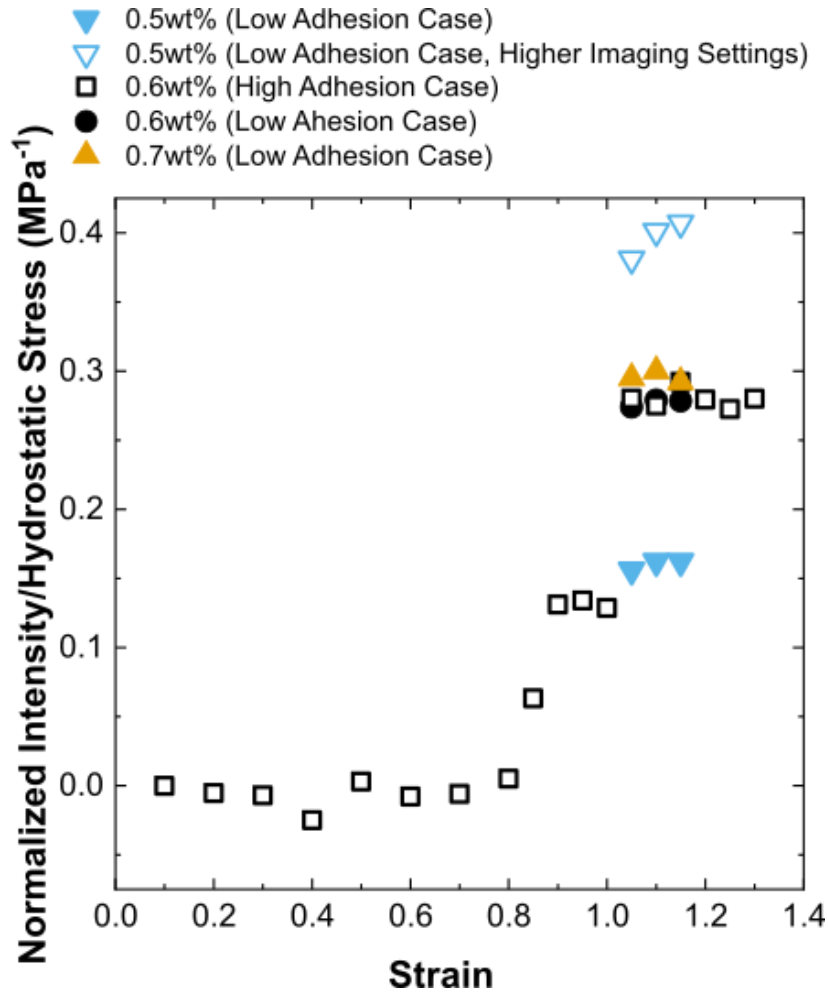


Figure 5-11. The change in I with respect to σ_h as ε increases showing the artificially high determined I to σ_h calibration value for the 0.5wt% system taken at higher imaging settings.

Figures 5-9c-d show the ability of the presented methodology to determine I to σ_h calibrations in different stress states and with different materials systems. Applying the calibration to the same materials system in a different stress state determined similar I to σ_h calibration values while changing the materials system changed the I to σ_h calibration value. Generally, to apply this methodology a I gradient must be observed and FEA simulations modeling the mechanical behavior of the materials system must be obtained. Once I and σ_h have been characterized, relating the two quantities by mapping the x_2 or x_1 profiles to one another determines the I to σ_h calibration. Utilizing the methodology proposed here acts as a tool to calibrate I to σ_h allowing for I to be employed as a quantitative assessment for damage to the materials system.

5.4 Conclusion

Creating a methodology for calibrating I to σ_h is a crucial step for employing MPs as in-situ damage sensors for polymeric materials. Here, a methodology is presented that couples experimentally determined I near a glass particle imbedded in the matrix with FEA determined σ_h of the same system to calibrate I to σ_h . The adhesion of the glass particle to the PDMS matrix and MP concentration were modified to create different stress states and materials system to show the robustness of the calibration methodology.

High, medium, and low adhesion cases of the glass particle to the matrix were examined to determine the MP activation response. The high and low adhesion cases had consistent MP activation in the 2 direction and 1 direction respectively, while the MP activation for the medium adhesion case switched directions during experimentation due to the matrix debonding from the particle at both poles. Due to the directional consistency of I for the low and high adhesion cases were selected for utilization with the calibration methodology.

FEA was employed to determine the stresses near the rigid inclusion of the materials system. The Ogden Model was selected to represent the PDMS/SPN matrix and cohesive zone element formulations were used to represent the adhesion of the glass particle to the PDMS/SPN matrix. Twenty seven runs were simulated to determine the best model for the high and low adhesion cases. σ_h values were found to align closely with expected stress values of the peak stress near the glass particle/matrix interface, and chosen to be the stress type that is related to I .

The high adhesion case was selected to present the methodology where the I and σ_h concentration gradient profiles were characterized in the 2 direction as a function of x_2 . By mapping the I and σ_h profiles to one another the two quantities were related. Once the onset of MP activation occurs and steady state activation is achieved, the I - σ_h relationship was found to be linear with the slope taken as the I - σ_h calibration value.

The low adhesion case was presented to show the robustness of the calibration methodology determining a I - σ_h calibration value under a different stress state and with a different materials system. The I - σ_h calibration determined from the 0.6wt% SPN system for the low adhesion case was compared to the I - σ_h calibration determined from the 0.6wt% SPN system of the high adhesion case and found to agree. By increasing the SPN concentration, the I - σ_h calibration increased, while decreasing the SPN concentration decreased I - σ_h calibration

value. When performing the $I - \sigma_h$ calibration, the applied stress state did not change the calibration value while the materials system affected the determined $I - \sigma_h$ calibration value.

Quantifying MP activation to applied stress is a necessary step for implementing MPs into industrial applications. While many MPs are engineered to behave differently from one another a systematic $I - \sigma_h$ calibration methodology would assist in pushing MP technologies into the practical application space. Such a methodology is presented here by coupling a characterized MP activation response near a stress concentrator with FEA of the same materials system to characterize the stress state near the stress concentrator. The material systems was shown to be dependent on the calibration value with the stress state being independent. The dependence on the material system provides evidence that the calibration methodology can determine a $I - \sigma_h$ calibration for different materials systems other than the PDMS/SPN system used here. The $I - \sigma_h$ calibration methodology has the ability to determine a $I - \sigma_h$ calibration for any materials system with the capability of observing MP activation near a stress concentration providing a methodology capable of quantifying the I to σ_h relationship.

Therefore, before calibrating I to σ_h it is essential to either optimize the imaging settings for a given materials system or create a set of I calibration curves. The presented methodology has the ability to determine I to σ_h calibrations in different stress states and with different materials systems. Applying the calibration to the same materials system in a different stress state determined similar I to σ_h calibration values while changing the materials system changed the I to σ_h calibration value. Generally, to apply this method a I gradient must be observed and FEA simulations modeling the mechanical behavior of the materials system must be obtained. Once I and σ_h have been characterized, relating the two quantities by mapping the x_2 or x_1 profiles to one another determines the I to σ_h calibration. Utilizing the methodology presented here acts as a tool to calibrate I to σ_h allowing for I to be employed as a quantitative assessment for damage to the materials system.

CONCLUSIONS

As industry problems become more advanced, so do the materials system employed to solve them. For new materials to be implemented into practice, the properties and performance must be well characterized. An essential part of assessing the performance of new materials is determining the mechanical properties. Often times commonly utilized mechanical characterization techniques are unable to accurately and rapidly assess properties and performance of these novel material systems warranting the development of new methodologies.

Here, two strategies are utilized for the development of new mechanical characterization techniques. The first is to repurpose old tools and techniques to solve new problems and the second is to develop new tools and techniques to solve older problems. Using the first strategy, a classical buckling mechanics approach to characterize the elastic modulus of brittle films was developed and a methodology used to determine the “handle” of textiles was repurposed to determine the elastic modulus of structurally complex temporary pavement marking tape. By applying the second strategy, a systematic calibration methodology was developed to quantify the response of stress sensing molecules attached into a polymer systems to mitigate unexpected material failure.

Characterizing the elastic modulus of brittle films is important for assessing material performance, but difficult to achieve when applying a technique that utilizes tensile forces. In compression, brittle materials tend to perform better allowing for greater applied forces before failure. When both ends of the film are fixed and a compressive load is applied the film buckled. allowing for the application of classical buckling mechanics to be employed to determine the elastic modulus. Free standing column buckling experiments were performed for PET films of varying geometries to ensure consistency in the measurement as elastic modulus is not geometry dependent. The results agreed well with moduli determined via tensile testing leading to the conclusion that methodology was able to characterize the elastic modulus of brittle films.

Elaborating on the freestanding column buckling modulus determination methodology, a variety of nanocellulose films, all with different moduli, were tested to expand on the limitations and techniques used to determine the elastic modulus. The linear intercept method and Southwell method were two different free standing column buckling approaches taken to determine the elastic modulus of each nanocellulose film. The elastic modulus determine through the linear intercept and Southwell were in good agreement. When compared to the elastic modulus determined

through tensile testing the stiffer, thicker films were found to agree better with moduli determined through free standing column buckling compared to the more compliant, thinner films. Stiffness and freestanding film stability were examined to determine the effects on precision and accuracy of the technique. Film stiffness was found to have a significant impact on the precision and accuracy of determining the elastic modulus through freestanding column buckling and strategies to overcome low film stiffnesses were discussed.

Continuing with buckling mechanics approaches to characterize the elastic modulus, the Peirce cantilever test was applied to temporary pavement marking tape to determine an effective modulus of the tape. The force required to detach a temporary pavement marking tape from a substrate is directly related to the elastic modulus. Therefore, accurately characterizing the elastic modulus is essential for assessing the adhesive performance of temporary pavement marking tapes. Common mechanical characterization techniques such as, tensile and three point bend testing, were shown to have a large variance in determining the elastic modulus due to the structural complexities of temporary pavement marking tapes. When employing the Peirce cantilever test or “Tape Drape Test,” the characterized modulus values aligned well with physical handling assessment of tape stiffness. Additionally, the Tape Drape test is able to be employed in the field which is important due to potential changes in the elastic modulus caused by changes in temperature allowing for the elastic modulus characterization of the tapes to be conducted at the application temperature. The Tape Drape test was found to be the most appropriate method for determining the effective modulus of temporary pavement marking tapes.

A reoccurring problem in industry is premature or unexpected catastrophic failure of polymer materials in expensive material systems. Real time damage sensing capabilities offered by mechanophores are a potential solution to avoid unanticipated material failure. By incorporating mechanophores into the backbone of polymer chains a colorimetric or fluorescence change indicates damage making self-reporting damage sensing in polymer materials a reality. For mechanophores to be implemented into industry, the color or fluorescence change must be calibrated to applied stress. Here, a systematic calibration methodology is presented by relating the fluorescent mechanophore response near a rigid inclusion in an elastomeric matrix with finite element analysis determined hydrostatic stresses of the same system. The methodology was shown to determine the same calibration value when applied to the same system under a different stress state achieved through modifying the rigid inclusion adhesion to the elastomeric matrix. To show

further robustness of the methodology, the materials system was modified by varying the mechanophore concentration in the polymer matrix. The calibration value increased as mechanophore concentration increased and decreased with decreasing the mechanophore concentration. By utilizing the presented methodology, the fluorescent mechanophore activation was calibrated to applied stress which can be applied to any mechanophore functionalized polymer system.

As new materials are developed, new characterization techniques must be developed simultaneously to ensure accurate materials characterization and performance assessments. The focus of this work is on the development of novel mechanical characterization techniques which are essential for performance assessments of materials. Here, two strategies are used for the development and design of novel mechanical characterization methodologies. The first being through repurposing old tools or technologies to solve new problems and the second being through developing new tools or technologies to address old problems. By applying the first strategy, a free standing column buckling methodology was developed to determine the elastic modulus of brittle polymeric films and the Peirce cantilever test developed in 1930 for textiles was applied to temporary pavement marking tapes to determine the elastic modulus. Through the application of the second strategy, mechanophore activation intensity to be applied as in-situ damage sensors in polymeric materials was calibrated to applied stress to help mitigate unexpected material failure.

Hopefully through the examples presented in this work, other engineers will be inspired to develop new mechanical characterization techniques based on the two strategies discussed here. Scientific giants such as Newton, Euler, Gent, etc. have provided engineers and scientists many tools for understanding the world around us. By taking these tools and exploring how they can be applied across engineering and scientific disciplines creates many opportunities for innovation. The work discussed in this dissertation are examples of how we can apply the ideas and concepts that govern the world into application spaces across scientific and engineering disciplines. Just because an idea or concept is mainly used for one specific application does not mean that it is the only way or even the best way to apply them. I implore future engineers and scientists to consider how fundamental scientific laws and relationships can be applied out of their current application spaces to continue the development of novel materials and characterization techniques.

REFERENCES

1. Dizon, J. R. C., Espera, A. H., Chen, Q. & Advincula, R. C. Mechanical characterization of 3D-printed polymers. *Addit. Manuf.* **20**, 44–67 (2018).
2. Peterson, G. I., Larsen, M. B., Ganter, M. A., Storti, D. W. & Boydston, A. J. 3D-printed mechanochromic materials. *ACS Appl. Mater. Interfaces* **7**, 577–583 (2015).
3. Wiggins, K. M., Brantley, J. N. & Bielawski, C. W. Methods for activating and characterizing mechanically responsive polymers. *Chem. Soc. Rev.* **42**, 7130–7147 (2013).
4. El Awad Azrak, S. M., Clarkson, C. M., Moon, R. J., Schueneman, G. T. & Youngblood, J. P. Wet-Stacking Lamination of Multilayer Mechanically Fibrillated Cellulose Nanofibril (CNF) Sheets with Increased Mechanical Performance for Use in High-Strength and Lightweight Structural and Packaging Applications. *ACS Appl. Polym. Mater.* **1**, 2525–2534 (2019).
5. Kier, N. & Nagy, A. Single-Molecule Force Spectroscopy: Optical Tweezers, Magnerit Tweezers and Atomic Force Microscopy. *Nat. Methods* **5**, 491–505 (2008).
6. Chowdhury, R. A., Peng, S. X. & Youngblood, J. Improved order parameter (alignment) determination in cellulose nanocrystal (CNC) films by a simple optical birefringence method. *Cellulose* **24**, 1957–1970 (2017).
7. Rencheck, M., Zelenak, P., Shang, J. & Kim, H. Evaluation of DIC Based Forming Limit Curve Methods at Various Temperatures of Aluminum Alloys for Automotive Applications. in *SAE Technical Paper* (2017). doi:10.4271/2017-01-0309.Copyright
8. Peirce, F. T. The “Handle” of Cloth as a Measurable Quantity. *J. Text. Inst. Trans.* **21**, T377–T416 (1930).
9. Hall, A. K. I., O’Connor, T. C., McGath, M. K. & McGuiggan, P. The bending mechanics of aged paper. *J. Appl. Mech. Trans. ASME* **85**, 1–10 (2018).
10. Ducrot, E., Chen, Y., Bulters, M., Sijbesma, R. P. & Creton, C. Toughening elastomers with sacrificial bonds and watching them break. *Science (80-.).* **344**, 186–189 (2014).
11. Clough, J. M., Creton, C., Craig, S. L. & Sijbesma, R. P. Covalent Bond Scission in the Mullins Effect of a Filled Elastomer: Real-Time Visualization with Mechanoluminescence. *Adv. Funct. Mater.* **26**, 9063–9074 (2016).

12. Deneke, N., Rencheck, M. L. & Davis, C. S. An engineer's introduction to mechanophores. *Soft Matter* **16**, 6230–6252 (2020).
13. Timoshenko, S. P. & Gere, J. *Theory of elastic stability*. (Dover Publications, Inc., 1963).
14. Southwell, R. V. On the Analysis of Experimental Observations in Problems of Elastic Stability. *Proc. R. Soc. A Math. Phys. Eng. Sci.* **135**, 601–616 (1932).
15. Callister, W. D. & Rethwisch, D. G. *Callister's Materials Science and Engineering*. (Wiley, 2020).
16. Li, J., Nagamani, C. & Moore, J. S. Polymer Mechanochemistry: From Destructive to Productive. *Acc. Chem. Res.* **48**, 2181–2190 (2015).
17. Davis, D. a *et al.* Force-induced activation of covalent bonds in mechanoresponsive polymeric materials. *Nature* **459**, 68–72 (2009).
18. Gossweiler, G. R. *et al.* Mechanochemical activation of covalent bonds in polymers with full and repeatable macroscopic shape recovery. *ACS Macro Lett.* **3**, 216–219 (2014).
19. Chen, Y., Joshua Yeh, C., Qi, Y., Long, R. & Creton, C. From force-responsive molecules to quantifying and mapping stresses in soft materials. *Sci. Adv.* **6**, 1–9 (2020).
20. Rencheck, M. L., Rodriguez, R., Miller, N. A. & Davis, C. S. A buckling mechanics approach to elastic modulus determination of glassy polymer films. *J. Polym. Sci. Part B Polym. Phys.* **57**, 15–20 (2019).
21. Li, F. The Potential of NanoCellulose in the Packaging Field: A Review. *Packag. Technol. Sci.* **23**, 253–266 (2010).
22. Johansson, C. *et al.* Renewable fibers and bio-based materials for packaging applications - A review of recent developments. *BioResources* **7**, 2506–2552 (2012).
23. Fujisaki, Y. *et al.* Transparent nanopaper-based flexible organic thin-film transistor array. *Adv. Funct. Mater.* **24**, 1657–1663 (2014).
24. Nogi, B. M., Iwamoto, S. & Nakagaito, A. N. Optically Transparent Nanofiber Paper. *Adv. Mater.* 1595–1598 (2009). doi:10.1002/adma.200803174
25. Hu, L. *et al.* Transparent and conductive paper from nanocellulose fibers. *Energy Environ. Sci.* **6**, 513–518 (2013).
26. Yang, A. C., Wang, R. C. & Lin, J. H. Ductile-brittle transition induced by aging in poly(phenylene oxide) thin films. *Int. J. Sci. Technol. Polym.* **31**, 5751–5754 (1996).

27. Reising, A. B., Moon, R. J. & Youngblood, J. P. Effect Of Particle Alignment on Mechanical Properties of Neat Cellulose Nanocrystal Films. *J. Sci. Technol. For. Prod. Process.* **2**, 32–41 (2012).
28. Liu, J.-C., Moon, R. J., Rudie, A. & Youngblood, J. P. Mechanical Performance of Cellulose Nanofibril Film-Wood Flake Laminate. *Holzforschung* **68**, 283–290 (2014).
29. Gunda, M., Kumar, P. & Katiyar, M. Review of Mechanical Characterization Techniques for Thin Films Used in Flexible Electronics. *Crit. Rev. Solid State Mater. Sci.* **42**, 129–152 (2017).
30. Lewis, J. Material challenge for flexible organic devices. *Mater. Today* **9**, 38–45 (2006).
31. Bolshakov, A. & Pharr, G. M. Influences of pileup on the measurement of mechanical properties by load and depth sensing indentation techniques. *J. Mater. Res.* **13**, 1049–1058 (2017).
32. Taljat, B. & Pharr, G. M. Development of pile-up during spherical indentation of elastic-plastic solids. *Int. J. Solids Struct.* **41**, 3891–3904 (2004).
33. Cheng, Y. T. & Cheng, C. M. Relationships between initial unloading slope, contact depth, and mechanical properties for spherical indentation in linear viscoelastic solids. *Mater. Sci. Eng. A* **409**, 93–99 (2005).
34. Stafford, C. M. *et al.* A buckling-based metrology for measuring the elastic moduli of polymeric thin films. *Nat. Mater.* **3**, 545–550 (2004).
35. Cranston, E. D. *et al.* Determination of Young's modulus for nanofibrillated cellulose multilayer thin films using buckling mechanics. *Biomacromolecules* **12**, 961–969 (2011).
36. Kan, K. H. M. & Cranston, E. D. Mechanical testing of thin film nanocellulose composites using buckling mechanics. *TAPPI J.* **12**, 35–43 (2013).
37. Khang, D. Y., Rogers, J. A. & Lee, H. H. Mechanical buckling: Mechanics, metrology, and stretchable electronics. *Adv. Funct. Mater.* **19**, 1526–1536 (2009).
38. Coşkun, S. B. & Atay, M. T. Determination of critical buckling load for elastic columns of constant and variable cross-sections using variational iteration method. *Comput. Math. with Appl.* **58**, 2260–2266 (2009).
39. Singer, J., Arbocz, J. & Weller, T. *Buckling Experiments: Experimental Methods in Buckling Thin-Walled Structures*. (John Wiley and Sons, Inc., 1998).

40. Salmon, E. H. *Columns: A Treatise on the Strength and Design of Compression Members*. (Oxford Technical Publications, 1921).
41. Mandal, P. & Calladine, C. R. Lateral-torsional buckling of beams and the Southwell plot. *Int. J. Mech. Sci.* **44**, 2557–2571 (2002).
42. Tomblin, J. & Barbero, E. Local buckling experiments on FRP columns. *Thin-Walled Struct.* **18**, 97–116 (1994).
43. Holmes, D. P. & Crosby, A. J. Snapping surfaces. *Adv. Mater.* **19**, 3589–3593 (2007).
44. Timoshenko, S. P. & Woinowsky-Krieger, S. *Theory of Plates and Shells*. (1964).
45. Croll, J. G. & Walker, A. C. *Elements of Structural Stability*. (John Wiley and Sons, Inc., 1972).
46. Peterson, E. C. Stiffness in Fabrics Produced by Different Starches and Starch Mixtures, and a Quantitative Method for Evaluating Stiffness. *Tech. Bull. United States Dep. Agric.* (1929).
47. Plaut, R. H. Formulas to determine fabric bending rigidity from simple tests. *Text. Res. J.* **85**, 884–894 (2015).
48. Rencheck, M. L. *et al.* Nanocellulose Film Modulus Determination via Buckling Mechanics Approaches. *ACS Appl. Polym. Mater.* **2**, 578–584 (2019).
49. Taylor, P., Weber, C. J., Haugaard, V., Festersen, R. & Bertelsen, G. Production and applications of biobased packaging materials for the food industry Production and applications of biobased packaging materials for the food industry. 37–41 (2010). doi:10.1080/0265203011008748
50. Petersen, K. *et al.* Potential of biobased materials for food packaging. *Trends Food Sci. Technol.* **10**, 52–68 (1999).
51. Bhutta, M. K. S., Omar, A. & Yang, X. Electronic Waste : A Growing Concern in Today ' s Environment. *Econ. Res. Int.* **2011**, (2011).
52. Berkhout, F. & Smith, D. Products and the environment: An integrated approach to policy. *Eur. Environ.* **9**, 174–185 (1999).
53. Okahisa, Y., Yoshida, A., Miyaguchi, S. & Yano, H. Optically transparent wood – cellulose nanocomposite as a base substrate for flexible organic light-emitting diode displays. *Compos. Sci. Technol.* **69**, 1958–1961 (2009).

54. Moon, R. J., Martini, A., Nairn, J., Simonsen, J. & Youngblood, J. *Cellulose nanomaterials review: structure, properties and nanocomposites*. *Chemical Society Reviews* **40**, (2011).
55. Zhu, H. *et al.* Wood-Derived Materials for Green Electronics, Biological Devices, and Energy Applications. *Chem. Rev.* **116**, 9305–9374 (2016).
56. Klemm, D. *et al.* Nanocellulose materials - Different cellulose, different functionality. *Macromol. Symp.* **280**, 60–71 (2009).
57. Peng, S. X., Moon, R. J. & Youngblood, J. P. Design and characterization of cellulose nanocrystal-enhanced epoxy hardeners. *Green Mater.* **2**, 193–205 (2014).
58. Gardner, K. H. & Blackwell, J. The Hydrogen Bonding in Native Cellulose. *Biochim. Biophys. Acta* **343**, 232–237 (1974).
59. Diaz, J. A., Wu, X., Martini, A. & Moon, R. J. Thermal Expansion of Self-Organized and Shear-Oriented Cellulose Nanocrystal Films. *Biomacromolecules* **14**, 2900–2908 (2013).
60. Oliver, W. C. & Pharr, G. M. An improved technique for determining hardness and elastic modulus using load and displacement sensing indentation experiments. *J. Mater. Res.* **7**, 1564–1583 (1992).
61. Yan, W., Pun, C. L., Wu, Z. & Simon, G. P. Some issues on nanoindentation method to measure the elastic modulus of particles in composites. *Compos. Part B Eng.* **42**, 2093–2097 (2011).
62. Davis, C. S. & Crosby, A. J. Mechanics of wrinkled surface adhesion. *Soft Matter* **7**, 5373 (2011).
63. Bowden, N., Huck, W. T. S., Paul, K. E. & Whitesides, G. M. The controlled formation of ordered, sinusoidal structures by plasma oxidation of an elastomeric polymer. *Appl. Phys. Lett.* **75**, 2557 (1999).
64. Volynskii, A. L., Bazhenov, S., Lebedeva, O. V & Bakeev, N. F. Mechanical buckling instability of thin coatings deposited on soft polymer substrates. *J. Mater. Sci.* **5**, 547–554 (2000).
65. Johansson, E. & Wågberg, L. Tailoring the mechanical properties of starch-containing layer-by-layer films. *Colloids Surfaces A Physicochem. Eng. Asp.* **394**, 14–22 (2012).
66. Eita, M., Arwin, H., Granberg, H. & Wågberg, L. Addition of silica nanoparticles to tailor the mechanical properties of nanofibrillated cellulose thin films. *J. Colloid Interface Sci.* **363**, 566–572 (2011).

67. Cai, S., Breid, D., Crosby, A. J., Suo, Z. & Hutchinson, J. W. Periodic patterns and energy states of buckled films on compliant substrates. *J. Mech. Phys. Solids* **59**, 1094–1114 (2011).
68. Mei, H., Huang, R., Chung, J. Y., Stafford, C. M. & Yu, H. H. Buckling modes of elastic thin films on elastic substrates. *Appl. Phys. Lett.* **90**, 1–4 (2007).
69. de Assis, C. A. *et al.* Cellulose micro- and nanofibrils (CMNF) manufacturing - financial and risk assessment. *Biofuels, Bioprod. Biorefining* **12**, 251–264 (2018).
70. Chowdhury, R. A. *et al.* Cellulose Nanocrystal (CNC) Coatings with Controlled Anisotropy as High-Performance Gas Barrier Films. *ACS Appl. Mater. Interfaces* **11**, 1376–1383 (2019).
71. International, A. ASTM D638-14 Standard Test Method for Tensile Properties of Plastics. *ASTM Int.* (2014). doi:10.1520/D0638-14.1
72. Mirmiran, A., Shahawy, M. & Beitleman, T. Slenderness Limit for Hybrid FRP-Concrete Columns. *J. Compos. Constr.* **5**, 26–34 (2001).
73. Dufresne, A., Cavaillé, J. Y. & Helbert, W. Thermoplastic nanocomposites filled with wheat straw cellulose whiskers. Part II: Effect of processing and modeling. *Polym. Compos.* **18**, 198–210 (1997).
74. Turner, M. J., Clough, R. W., Martin, H. C. & Topp, L. J. Stiffness and Deflection Analysis of Complex Structures. *J. Aeronaut. Sci.* **23**, 805–823 (1956).
75. Megson, T. H. G. Stress and Strain. in *Structural and Stress Analysis* **2**, 150–187 (2005).
76. Atay, M. T. & Coşkun, S. B. Elastic stability of Euler columns with a continuous elastic restraint using variational iteration method. *Comput. Math. with Appl.* **58**, 2528–2534 (2009).
77. Donnell, E. T., Chehab, G. R., Tang, X. & Schall, D. Exploratory analysis of accelerated wear testing to evaluate performance of pavement markings. *Transp. Res. Rec.* 76–84 (2009). doi:10.3141/2107-08
78. Lee, J. T., Maleck, T. L. & Taylor, W. C. Pavement marking material evaluation study in Michigan. *ITE J. (Institute Transp. Eng.* **69**, (1999).
79. Ellis, R. *Development of Improved Procedures for Managing Pavement Markings During FDOT Highway Construction Projects.* (2003).
80. Finley, M. D. & Ullman, B. R. Field evaluation of in-lane pavement markings in advance of freeway interchanges. *Transp. Res. Rec.* 32–40 (2011). doi:10.3141/2250-05

81. Retting, R. A., Greene, M. A. & Van Houten, J. Use of pavement markings to reduce rear-end conflicts at commercial driveway locations. *Transp. Res. Rec.* 106–110 (1997). doi:10.3141/1605-13
82. Songchitruksa, P., Ullman, G. L. & Pike, A. M. Guidance for Cost-Effective Selection of Pavement Marking Materials for Work Zones. *J. Infrastruct. Syst.* **17**, 55–65 (2010).
83. Hawkins, N., Smadi, O. & Aldemir-Bektas, B. *Evaluating the Effectiveness of Temporary Work-Zone Pavement Marking Products*. **5**, (2012).
84. Guidance for the Use of Temporary Pavement Marking in Work zones. (2014).
85. Dan, H. C., Tan, J. W., Zhang, Z. & He, L. H. Modelling and estimation of water infiltration into cracked asphalt pavement. *Road Mater. Pavement Des.* **18**, 590–611 (2017).
86. Xu, H., Guo, W. & Tan, Y. Permeability of asphalt mixtures exposed to freeze-thaw cycles. *Cold Reg. Sci. Technol.* **123**, 99–106 (2016).
87. Migletz, J., Graham, J. L., Harwood, D. W. & Bauer, K. M. Service life of durable pavement markings. *Transp. Res. Rec.* 13–21 (2001). doi:10.3141/1749-03
88. Zhou, X., Wang, S. & Zhou, C. Thermal Conduction and Insulation Modification in Asphalt-Based Composites. *J. Mater. Sci. Technol.* **28**, 285–288 (2012).
89. Airey, G. D., Collop, A. C., Zoorob, S. E. & Elliott, R. C. The influence of aggregate, filler and bitumen on asphalt mixture moisture damage. *Constr. Build. Mater.* **22**, 2015–2024 (2008).
90. McGovern, M. E., Behnia, B., Buttlar, W. G. & Reis, H. Characterisation of oxidative ageing in asphalt concrete - Part 1: Ultrasonic velocity and attenuation measurements and acoustic emission response under thermal cooling. *Insight Non-Destructive Test. Cond. Monit.* **55**, 596–604 (2013).
91. Aktan, F. & Schnell, T. Performance evaluation of pavement markings under dry, wet, and rainy conditions in the field. *Transp. Res. Rec.* 38–49 (2004). doi:10.3141/1877-05
92. Bartlett, M. D. *et al.* Looking Beyond Fibrillar Features to Scale Gecko-Like Adhesion. *Adv. Mater.* **24**, 1078–1083 (2012).
93. Bartlett, M. D., Croll, A. B. & Crosby, A. J. Designing Bio-Inspired Adhesives for Shear Loading : From Simple Structures to Complex Patterns. *Adv. Funct. Mater.* 4985–4992 (2012). doi:10.1002/adfm.201201344

94. Kendall, K., Kendall, K. & Kendall, K. Crack propagation in lap shear joints Crack propagation in lap shear joints. *J. Phys. D. Appl. Phys.* **8**, 512 (1975).
95. Creton, C. Pressure-Sensitive Adhesives : An Introductory Course. *MRS Bull.* **28**, 434–439 (2003).
96. Choubane, B., Sevearance, J., Holzschuher, C., Fletcher, J. & Wang, C. (Ross). Development and Implementation of a Pavement Marking Management System in Florida. *Transp. Res. Rec.* **2672**, 209–219 (2018).
97. Gower, M. D. & Shanks, R. A. The effect of varied monomer composition on adhesive performance and peeling master curves for acrylic pressure-sensitive adhesives. *J. Appl. Polym. Sci.* **93**, 2909–2917 (2004).
98. Cantor, A. S. Glass transition temperatures of hydrocarbon blends: adhesives measured by differential scanning calorimetry and dynamic mechanical analysis. *J. Appl. Polym. Sci.* **77**, 826–832 (2000).
99. ASTM (American Society for Testing and Materials). D638 - Standard test method for tensile properties of plastics. *Annu. B. ASTM Stand.* **08**, 46–58 (2003).
100. ASTM D790-17. Flexural Properties of Unreinforced and Reinforced Plastics and Electrical Insulating Materials. *ASTM Stand.* 12 (2017). doi:10.1520/D0790-17.2
101. ASTM D1388-08. Standard Test Method for Stiffness of Fabrics. *ASTM Int.* 1–6 (2012). doi:10.1520/D1388-18.2
102. Lammens, N., Kersemans, M., Luyckx, G., Van Paepegem, W. & Degrieck, J. Improved accuracy in the determination of flexural rigidity of textile fabrics by the Peirce cantilever test (ASTM D1388). *Text. Res. J.* **84**, 1307–1314 (2014).
103. Abbott, N. J. The Measurement of Stiffness in Textile Fabrics. *Text. Res. J.* **21**, 435–441 (1951).
104. Szablewski, P. & Kobza, W. Numerical analysis of Peirce’s cantilever test for the bending rigidity of textiles. *Fibres Text. East. Eur.* **11**, 54–57 (2003).
105. Brantley, J. N., Wiggins, K. M. & Bielawski, C. W. Polymer mechanochemistry: the design and study of mechanophores. *Polym. Int.* **62**, 2–12 (2013).
106. Li, J., Nagamani, C. & Moore, J. S. Polymer Mechanochemistry: From Destructive to Productive. *Acc. Chem. Res.* **48**, 2181–2190 (2015).

107. Joshi, K., Scheiner, M., Olawale, D. O. & Dickens, T. J. *Triboluminescent Sensors for Polymer-Based Composites. Triboluminescence: Theory, Synthesis, and Application* (Springer International Publishing, 2016). doi:10.1007/978-3-319-38842-7_10
108. Shohag, M. A. S., Tran, S. A., Ndebele, T., Adhikari, N. & Okoli, O. I. Designing and implementation of triboluminescent materials for real-time load monitoring. *Mater. Des.* **153**, 86–93 (2018).
109. Ahmad, F., Choi, H. S. & Park, M. K. A review: Natural fiber composites selection in view of mechanical, light weight, and economic properties. *Macromol. Mater. Eng.* **300**, 10–24 (2015).
110. Anaidhuno, U. P. & Edelugo, S. O. Evaluation of the Mechanical Properties and Simulation of Sisal / Jute Hybrid Polymer Composite Failure in Automobile Chassis Panel . **07**, 56–64 (2017).
111. Chen, Y. *et al.* Mechanical activation of mechanophore enhanced by strong hydrogen bonding interactions. *ACS Macro Lett.* **3**, 141–145 (2014).
112. Woodcock, J. W. *et al.* Observation of Interfacial Damage in a Silk-Epoxy Composite, Using a Simple Mechanoresponsive Fluorescent Probe. *Adv. Mater. Interfaces* 1601018 (2017). doi:10.1002/admi.201601018
113. Raisch, M. *et al.* Highly Sensitive, Anisotropic, and Reversible Stress/Strain-Sensors from Mechanochromic Nanofiber Composites. *Adv. Mater.* **30**, 1802813 (2018).
114. Sung, J., Robb, M. J., White, S. R., Moore, J. S. & Sottos, N. R. Interfacial Mechanophore Activation Using Laser-Induced Stress Waves. *J. Am. Chem. Soc* **140**, 25 (2018).
115. Beiermann, B. A. *et al.* Environmental effects on mechanochemical activation of spiropyran in linear PMMA. *J. Mater. Chem.* **21**, 8443 (2011).
116. Lee, C. K. *et al.* Exploiting force sensitive spiropyran as molecular level probes. *Macromolecules* **46**, 3746–3752 (2013).
117. Beiermann, B. A. *et al.* The Effect of Polymer Chain Alignment and Relaxation on Force-Induced Chemical Reactions in an Elastomer. *Adv. Funct. Mater.* **24**, 1529–1537 (2014).
118. Kim, T. A., Robb, M. J., Moore, J. S., White, S. R. & Sottos, N. R. Mechanical Reactivity of Two Different Spiropyran Mechanophores in Polydimethylsiloxane. *Macromolecules* **51**, 9177–9183 (2018).

119. Gossweiler, G. R. *et al.* Mechanochemical Activation of Covalent Bonds in Polymers with Full and Repeatable Macroscopic Shape Recovery. *ACS Macro Lett.* **3**, 216–219 (2014).
120. Lin, Y., Barbee, M. H., Chang, C.-C. & Craig, S. L. Regiochemical Effects on Mechanophore Activation in Bulk Materials. *J. Am. Chem. Soc.* **140**, 15969–15975 (2018).
121. Wang, Q., Gossweiler, G. R., Craig, S. L. & Zhao, X. Cephalopod-inspired design of electro-mechano-chemically responsive elastomers for on-demand fluorescent patterning. *Nat. Commun.* **5**, 1–9 (2014).
122. Beiermann, B. A., Kramer, S. L. B., Moore, J. S., White, S. R. & Sottos, N. R. Role of Mechanophore Orientation in Mechanochemical Reactions. *ACS Macro Lett.* **1**, 163–166 (2012).
123. Davis, D. A. *et al.* Force-induced activation of covalent bonds in mechanoresponsive polymeric materials. *Nature* **459**, 68–72 (2009).
124. Brown, C. L. & Craig, S. L. Molecular engineering of mechanophore activity for stress-responsive polymeric materials. *Chem. Sci.* **6**, 2158–2165 (2015).
125. Celestine, A. D. N., Sottos, N. R. & White, S. R. Strain and stress mapping by mechanochemical activation of spiropyran in poly(methyl methacrylate). *Strain* **55**, 1–17 (2019).
126. Goodier, J. N. Concentration of Stress Around Spherical and Cylindrical Inclusions and Flaws. *Trans. Am. Soc. Mech. Eng.* **1**, (1933).
127. Eshelby, J. D. The Determination of the Elastic Field of an Ellipsoidal Inclusion, and Related Problems. *Proc. R. Soc. A Math. Phys. Eng. Sci.* **241**, 376–396 (1957).
128. Celestine, A. D. N. *et al.* Fracture-induced activation in mechanophore-linked, rubber toughened PMMA. *Polym. (United Kingdom)* **55**, 4164–4171 (2014).
129. Terpilowski, K. & Rymuszka, D. Surface properties of glass plates activated by air, oxygen, nitrogen and argon plasma. *Glas. Phys. Chem.* **42**, 535–541 (2016).
130. Lin, Y., Barbee, M. H., Chang, C. C. & Craig, S. L. Regiochemical Effects on Mechanophore Activation in Bulk Materials. *J. Am. Chem. Soc.* **140**, 15969–15975 (2018).
131. Gossweiler, G. R., Kouznetsova, T. B. & Craig, S. L. Force-rate characterization of two spiropyran-based molecular force probes. *J. Am. Chem. Soc.* **137**, 6148–6151 (2015).
132. Megson, T. H. G. Deflection of Beams. in *Structural and Stress Analysis* 337–338 (Elsevier, 2014).

133. Makishima, A. & Mackenzie, J. D. Calculation of Bulk Modulus, Shear Modulus, and Poisson's Ratio of Glass. *J. Non. Cryst. Solids* **17**, 147–157 (1975).
134. Spinner, S. Elastic Moduli of Glasses by a Dynamic Method. *J. Am. Ceram. Soc.* **37**, 229–234 (1954).
135. Zheng, P. & McCarthy, T. J. Rediscovering silicones: Molecularly smooth, low surface energy, unfilled, UV/Vis-transparent, extremely cross-linked, thermally stable, hard, elastic PDMS. *Langmuir* **26**, 18585–18590 (2010).
136. Gent, A. N. & Park, B. Failure Processes in Elastomers At or Near a Rigid Spherical Inclusion. **19**, 1947–1956 (1984).
137. Gent, A. N. Detachment of an elastic matrix from a rigid spherical inclusion. *J. Mater. Sci.* **15**, 2884–2888 (1980).
138. Liu, H. T., Ju, J. W. & Sun, L. Z. An Interfacial Debonding Model for Particle-reinforced Composites. *Int. J. Damage Mech.* **13**, 163–185 (2004).
139. Zimmerlin, J. A., Sanabria-Delong, N., Tew, G. N. & Crosby, A. J. Cavitation rheology for soft materials. *Soft Matter* **3**, 763–767 (2007).
140. Gent, A. N. & Wang, C. Fracture mechanics and cavitation in rubber-like solids. *J. Mater. Sci.* **26**, 3392–3395 (1991).
141. Fukahori, Y. & Seki, W. Stress analysis of elastomeric materials at large extensions using the finite element method. *J. Mater. Sci.* **28**, 4471–4482 (1993).
142. Fukahori, Y. & Seki, W. Stress analysis of elastomeric materials at large extensions using the finite element method. *J. Mater. Sci.* **28**, 4471–4482 (1993).
143. Celestine, A. D. N. *et al.* Fracture-induced activation in mechanophore-linked, rubber toughened PMMA. *Polym. (United Kingdom)* **55**, 4164–4171 (2014).
144. Shahzad, M., Kamran, A., Siddiqui, M. Z. & Farhan, M. Mechanical characterization and FE modelling of a hyperelastic material. *Mater. Res.* **18**, 918–924 (2015).
145. Marckmann, G. & Verron, E. Comparison of hyperelastic models for rubber-like materials. *Rubber Chem. Technol.* **79**, 835–858 (2006).
146. Steinmann, P., Hossain, M. & Possart, G. Hyperelastic models for rubber-like materials: Consistent tangent operators and suitability for Treloar's data. *Arch. Appl. Mech.* **82**, 1183–1217 (2012).

147. Ali, A., Hosseini, M. & Sahari, B. A review of constitutive models for rubber-like materials. *Am. J. Eng. Appl. Sci.* **3**, 232–239 (2010).
148. Khajehsaeid, H., Arghavani, J. & Naghdabadi, R. A hyperelastic constitutive model for rubber-like materials. *Eur. J. Mech. A/Solids* **38**, 144–151 (2013).
149. Ogden, R. W. Large deformation isotropic elasticity: on the correlation of theory and experiment for compressible rubberlike solids. *Proc. R. Soc. London. A. Math. Phys. Sci.* **328**, 567–583 (1972).
150. Mooney, M. A theory of large elastic deformation. *J. Appl. Phys.* **11**, 582–592 (1940).
151. Rivlin, R. S. Large Elastic Deformations of Isotropic Materials. *Collect. Pap. R.S. Rivlin* **822**, 90–108 (1997).
152. Yu, Y. S. & Zhao, Y. P. Deformation of PDMS membrane and microcantilever by a water droplet: Comparison between Mooney-Rivlin and linear elastic constitutive models. *J. Colloid Interface Sci.* **332**, 467–476 (2009).
153. Cardoso, C., Fernandes, C. S., Lima, R. & Ribeiro, J. Biomechanical analysis of PDMS channels using different hyperelastic numerical constitutive models. *Mech. Res. Commun.* **90**, 26–33 (2018).
154. Brewer, J. C. & Lagace, P. A. Quadratic Stress Criterion for Initiation of Delamination. *J. Compos. Mater.* **22**, 1141–1155 (1988).
155. Benzeggagh, M. L. & Kenane, M. Measurement of Mixed-Mode Delamination Fracture Toughness of Unidirectional Glass/Epoxy Composites with Mixed-Mode Bending Apparatus. *Compos. Scie* **56**, 439–449 (1996).
156. Vaughan, T. J. & McCarthy, C. T. Micromechanical modelling of the transverse damage behaviour in fibre reinforced composites. *Compos. Sci. Technol.* **71**, 388–396 (2011).
157. Yang, L., Yan, Y., Liu, Y. & Ran, Z. Microscopic failure mechanisms of fiber-reinforced polymer composites under transverse tension and compression. *Compos. Sci. Technol.* **72**, 1818–1825 (2012).
158. González, C. & LLorca, J. Mechanical behavior of unidirectional fiber-reinforced polymers under transverse compression: Microscopic mechanisms and modeling. *Compos. Sci. Technol.* **67**, 2795–2806 (2007).

159. Yu, X., Zhang, B. & Gu, B. Interfacial fatigue damage behavior of fiber reinforced rubber—A combined experimental and cohesive zone model approach. *Polym. Eng. Sci.* **60**, 1316–1323 (2020).
160. Silberstein, M. N. *et al.* Modeling mechanophore activation within a viscous rubbery network. *J. Mech. Phys. Solids* **63**, 141–153 (2014).
161. Pawlak, A. & Galeski, A. Determination of stresses around beads in stressed epoxy resin by photoelasticity. *J. Appl. Polym. Sci.* **86**, 1436–1444 (2002).
162. Thomson, R. D. & Hancock, J. W. Local stress and strain fields near a spherical elastic inclusion in a plastically deforming matrix. *Int. J. Fract.* **24**, 209–228 (1984).
163. Chen, W. T. Axisymmetric Stress Field Around Spheroidal Inclusions and Cavities in a Transversely Isotropic Material. *J. Appl. Mech.* **35**, 770 (1968).
164. Hoshino, T. *et al.* Mechanical stress analysis of a rigid inclusion in distensible material: a model of atherosclerotic calcification and plaque vulnerability. *Am. J. Physiol. Hear. Circ. Physiol.* **297**, 802–810 (2009).
165. Chiang, C. R. Stress concentration around a spherical cavity in a cubic medium. *J. Strain Anal. Eng. Des.* **42**, 155–162 (2007).
166. Degen, C. M., May, P. A., Moore, J. S., White, S. R. & Sottos, N. R. Time-dependent mechanochemical response of SP-cross-linked PMMA. *Macromolecules* **46**, 8917–8921 (2013).